COMPUTATIONAL MODELING OF A SCALABLE HUMAN BODY AND DEVELOPMENT OF A HELMET TESTING DIGITAL TWIN

by

Sean Bucherl

A Thesis

Submitted to the Faculty of Purdue University

In Partial Fulfillment of the Requirements for the degree of

Master of Science in Mechanical Engineering

School of Mechanical Engineering

West Lafayette, Indiana

May 2022

THE PURDUE UNIVERSITY GRADUATE SCHOOL
STATEMENT OF COMMITTEE APPROVAL

Dr. Eric Nauman, Co-Chair

School of Mechanical Engineering and Weldon School of Biomedical Engineering

Dr. Vitaliy Rayz, Co-Chair

Weldon School of Biomedical Engineering

Dr. Thomas Talavage

School of Electrical and Computer Engineering

Dr. Kevin Lister

Corvid Technologies LLC

Approved by:

Dr. Nicole Key

To my family, the buttress that has always supported me.

ACKNOWLEDGMENTS

I want to express my gratitude and appreciation to those who have provided me assistance during my graduate student research, starting with the members of my committee: Dr. Eric Nauman, Dr. Vitaly Rayz, Dr. Thomas Talavage, and Dr. Kevin Lister. Beginning with the co-chairs of my committee, Dr. Nauman and Dr. Rayz, I want to express my thanks. Dr. Nauman, thank you for the advice that you have given me throughout my undergrad and graduate research and the insights, from big picture to minutia, that you have drawn my attention toward. Dr. Rayz, thank you for agreeing to become a co-chair on my committee and smoothing the transition from single chair to two co-chairs. Your feedback on my research has been very much appreciated and values. I thank Dr. Talavage for his guidance on digital signal processing and the different avenues that are available to do so. I thank Dr. Lister for his mentorship to me during my internship at Corvid Technologies, as well as his continued advice after in matters related to finite element simulation.

Thank you to the current and former members of the HIRRT Lab; your camaraderie and advice were always welcomed and appreciated. I want to especially thank Kevin McIver for his input and for his input and advice on my research and for being a stalwart colleague and good friend.

I also wish to extend my thanks to the entities that have funded my education and research. Thank you to Purdue's Engineering Honors College for the funding you provided and the experience I acquired being under your care. Thank you as well to Corvid and the USAF for the opportunity to work on an AFWERX-STTR and the funding granted to me as a result. My thanks as well to the US army for the funding that has come with the AAMP-EM contract on which I have worked.

TABLE OF CONTENTS

LIST OF TABLES

LIST OF FIGURES

ABBREVIATIONS

ATD	Anthropomorphic Test Dummy
GHBMC	Global Human Body Models Consortium
HBM	Human Body Model
THUMS	Total Human Model for Safety
CAVEMAN	Computational Anthropomorphic Virtual Experiment Man
TBI	Traumatic Brain Injury
CTE	Chronic Traumatic Encephalopathy
NOCSAE	National Operating Committee on Standards for Athletic Equipment
FE	Finite Element
1D	1 Dimensional
3D	3 Dimensional
ANSURII	Anthropometric Survey of U.S. Army Personnel
FB-1DS	Full Body 1D Scaaler
H3	Hybrid III
SPC	Single Point Restraint
PTA	Peak Translational Acceleration
PRA	Peak Rotational Acceleration
H5	Hierarchical Data Format 5
RRSC	Riddell Revolution Speed Classic

ABSTRACT

Human body models (HBMs) have been present in the automotive industry for simulating automotive related injury since the turn of the century and have in recent years found a place in assessment of soldier and sports related injury prediction and assessment. This issue is the lack of models that lie outside of the 50th percentile. By a simple application of physics, it is evident that acceleration or force will affect people of varying weights differently. To this end, having the ability to scale a 50th percentile HBM to targets for weight and stature would allow for better characterization on how an impact or acceleration event will affect people of differing size, especially when ~90% of males can fall outside the 50th percentile for weight and stature and HBMs models from vendors exist in only a few variations outside the 50th percentile [1]. Using Corvid Technologies' 50th percentile model CAVEMAN (capable of being repositioned) as a base, scaled model from the 5th to 95th percentiles of stature and weight were generated based on ANSURII metrics, using a combination of 1D and 3D scaling transformations. These models met their stature and weight metrics when standing and weight metrics when positioned.

After creation of a framework to scale the CAVEMAN HMB, creation of a digital twin to the HIRRT Lab helmet testing model commenced. With the HIRRT Lab's history of experimental testing of football helmets, a natural turn of events was to bring helmet performance testing into the computational space. This digital twin was a natural evolution and addition to the HIRRT Lab's helmet testing as it would enable manipulation of helmets that would be infeasible experimentally. After calibration of the barehead using experimental data, helmeted simulation began. Angle of impact, while it was found to effect peak translational acceleration, was found to profoundly effect peak rotational acceleration. With this in mind, various angles of impact were simulated to produce curves similar to experimental results. Helmeted simulations were qualitatively dissimilar to experimental data, prompting a modification of the padding material used by the models. Following various modifications of the padding material model, these inconsistencies between simulated helmets and experimentally tested helmets persisted. These inconsistencies highlight a need for better characterization of material, such as foam, and more thorough validation of simulated helmet models. The results of the helmeted simulations are difficult to quantify, as the evaluation criteria used for the BioCore model did not include rotational acceleration, indicating a need for further research and simulation is necessary.

1. INTRODUCTION

1.1 Modeling of the Human Body

Human body testing, whether it be with cadaveric bodies costing thousands of dollars or test dummies costing hundreds of thousands of dollars, paired with testing of vehicles worth tens of thousands to millions of dollars immediately paints a picture of a possible very expensive inconclusive result[2]–[4]. This price hits a lot harder if the experiment involves destructive testing of a vehicle through the use of collisions or under body blast tests. This is where simulations using finite element models of human bodies and vehicles has the opportunity to reduce the consumables cost of experimental testing with the benefit of being able to see the soft and hard tissue damage. Human body model simulations have a distinct advantage over anthropometric test dummy (ATD) simulation in that ATDs do not have soft tissue to speak of.

Modeling of the human body has been a subject of research for nearly half a century with a notable early example being the mathematical model of the human thorax by Lobdell et al., which was composed of a system of masses, springs, and dashpots in a linear configuration [5]. Finite element modeling of the human body became of particular interest to the automotive industry around the turn of the century with models of the constituents parts of the body like the head, neck, thorax, arm, and leg [6]–[12].

There were also early full body 50^{th} percentile male human body models HBMs running in MADYMO, Radioss, and THUMS (Total Human Model for Safety); these HBMs can be seen in Figure 1.1 [13]–[17].

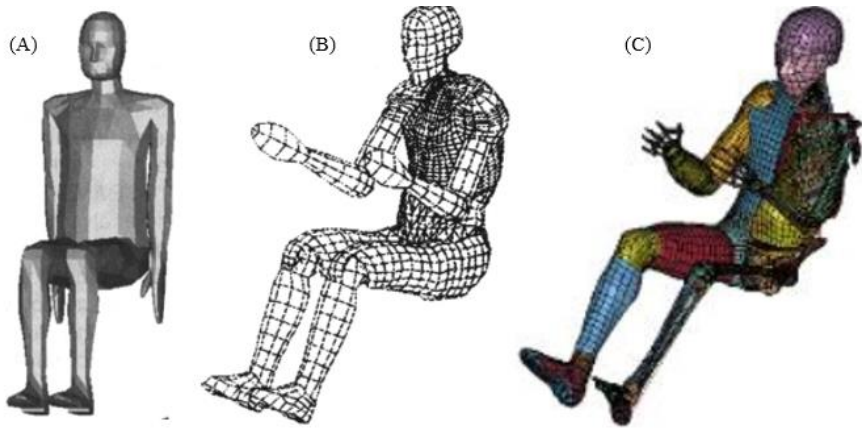

Figure 1.1 MADYMO (A), Radioss (B), and THUMS (C) HBMs. Figures from [13], [15], [18].

The MADYMO model was created based on RAMSIS data by Happee et al., and was composed of 25 rigid bodies for the spine, 7 flexible bodies for the thorax, rigid bodies for the limbs, and a skin surface composed of 2174 triangular facets [13]. This HBM did contain distinct soft tissue features such as individual fingers and toes. There were also early MADYMO models for a child, female, and large male and can be seen in Figure 1.2.

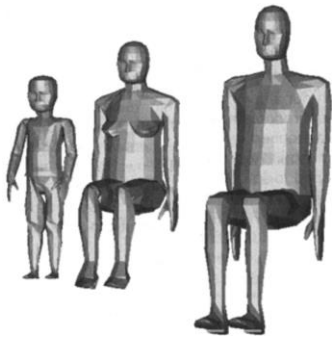

Figure 1.2 Child, female, and large male MADYMO models. Figure from [13].

The Radioss model, created by Lizee et al., was composed of 225 springs, 6308 shell elements, and 3638 solid elements [14]. This model also lacked specific soft tissues such as finger toes, with the limbs being defined only as rigid bodies. It did however have three meshed parts in the abdomen corresponding to the heart and lungs, the spleen and stomach, with the third section corresponding to the lower abdomen organs including the intestines [14]. This model also had some explicitly modeled parts of the torso, which can be seen in Figure 1.3.

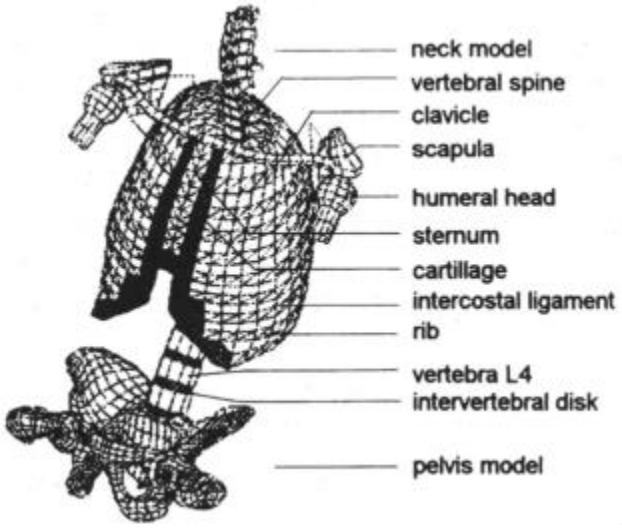

Figure 1.3 Meshed models of skeletal parts of the torso of the Radioss model. Figure from [14].

A standout among early HBMs is the THUMS model from Toyota, with version 1 of the model appearing in May of 2000. It eclipsed the MADYMO and Radioss models of two years prior with its higher complexity and geometric fidelity. THUMS V1 was composed of 83,500 element, with 30,000 falling being solid elements, 51,000 being shell elements, and 2,500 being beam elements [16], [17]. Unlike the MADYMO and Radioss models, THUMS also had modeled and meshed bones in the limbs and even included separate parts defining major organs such as the heart, lungs, stomach, liver, and intestines (see Figure 1.4) [16]. All three of these models were used in the automotive industry for occupant and pedestrian impacts [13], [14], [16], [17].

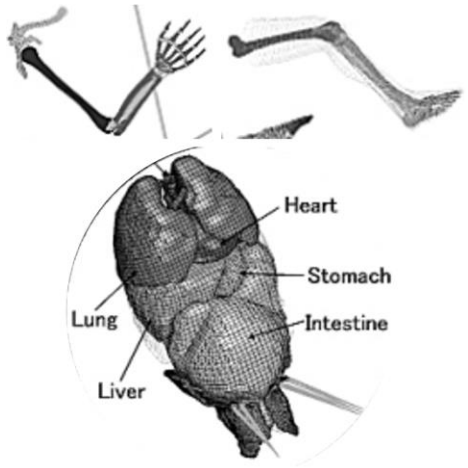

Figure 1.4 Arm, leg, and organs of the THUMS V1 model. Figure from [16].

Outside of vehicle testing, human body modeling also has a place in human injury assessment in sports, where it can be used to reconstruct injury events and test protective sports equipment. In particular, it would allow for considerably rapid testing of helmets using different padding, placement of padding, and shell geometries.

Modern HBMs are much more detailed than their 20 year old predecessors, with higher fidelity to human anatomy and element counts. These models can be licensed from their vendors and used for human injury analysis.

The specific impetus behind the scaling of a HBM gone over in detail later is to fulfill an AFWERX STTR contract in conjunction with Corvid Technologies LLC to develop methods of positioning and scaling of a human body model to evaluate and analyze pilot injury. The need for a scalable human body can be highlighted by the fact that ~90% of males are not of average height and 95% are not of average weight [1]. The work and methods developed from this contract could also be applied to sports injury simulation. Using football as an example space, scaled models are a must if a player collision is to be simulated with the weight of football players ranging from 193 to 315 pounds [19].

1.2 Head Impacts and Helmets

Traumatic brain injuries (TBI), usually resulting from a impact or jolt to the head or body, can have short-term symptoms headache, nausea, dizziness, mood changes, and restlessness in mild cases to loss of consciousness, seizures, slurred speech, and loss of motor control in moderate

to severe cases [20]–[22]. Long-term and permanent symptoms can involve headaches, dizziness, and seizures as well as coma, impaired cognitive function, difficulty communicating, and emotional and behavioral changes in severe cases [20], [21]. From 2006-2014, TBI incidents resulting in seeking emergency care have been rising, with an estimated lifetime cost from moderate to severe TBI coming in at approximately $76.5 billion [23], [24]. In 2014, TBI was the cause of approximately 2.5 million Emergency Department (ED) visits in the United States, with nearly a third of these cases being among children [25]. 283,000 of these ED visits involving children (aged ≤17 years) were sport and recreation related, with 45% being from contact sports [26]. In total, approximately 3.8 million sport and recreation related ED visits for TBI were found for children, with 41% (approximately 1.5 million) being associated with contact sports, with football accounting for most of these [26].

Concussion, a commonly known form of TBI, has a disturbingly high trend among high school student in the U.S. From data in a survey in 2017, 15.1% (nearly 2.5 million) of high school students engaged in sports or physical activity self-reported having had a minimum of one concussion in the previous 12 months, with 6% (nearly 1 million) reporting having had a minimum of 2 concussions [27]. This is startling, as a 2006 estimate of the number of TBIs related to sports was 1.6-3.8 million annually [28]. Starting in 2009, Washington State was the first to implement laws addressing concussion in youth athletics and by 2012 42 states had similar laws; as of now all 50 states have "Return to Play" laws [29], [30]. These laws corresponded to a decreasing trend in ED visit related to TBI around 2012 that has continued to 2018, even with 40% of high school athletes reporting in 2014 that their coaches were unaware of an athlete's symptoms of concussion [26], [31].

Even without diagnosed concussion, medical imaging has shown brain injury in athletes engaged in contact sports [32], [33]. Football players, sustaining nearly a thousand impacts per season, have the chance of sustaining hundreds of sub concussive impacts that can still produce observable structural changes in the brain [34]–[36]. Even at higher levels of play, brain injury is prevalent. Of the approximately 1.1 million athletes who play football in high school in 2016, only 251 made it to the National Football League (NFL) [37]. These lucky (or possibly unlucky) few will continue to hit and be hit on the field and at risk for Chronic Traumatic Encephalopathy (CTE). CTE, characterized by Mez et al. as "a progressive neurodegeneration associated with repetitive head trauma", has been observed in NFL players for nearly two decades with the first appearance

of CTE in a retired NFL player in literature in 2005 [38]. A study from 2017, which evaluated the brains of 202 American football players (111 of whom played in the NFL), 177 were diagnosed with CTE [39]. Of the athletes who made it to the NFL, 110 were diagnosed with CTE [39]. A change in play style may alleviate the number of head impacts, but progressively better protective equipment could help as well.

The first head covering meant to protect the head in football seems to have appeared in 1893 and was made simply of moleskin [40]. The first plastic helmet, which was manufactured by Riddell, appeared in 1993 but lacked the chinstrap and facemask that modern football helmets possess [40], [41]. Helmets have been mandatory in the NFL since 1943 [42].

Even with helmets becoming mandatory in the NFL in 1943, the National Operating Committee on Standards for Athletic Equipment (NOCSAE), with its safety standard that is embossed on myriad athletic equipment today, did not exist until 1970 with the test standard being published in 1973 [43], [44]. All football players in the NFL, NCAA, and those governed by National Federation of State High School Associations (NFHS) rules are required to wear a helmet embossed with the "Meets NOCSAE Standard" phrase and seal on the rear of the helmet [44], [45]. Some modern helmets, each produced by different manufacturers, that have met the NOCSAE testing standards can be seen in Figure 1.5.

The NOCSAE standard for football helmets uses a drop tower and pneumatic ram to test a helmet design's performance. In both setups, the helmets are placed on helmeted headforms. The drop tower tests are conducted such that there are multiple impacts to the helmet at various locations and velocities, as well as at ambient and higher temperatures. The pneumatic ram tests are performed at various locations as well but at a single velocity and temperature. Limits to define a passing grade for a tested helmet are a defined in the form of peak rotational acceleration and peak severity index [46]. The severity index (SI) can be seen below, where T is the duration of the impact and A is the acceleration of the head during impact [47].

$$SI = \int_0^T A^{2.5} dt \tag{1.1}$$

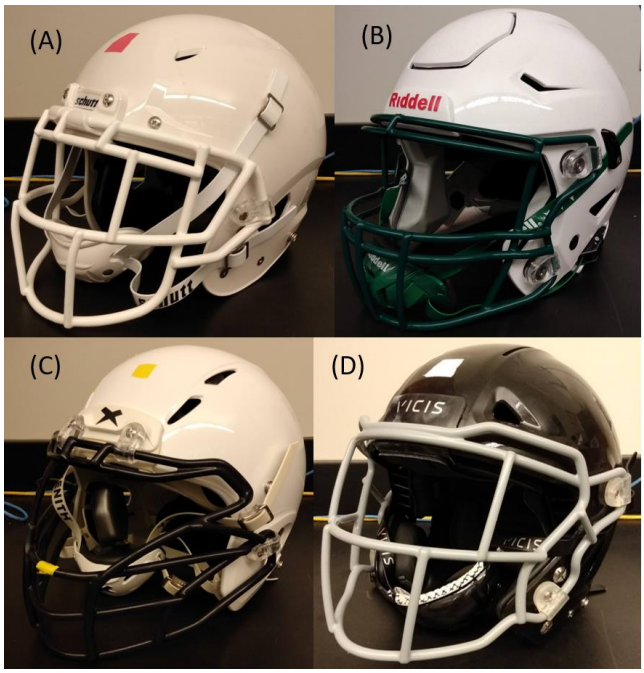

Figure 1.5 (A) Schutt Vengeance Pro, (B) Riddell SpeedFlex, (C) Xenith EPIC+, and (D) VICIS ZERO1 football helmets that have met the NOCSAE standard.

Applying Finite Element Analysis (FEA) to football helmets presents the possibility of research that would be unfeasible or unpractical in an experimental setting. With FE models of helmets, investigating the contribution of individual components of the helmet to energy absorption becomes a workable option. Padding and helmet shell geometries can be modified, and material definitions changed to investigate the impact of different materials. This would allow part switching between helmets within a brand as well as the integration additional energy absorption materials such as newly developed padding materials. This would also allow research into optimizing a helmet to perform better for a position on the field, since different positions experience different impacts [48].

With many helmets having been tested experimentally in the HIRRT Lab, creating a digital twin to the experimental setup would enable further and more varied helmet testing that would prove infeasible to test experimentally. To this end, a FE Hybrid III head and neck model was validated to data from the experimental setup and a FE helmet model was created to be used in evaluating helmet changes.

2. BACKGROUND

2.1 Current Human FE Body Models and their Scaling

Some existing human body models include the GHBMC male 50th percentile model, Toyota's THUMS, HUByx by CEDREM, and CAVEMAN by Corvid Technologies. With the exception of CAVEMAN, these models only come from their vendors in seated and standing positions, with few options for the size of the models.

The Global Human Body Models Consortium (GHBMC) created in 2006, is a global entity with the goal to develop HBMs to "advance crash safety technology", according to their website. Available for license from Elemance, there are 4 50th percentile male HMBs: one each simplified and detailed standing model and one each in the seated position as well. These models can be seen in Figure 2.1. The simplified model consists of ~840 thousand and the detailed model consists of ~2.3 million elements; the standing models have a stature of 175 cm and a weight of 77 kg [49]. Aside from the 50th percentile model, Elemance also has 95th percentile male, 5th percentile female, and 6 year old child HBMs.

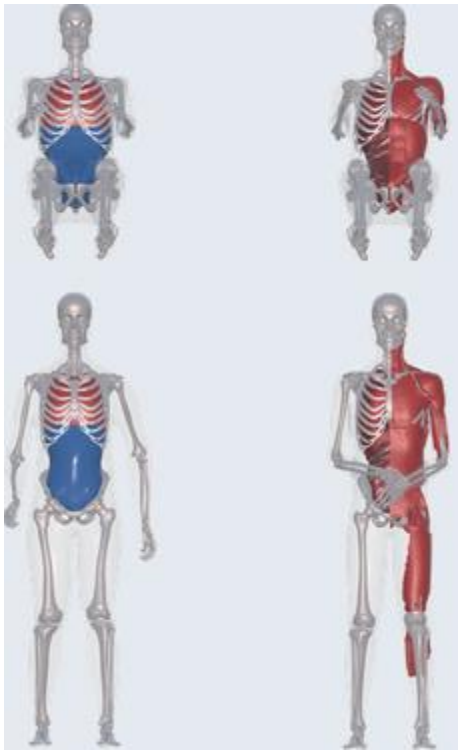

Figure 2.1 Simplified seated and standing GHBMC 50th percentile male models (left) and detailed seated and standing model (right). Figure from [49].

Toyota's Total Human Model for Safety (THUMS), with its 20 year history is currently in its 6th version, which comes in seated and standing positions. The version 4 models for these two positions can be seen in Figure 2.2. The V4 models are shown because seated and standing models of V6 could not be found and V6 is built upon V4 [50]. THUMS V6 has a stature of 179 cm and a weight of 79 kg and is composed of ~1.9 million [51]. THUMS HBMs are also available for a 3 year old, 6 year old, 10 year old, adult female 5th percentile, adult male 50th percentile, and adult male 95th percentile bodies in the standing and seated positions.

Figure 2.2 Seated and standing models of THUMS V4. Figure from [52].

HUByx by CEDREM, a product from Altair, can be seen in Figure 2.3 with less information available. A literature search shows only that there are ~115,000 elements in the thorax with the number of elements in the rest of the body unknown [53], [54].

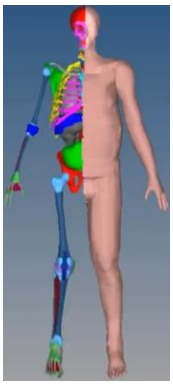

Figure 2.3 HUByx HBM. Image taken from Altair's website.

CAVEMAN from Corvid Technologies (Figure 2.4) was the HBM used for scaling and is composed of ~5.3 million elements. Prior to scaling methods being developed, Corvid already had a seated model as well as software framework to position the limbs to user specifications.

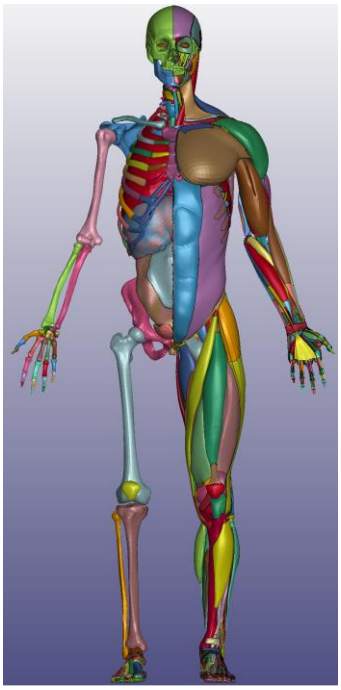

Figure 2.4 CAVEMAN male 50th percentile model from Corvid Technologies.

It is unknown if any of the HBMs besides CAVEMAN were capable of repositioning of the limbs with software from their vendors. A literature search did not reveal any models that were in positions besides sitting and standing. There was however a software framework that can scale the GHBMC and THUMS 50th percentile HBMs.

This framework is called Position and Personalize Advanced Human Body Models for Injury Prediction (PIPER). PIPER became usable under a public release in 2017 with version 1.0.0 and is capable of scaling and positioning and was envisioned to be implementable to different models. Prior to scaling or positioning, a model needs to be prepared. Fortunately, PIPER supports import of LS-DYNA files and the node and element data CAVEMAN in written in a LS-DYNA keyword file. A typical workflow, as outlined in the PIPER user guide and could be applied to the CAVEMAN model, would be to import CAVEMAN, check the model, produce some anthropometric targets, scale CAVEMAN using Kreging interpolation, position CAVEMAN, check element quality and improve it as necessary, and finally export it as a LS-DYNA keyword file but this would all be done by PIPER [55]. As Corvid has already developed a method to position the CAVEMAN HBM, the PIPER workflow would instead be to import CAVEMAN, check the model, produce some anthropometric targets, scale CAVEMAN, check and improve

element quality, and export the scaled CAVEMAN model. Though PIPER is a powerful tool for HBM scaling and positioning, creating a pipeline to connect Corvid's repositioning code to PIPER in order to use its scaling functionality would not be feasible given the millions of different positions that the CAVEMAN model could take. Kriging interpolation has also been used by others to scale HBMs [56], [57].

Kriging interpolation is a method to morph an HBM using control points chosen from nodes of the model, whose initial and final positions must be known, and weightings to determine the final position of the nodes surrounding the control nodes in their initial position whose final positions are not known [55], [56]. These control points could be nodes on the surface of the skin or nodes on the surface of the bones. For example, Jolivet et al. used pairs of control points on the skin that corresponded to anthropometric measurements [56]. An issue with Kriging interpolation is its computational cost when using higher numbers of control points (N) because the covariance matrix used to determine the weights is NxN in size and needs to be inverted to determine weights. An issue with applying Kriging interpolation to scale CAVEMAN is that the model can be positioned in postures besides sitting and standing. Anthropometric measurements are taken on the outside of the body using landmarks such as the radiale and stylion landmarks. The radiale-stylion length is the measured distance between these two landmarks and is taken with the arm relaxed at the side with the palm facing forward [1]. When the elbow is flexed the relative position of the radiale landmark will shift to an unknown degree, affecting the Kriging interpolation in. Additionally, a literature review showed no Kriging model being used on a HBM in multiple positions.

Another scaling method used is radial basis function (RBF) interpolation, which has been implemented by Zhang et al. and McKee [58], [59]. RBF interpolation uses "known vector translations and a vector filed" (McKee) to interpolate the points between control points [59]. A foreseeable issue with using RBF interpolation would be choosing sufficient and appropriate reference points. The scaling performed by McKee and Zhang et al. was done on one model, that could not change position. With CAVEMAN possibly positioned in a multitude of manners, reference points are not guaranteed to work well in all positions the model may take.

What I did, and which no one else has done as far as a literature search revealed, was scale a HBM after positioning. Additionally, the scaling method employed utilized a simpler approach than other methods while still producing acceptable results in a very short timeframe, sufficient

for on the fly scaling of a repositioned model. Also of note was that literature could not be found where a single scaling method was applied to a wide swath of percentile target bodies.

2.2 Helmet Simulations

Prior to FE simulations of helmeted impacts appearing in literature, experiments using helmeted head-forms were used to evaluate helmeted impacts. One outstanding example had instrumented dummies fully kitted out in football padding and helmets and were hung from angled rails and would collide at a prescribed location and velocity (see Figure 2.5) [60]. Other test setups are much simpler, such as the NOCSAE testing methods given earlier.

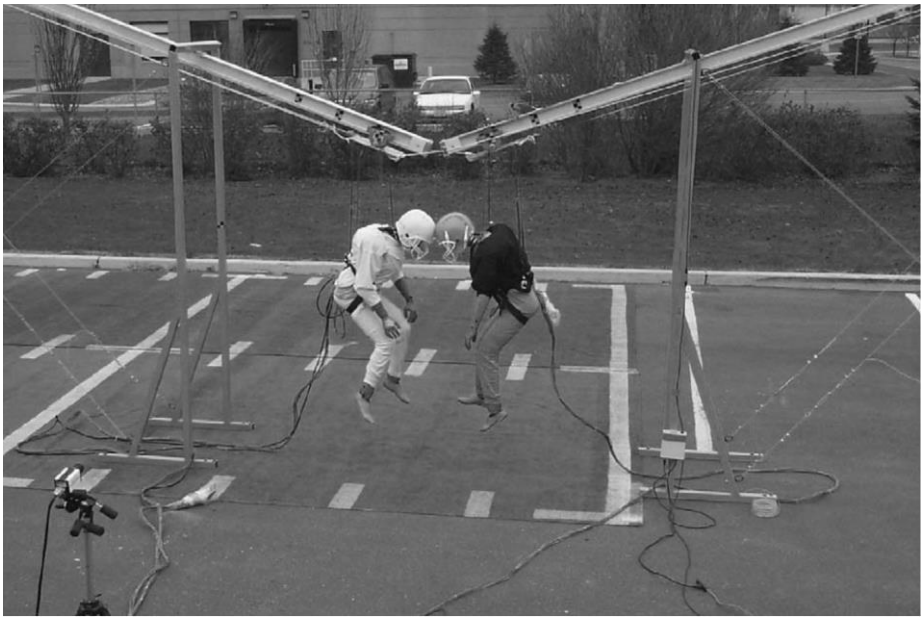

Figure 2.5 Setup of two test dummies set up to simulate a game collision. Figure from [60].

One of the earliest FE helmet simulations found in literature was the simulation of a crash helmet designed to prevent skull fracture in 1992, which consisted of a modest 144 elements inclusive of the skull and helmet [61]. Later, simulations became more complex with tens of thousands of elements, but the helmets simulated were of relatively simple geometry. Two examples from 2011 and 2012 are simulations of a motorcycle helmet composed of 34 thousand elements and an Advanced Combat Helmet (ACH) with pads, like the one pictured in Figure 2.6 [62], [63].

Figure 2.6 ACH helmet similar to the one simulated by Moss et al. in 2011.

One of the earliest football helmet FE simulations found in literature comes from Johnston et al. and investigated the implementation of a novel padding system to reduce rotational acceleration in a Schutt ION4D helmet [64]. In this article however, the simulations are second string when compared to the experimental testing, but the data generated from simulation was used to inform design decisions in the prototyping of the padding. This use of simulation to augment and inform experimental prototyping and design in helmet testing still had great potential towards the endeavor to develop better helmets.

An early standout among football helmet FE simulation was conducted by Darling et al in 2016. They simulated a football helmet, without facemask or chinstrap, on the GHMBC full body model and simulated the effects of hits at different location on the helmet [65]. It is worth noting that the article purports to use the Riddell Attach Revolution Youth helmet for geometry reference, the modeled helmet bears a greater resemblance to the Riddell VSR-4 helmet. Also worth mentioning is that the article uses the Revolution helmet to validate the modeled helmet, which deserves scrutiny due to the differences between the modeled helmet and the Revolution helmet.

After these two early examples of helmet simulation, there was gap in literature until 2020. This comes around after the time of the first public release of 4 meshed football helmet models from Biomechanics Consulting and Research (BioCore) LLC [66]. These 4 helmets were developed as a collaborative project between BioCore, Football Research Inc, the NFL, and university partners. The four helmets are the 2017 Vicis 01, 2016 Riddell Revolution Speed Classic,

2016 Xenith X2E, and 2016 Schutt Air XP Pro created with University of Virginia, KTH Royal Institute of Technology, University of Waterloo, and Wake Forest School of Medicine university partners respectively. At the time of writing, there are two versions of each helmet available on BioCore's website, with version 1 being publicly released in May 2018 and version 2 being released in September 2019.

Since the release of the Biocore models, relatively few articles were found that simulated modern football helmets. Among 5 article that use a BioCore model since the release of the models in 2018, 4 articles included authors that were directly related to the development of the BioCore models or whose names are included among the authors in the user manuals for the helmet.

Two studies were found that used the BioCore 2016 Xenith X2E, both having authors from the University of Waterloo team that developed the helmet. The first article by Corrales et al., from 2020, read like an extension to the user manual they developed for BioCore, which is currently available via BioCore's website [67], [68]. Something that the article contained that the manual did not was acceleration traces for some impacts, but the main focus of the paper was evaluate the energy distribution of the components of the helmet at different velocities and locations [67]. The second study sought to simulate and compare brain response under impacts with differing boundary conditions. One boundary condition employed to was prescribed skull kinematics, where experimental translational and rotational acceleration were used to accelerate the HBM head. The second boundary condition used a linear impactor hitting the helmeted HBM head with and without muscle activation in the neck[69]. The response of the brain was evaluated by examing strain in the brain [69].

Decker et al., from Wake Forest School of Medicine, similarly wrote an article that read like an extension to the manual developed for the 2016 Schutt Air XP Pro for BioCore [70], [71]. The university partner at University of Virginia that developed the VICIS 01 helmet also published a paper similar in structure to the articles by Decker et al. and Corrales et al, but also developed the dummy and impactor models used in the BioCore models [72], [73].

One journal article was found that used the BioCore 2016 Riddell Revolution Speed Classic helmet. The article was written by Mills et al. and sought to investigate the effect of different foams in the helmet effecting the linear acceleration of a headform [74]. It was the among the first, if not the first, study to investigate this [74]. This was the only article found using a BioCore helmet model that did not have authors associated with the development of the helmets.

3. CAVEMAN HUMAN FINITE ELEMENT MODEL SCALING

3.1 Overview

CAVEMAN, a product of Corvid Technologies LLC, is a HBM that was developed using the highly comprehensive and medically accurate CAD from the ZYGOTE Solid 3D 50th Percentile Male Model [75], [76]. CAVEMAN has multiple iterations and the version used in the final scaling method was Version 21.4. This version is composed of 5.3 million elements, 6.7 million nodes, and over a thousand parts which includes bones, muscles, tendons, ligaments, cartilage, organs, skin, and void fill. The void fill was created to fill in any voids between tissues and ensure load transmission between soft and hard tissues [76]. Among the parts are 258 parts that define cortical and cancellous bone, 397 muscles/tendons, 342 ligaments, 16 organs, and the skin [76].

Development of positioning (developed and implemented by a team at Corvid) and scaling (developed by me) methods were made in order to be able to produce user specified percentile male HBMs that would be used to model and predict injury. Positioning of CAVEMAN would occur first, after which the data defining the repositioned body would be input into the scaling code.

Given that positioning of the body would occur prior to scaling, it was important to know the bounds within which the CAVEMAN model would be positioned. The model was capable of movement in the elbows, hips, knees, and ankles with parameters defining the bounds of flexion. These parameters were ±20º flexion and extension of the foot at the ankle, 0-110º flexion of the knee, 0-90º hip flexion, 0-90º elbow flexion, and a seated and standing posture for the torso. The positioning of the joints could be done in 1º increments. With these user defined positioning parameters, there are 75.3 million positions that the body could take. If all nodal coordinate data for all the possible data were to be saved, this would result in approximately 37 petabytes of data. Keep in mind that this is before any scaling is applied to the positioned models.

Scaling of the body needed to be informed by anthropometric measures and the model needed to be scalable to stature and weight targets from the 5th to 95th percentile targets in 1 percentile increments. The percentile target would be met on the nominal standing position, seen in Figure 3.1, and the relevant scaling values would be used to scale the body regardless of body position.

With the combination of positioning and scaling there are 6.8 billion models that could be generated, which would result in approximately 3.4 exabytes (3400 terabytes) of data purely describing nodal coordinate positions. With such potential for large datasets, the scaling code was developed to be as computationally efficient as possible and perform scaling on the fly of the repositioned model being fed in.

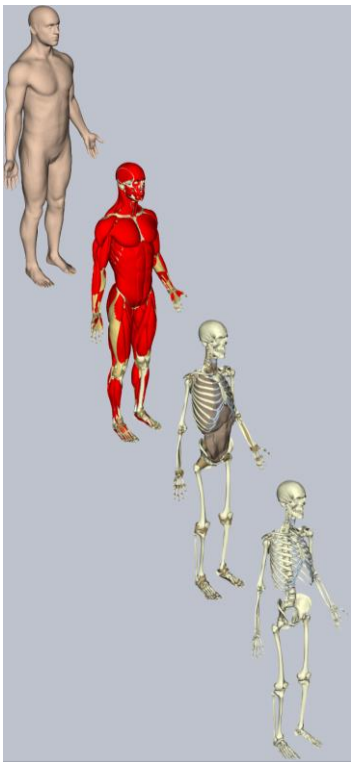

Figure 3.1 CAVEMAN HBM and its layers in the standing nominal position. Figure from [76].

MATLAB, a MathWorks programming platform, was used to develop and preform the scaling of the CAVEMAN HBM [77]. LS-PrePost, a Liverpool Software Technology pre- and post-processing software, was used to visually interact with the original 50th percentile CAVEMAN model and visually check scaled models [78].

3.2 Methods

Before working to scale the entire CAVEMAN HBM, the left leg was chosen as a testing platform for scaling methods. The left leg, with over a million nodes, have the three joints of the hip, ankle, and the knee with its largest positioning range of 110º was chosen to test scaling methods.

3.2.1 First Scaling Method Using Global References

The left leg, which lay along the global y-axis in the nominal, unbent position was chosen as a testing area for methods of scaling. In order to preserve the geometry of the joints, 1D scaling was only performed along the axis of the leg. The first scaling method involved visually identifying nodes on the surface of the leg that would be used to scale it in the global y direction. Two nodes, distal to the knee and proximal to the ankle, were chosen to scale the lower leg. Analogously, two scaling nodes were chosen for the upper leg, with one being distal to the hip and the other being proximal to the knee (see Figure 3.2). Scaling was done using the global y-position to determine whether a node would be scaled or translated. Scaling started in the femur with establishing what nodes had a y value between the range defined by points 1 and 2's y values. These nodes between points 1 and 2 would then be scaled according to user-defined input and shift to the right (or left), resulting in lower (or higher) y values than before and the shift of point 2's position. The points to the right of point 2 would then be translated in the -y direction. The process would then repeat with the nodes between points 3 and 4 scaling to the right (or left), and the points to the right of point 4 being translated.

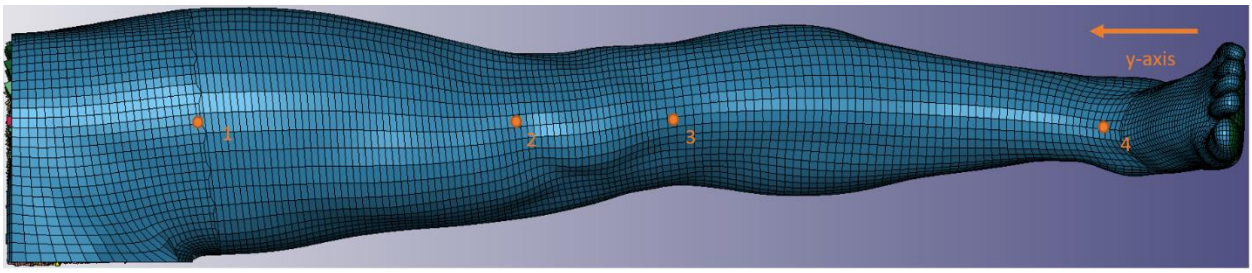

Figure 3.2 Unscaled left leg with points chosen for scaling.

3.2.2 Description of General 1D Scaling Method Using Local References Based on First Scaling Method

This rudimentary scaling method using global coordinates functions for the nominal position of the leg but would not function appropriately when the hip, knee, and(or) ankle are repositioned. This method would also inevitably function inappropriately in the other sections of the body to be repositioned and scaled. These scaling sections (see Figure 3.3) are the torso (including the head and neck), the upper and lower parts of the arms, and the upper and lower parts of the legs.

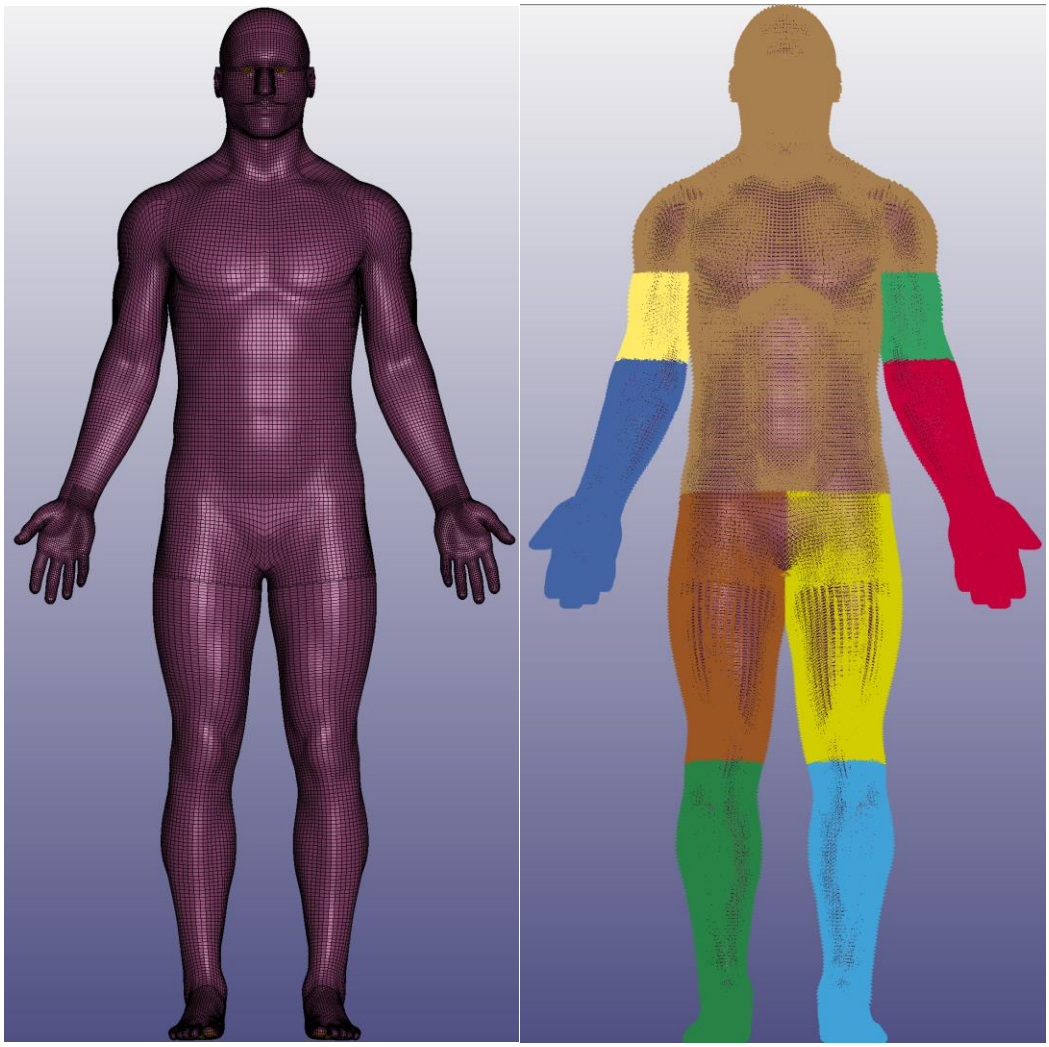

Figure 3.3 Nominally positioned, 50th percentile male CAVEMAN FE model (left) and scaling sections of said model (right).

A different but similar method of scaling was devised that would make use of the nodes of the model. When repositioning a joint, the soft tissue would inevitably shift and change their relative positions, therefore the soft tissue was unsuitable to be used as reference geometry for scaling. This left the bones as the obvious choice to use as references when scaling.

Continuing to use the left leg as a testing area, the soft tissue was turned off in the model so that only the bones of the leg were visible. From these bones, 4 nodes were chosen to be used for scaling the upper and lower leg. For both sections, nodes (dubbed scaling nodes) were chosen from the bones that lie outside the areas of joints so that the 1D scaling would not affect the geometry of the joints. For each scaling section there is a proximal and distal scaling node. The same

methodology was used to scale the upper and lower leg, which will be described in general terms. To determine where a node should be scaled in a scaling section, components were used; see Equation (3.1). The component of **u** with respect to **v,** is the magnitude of **u** that lies along the vector **v**. The vector **u** (scaling vector) would be defined as the vector whose tail is the proximal scaling node of the section and whose head is a node in the scaling section. The vector **v** would be defined as the vector whose tail is the proximal scaling node of the section and whose head is the distal node of the scaling section. Therefore, if the component of **u** along **v** was greater than zero and less than or equal to the magnitude of **v**, the node would be flagged for scaling. This component calculation would be done for all nodes in the scaling section. The nodes in the scaling section that had components greater than the magnitude of **v** were flagged for translation.

$$comp_{\boldsymbol{v}}\boldsymbol{u} = \frac{\boldsymbol{u}\cdot\boldsymbol{v}}{\|\boldsymbol{v}\|} \tag{3.1}$$

After determining which nodes are to be scaled, their scaling is not performed all at once but in slices. The nodes are scaled in 1 mm intervals, forming "n" slices of nodes, for the length of the scaling vector. The user input length change to the magnitude of **u** is defined as "dL_u", the quantity dL_u/n shall be referred to as "d_n" for convenience, and $\hat{u}$ is the unit vector of **u**. To be scaled, the nodes in every n^{th} slice would $n*d_n*\hat{u}$ added to their coordinates. After scaling all the nodes that lie in the n slices, there can be some nodes that were flagged for scaling but were not scaled because $\|\mathbf{u}\|/n$ did not have a remainder of zero. These nodes are reflagged for translation. Once scaling is done all nodes flagged for translation are translated by $dL_u*\hat{u}$.

3.2.3 1D Scaling all Sections of the Body

Figure 3.4 shows the locations of all the scaling nodes. The body is scaled from the head to the feet and the first section to be scaled is unique among the scaling sections; the torso has two pairs of scaling nodes for scaling the neck and the torso below the neck. The neck is scaled first using nodes from the C3 and C7 vertebrae to define the scaling vector and scaling is informed by the neck link anthropometric measurement which can be seen in Appendix A (as will the rest of the anthropometric measurements used to inform scaling of the body). The nodes between the neck scaling nodes are scaled in the direction of the scaling vector and afterwards the nodes below the

inferior neck scaling node are then translated by dL_u*û relevant to the neck. The next section to scale is the torso and this scaling is done using nodes from the T5 and L5 vertebrae and is informed by the waist back length anthropometric measurement. This scaling is also unique among the rest in that scaling of the torso affects the upper arms as well, but does not change the 3D geometry of the shoulder joint. This scaling of nodes between the T5 and L5 would, if unchecked, cause elements from the torso and upper arms scaling section to overlap but this was compensated for by tracking the movement of nodes at the edge of the torso scaling section bordering the upper arm scaling sections and measuring how far they were scaled. This measured movement of the border nodes was then used to translate the arm nodes along the scaling vector of the torso. The nodes of the leg scaling sections would then be translated by the usual dL_u*û relevant to the torso scaling. The following scaling of the upper and lower arms and legs all follow the basic scaling methodology described in section 3.2.2. The upper and lower arms scaling is informed by the acromion-radiale length and radiale-stylion length anthropometrics measurements, respectively. The upper legs scaling is informed by the difference between the anthropometric measurements of the buttock height minus the knee height (midpatella), while the lower legs scaling is informed by the knee height (midpatella). As evident from the figures in Appendix A, values were not given for the percentiles between 5 and 95 that were not divisible by 5. These in-between values were approximated using linear interpolation between the given values.

This scaling method resulted in approximate values for stature but not weight. The 5^{th} Percentile model was over a dozen kg overweight while the 95^{th} Percentile model was nearly 10 kg underweight. This necessitated a modification to the scaling of the model to meet stature and weight targets.

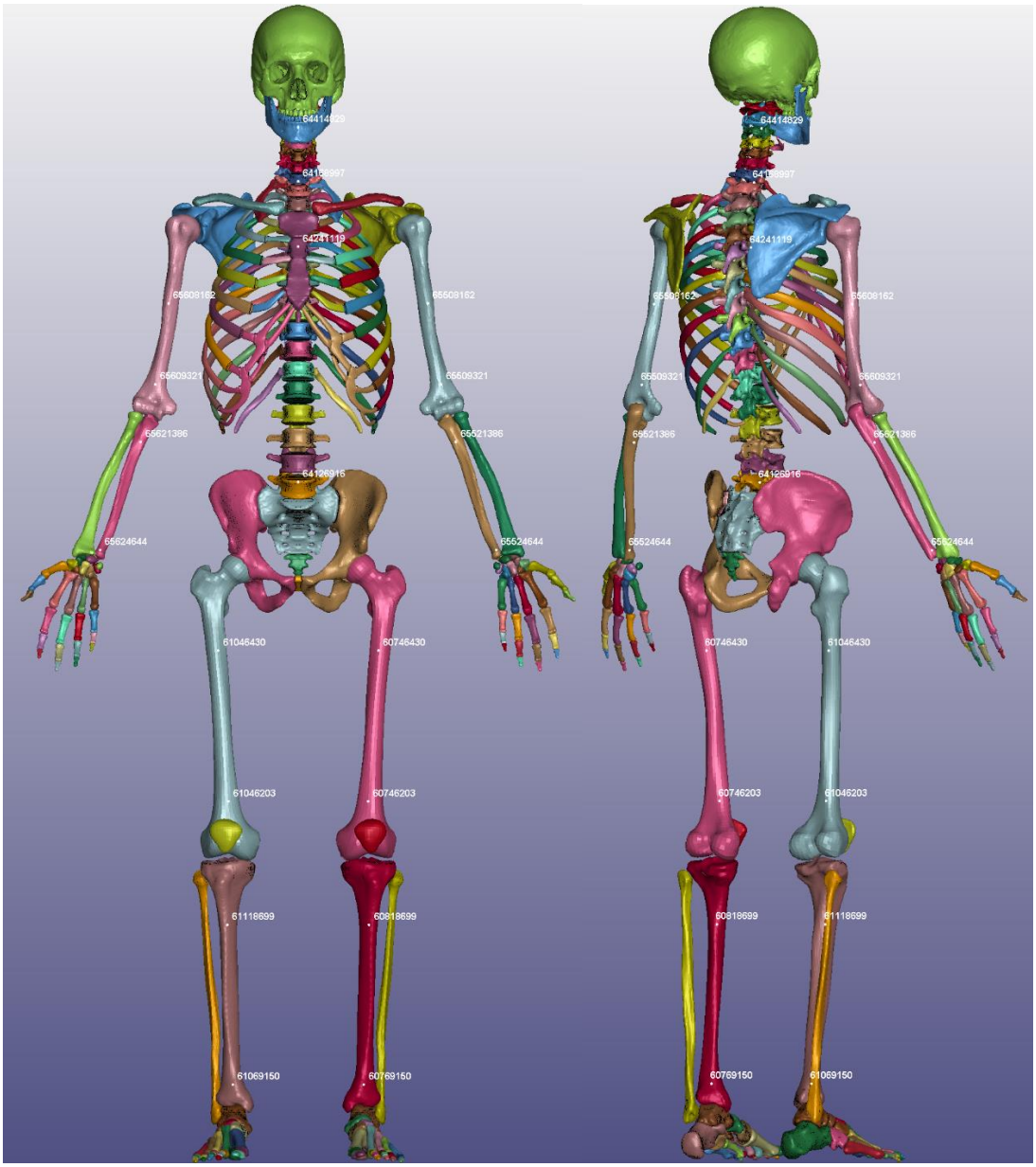

Figure 3.4 Skeleton of CAVEMAN model showing locations of the scaling nodes.

3.2.4 Final Scaling Method Using Combination of 3D and 1D Scaling

The method to achieve the stature and weight target was to employ a combination of 3D global scaling of the model and the previously defined method of 1D scaling of the scaling sections. An iterative process was used to determine the combination of 3D and 1D scaling necessary to meet target values. The 50th percentile model would be 3D scaled so that the target stature was met and then the weight of this model was calculated. If the 3D scaled model was too

heavy, the value used to 3D scale was decreased and the 1D scaling was applied to the scaling sections to achieve the stature target. Analogously, when the 3D scaled model was too light, the value used to 3D scale was increased and the 1D scaling was applied to the scaling sections to achieve the stature target. During the 3D scaling, the code used to perform 1D scaling would keep track of the 3D scaling's effect on the scaling sections and factor this effect into the 1D scaling. This combined scaling method was used to iterate for all target percentiles until the target stature and weight was reached, whereupon the 3D and 1D scaling variables would be saved for each percentile. These saved variables would be used to define the 3D and 1D scaling to reach the percentile target as defined by the user.

The method used by Corvid to measure the stature of the model is unknown, but this was a moot issue. Checking the stature of the standing model is a trivial matter as the nominal model is standing erect in the y axis. Measuring stature was as simple as finding the nodes with the maximum and minimum y values and taking the difference between them. The method used to determine the weight of the model during iteration is different than the method employed by Corvid Technologies. Corvid would load the model in the simulation environment, which can measure the mass of the simulation, or they would load the model in LS-PrePost and incorporate a special file that had the appropriate densities of the various parts of the CAVEMAN model and then measure the mass. Both methods for checking mass were manual and required user involvement, which made them unsuitable for repeated uses during the iteration process for reaching stature and weight targets. This resulted in a mass measurement function created to measure the stature and weight of the model at each iteration for each percentile. The function had the data for what nodes belonged to which elements, which elements belonged to which parts, and the densities for the various parts. For each solid element, the volume would be calculated based on the positions of its constituent nodes and was subsequently multiplied by the density of the part to which it belonged to calculate the weight of each element. All these solid element weights would be summed together, resulting in the solid element weight. Each shell element would then have its area calculated, have this area multiplied by the thickness and density specified for the part to which it belonged, and these shell elements would be summed together as the shell element weight. The solid and shell element weights would be added together for the mass of the scaled model. An issue experienced when comparing this calculated mass to the mass found by Corvid technologies was that there was a slight difference; the mass calculated via the mass checking function was

consistently higher than that determined by Corvid, but by less than 0.5 kg. The cause between the weight difference could not be identified and was labeled as not an issue given the relatively small difference between the measured weights.

The pipeline for the creation of a repositioned, scaled CAVEMAN starts with a user defining the metrics for repositioning of the CAVEMAN model and the percentile of the scaled body. The body would be repositioned using code developed at Corvid Technologies. This code would call my scaling code, give it the target percentile and the nodal coordinates of the repositioned body. My scaling code would then scale the body using the previously saved variables, regardless of body position.

3.3 Results

3.3.1 Full Body 1D Scaling

Table 3-1 shows the original full body 1D scaling gone over in section 3.2.3 for the 5th and 95th percentile models. While the stature was nearly at the target values for the given percentiles, the weight was far from acceptable. This led to the revised method of scaling using 1D and 3D scaling.

Table 3-1 Comparison of 5th and 95th percentile 1D scaled model metrics compared to ANSURII values. Scaled CAVEMAN weight was calculated by Corvid [79].

Metric	ANSURII 5th percentile	Scaled CAVEMAN 5th Percentile	Percent difference	ANSURII 95th percentile	Scaled CAVEMAN 95th Percentile	Percent difference
Stature (cm)	164.70	167.02	1.41%	187.30	191.51	2.25%
Weight (kg)	62.48	80.78	29.29%	101.72	93.00	8.57%
Bideltoid breadth (cm)	45.40	50.15	10.46%	54.40	50.17	7.75%
Chest depth (cm)	21.00	26.00	23.81%	28.20	25.82	8.44%
Waist depth (cm)	18.20	22.17	21.81%	26.39	22.14	16.10%
Waist breadth (cm)	26.60	30.71	15.45%	36.20	30.47	15.83%

3.3.2 Full Body Combined 1D/3D Scaling

Table 3-2 shows the scaled results for the 5th and 95th percentile models using the combined 1D and 3D scaling method described in section 3.2.4. Stature was within less than a millimeter of the target and mass was within a kilogram, both being acceptable.

Table 3-2 Comparison of 5th and 95th percentile 1D and 3D scaled model metrics compared to ANSURII values. Scaled CAVEMAN weight was calculated by Corvid [80].

Metric	ANSURII 5th percentile	Scaled CAVEMAN 5th Percentile	Percent difference	ANSURII 95th percentile	Scaled CAVEMAN 95th Percentile	Percent difference
Stature (cm)	164.70	164.69	0.01%	187.30	187.33	0.02%
Weight (kg)	62.48	63.40	1.47%	101.72	102.50	0.77%
Bideltoid breadth (cm)	45.40	44.60	1.76%	54.40	53.90	0.92%
Chest depth (cm)	21.00	22.10	5.24%	28.20	28.00	0.71%
Waist depth (cm)	18.20	19.60	7.69%	26.39	24.10	8.68%
Waist breadth (cm)	26.60	27.50	3.38%	36.20	36.10	0.28%

Tables 3-3 and 3-4 contain data comparing the ANSURII and scaled CAVEMAN values for stature and weight. The weight shown in these tables are the weights calculated by the mass measurement function. The stature of the seated models relevant to Table 2-4 are not given as the exact variables used to scale the nominal standing model were used to scale all positions the body may take, including a seated position. The largest difference between the stature of the standing scaled CAVEMAN models and the ANSURII values was 0.03 cm, a difference of 0.015%; the largest weight difference was 1.33 kg, a 1.98% difference. The largest weight difference between the scaled seated models and the ANSURII values was 1.02 kg, a 2.83% difference. These difference between the scale weight and the target weight were less than the standard deviation observed for the mean weight. A result of note that needs to be made clear is that the seated scaled models were consistently lighter than the target weight and the nominal standing models were consistently heavier that the weight target.

Table 3-3 Comparison of ANSURII and scaled CAVEMAN statures and weights for the 5th to 95th percentile in increments of 5 percentiles.

Percentile	Target Stature (cm)	Scaled Stature (cm)	Stature Difference (cm)	Stature % Difference	Target Weight (kg)	Scaled Weight (kg)	Weight Difference (kg)	Weight % Difference
5	164.70	164.69	-0.01	0.005%	62.48	63.71	1.23	1.98%
10	166.50	166.50	0.00	0.002%	65.70	66.84	1.14	1.73%
15	167.73	167.73	0.00	0.001%	68.50	69.75	1.25	1.83%
20	169.30	169.30	0.00	0.001%	70.40	71.63	1.23	1.74%
25	170.75	170.75	0.00	0.001%	71.90	73.09	1.19	1.66%
30	171.70	171.70	0.00	0.002%	73.60	74.78	1.18	1.60%
35	172.50	172.51	0.01	0.003%	75.00	76.21	1.21	1.62%
40	173.28	173.29	0.01	0.004%	76.60	77.77	1.17	1.52%
45	174.30	174.31	0.01	0.005%	77.90	79.12	1.22	1.56%
50	175.00	175.01	0.01	0.006%	79.90	81.09	1.19	1.49%
55	175.90	175.91	0.01	0.007%	81.40	82.58	1.18	1.45%
60	176.70	176.71	0.01	0.008%	83.10	84.41	1.31	1.58%
65	177.50	177.52	0.02	0.009%	84.87	86.16	1.29	1.52%
70	178.64	178.66	0.02	0.009%	86.60	87.91	1.31	1.51%
75	179.80	179.82	0.02	0.010%	88.25	89.51	1.26	1.43%
80	181.30	181.32	0.02	0.011%	90.80	92.07	1.27	1.40%
85	182.77	182.79	0.02	0.011%	93.13	94.24	1.11	1.19%
90	184.98	185.00	0.02	0.012%	96.52	97.66	1.14	1.18%
95	187.30	187.33	0.03	0.015%	101.72	102.87	1.15	1.13%

Table 3-4 Comparison of the ANSURII weight and the seated scaled CAVEMAN weight for the 5th to 95th percentiles in increments of 5 percentiles.

Percentile	Target Weight (kg)	Scaled Weight(kg)	Weight Difference (kg)	Weight % Difference
5	62.48	61.46	-1.02	1.63%
10	65.7	64.45	-1.25	1.90%
15	68.5	67.24	-1.26	1.84%
20	70.4	69.04	-1.36	1.93%
25	71.9	70.46	-1.44	2.00%
30	73.6	72.08	-1.52	2.07%
35	75	73.45	-1.55	2.06%
40	76.6	74.94	-1.66	2.17%
45	77.9	76.24	-1.66	2.13%
50	79.9	78.12	-1.78	2.23%
55	81.4	79.55	-1.85	2.28%
60	83.1	81.30	-1.80	2.16%
65	84.87	82.98	-1.89	2.23%
70	86.6	84.66	-1.94	2.24%
75	88.25	86.20	-2.05	2.33%
80	90.8	88.66	-2.14	2.36%
85	93.13	90.74	-2.39	2.57%
90	96.52	94.02	-2.50	2.59%
95	101.72	99.01	-2.71	2.67%

Figure 3.5 shows the 5th, 50th, and 59th percentile models side by side. More figures comparing different aspects of the comparison in size between the 5th, 50th, and 95th percentiles can be seen in Appendix B.

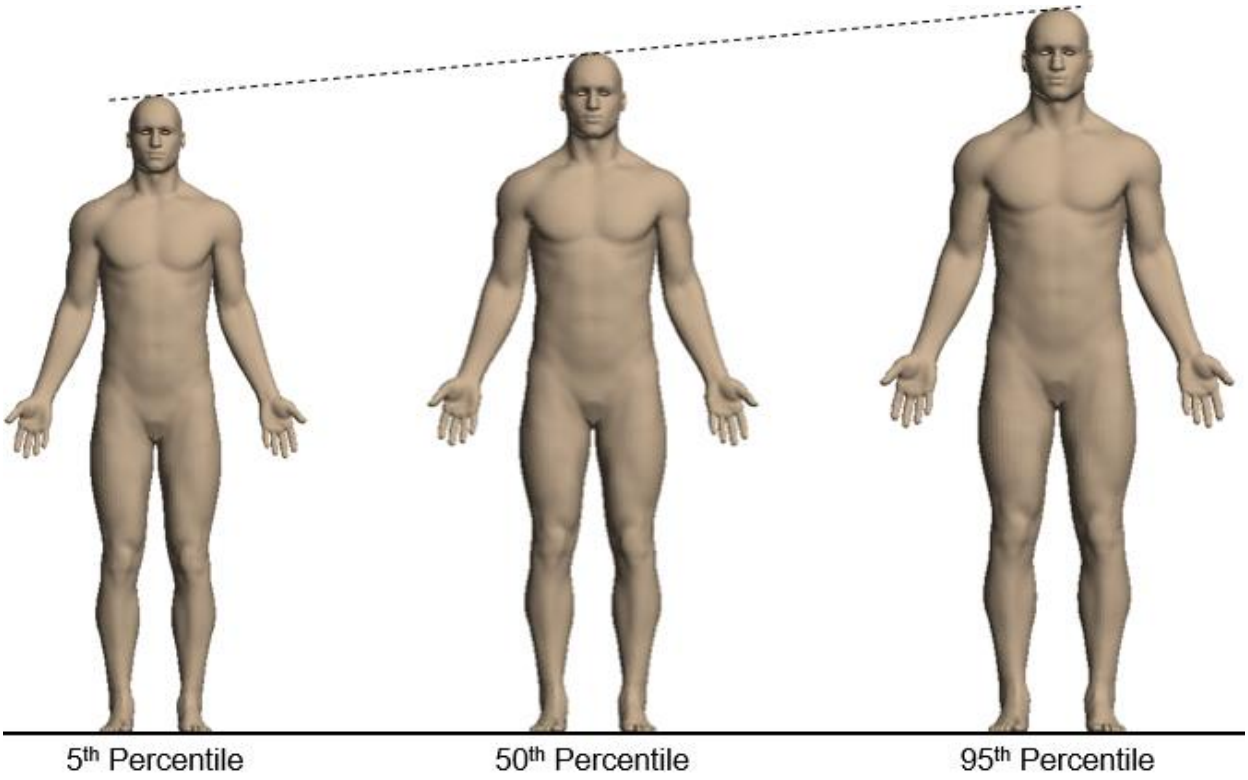

Figure 3.5 Side by side comparison of 5th, 50th, and 95th percentile models, standing in the nominal position. Figure from [80].

3.4 Discussion

The goal of this project was to create a code pipeline that would scale the CAVEMAN model to a target body percentile, regardless of the position of the limbs within the prescribed limits of the repositioning method developed at Corvid Technologies LLC, to facilitate simulations of bodies from the 5th to 95th percentile and in positions besides standing. A combination of 1D and 3D scaling was found to result in models with appropriate stature and weight in the standing position, and appropriate weight in other positions.

The first iteration of the scaling code using only 1D scaling resulted in models that were close to the target statures but fell short of the weight targets. This result prompted a refinement of the scaling code to incorporate 3D scaling to solve the issue of the weight being considerably far from target values in the percentile extremes and resulted in models that were closer to target stature as well. The difference in weight between a xth percentile standing model vs seated model was deemed acceptable by myself and the team at Corvid, as a human's body weight will fluctuate [81]–[83], and it would be unacceptable to use different scaling metrics for an xth percentile model

in different positions. The difference in weight between positioned models of an x^{th} percentile model were outside the control of the scaling code and was attributed to the repositioning code, as the mass of the nominal standing 50^{th} percentile had a different mass than the seated model.

Creation of scaled models outside of the 50^{th} percentile proved to be a non-intuitive process because of the nature of being outside the mean. The 50^{th} percentile model has average anthropomorphic measurements across the board, but a human with 5^{th} or 95^{th} percentile stature and weight may not have all other anthropometric measures in the 5^{th} or 95^{th} percentile. Looking at the isolated case of the 5^{th} and 95^{th} percentile measurements in Table 3-2 one can see that the given measurements of the scaled model are qualitatively close to those of the ANSURII values. This may indicate a trend in body proportions in a subpopulation, namely the subpopulation of U.S. Marines who participated in the anthropometric survey, but further analysis would be required to determine if this trend has statistical significance.

The method used for 1D scaling performed the scaling in what could be dubbed a "digital" fashion where sections of nodes were moved at a time to achieve a sort of scaling. A method that could have been used to achieve a "analog" scaling would be through the use of coordinate transformations. Taking for example the left leg, the scaling axis of the upper leg section could have been used to define one of the local coordinate axes, with bone nodes used to define the other two local coordinate axes. A transformation matrix could then transform the coordinates of the nodes of the leg from the global reference frame to the local reference frame, and with the local y axis pointed along the axis of the upper leg, the y values for the scaling nodes could have been multiplied by a scalar to be scaled. After this the nodes distal to the upper leg scaling section could be translated in the y axis and a similar process would happen with the lower leg. This method was not investigated due to the idea coming late in the development of the scaling code. By that time, the scaling code functioned quickly and without issue, precluding the need to develop a new scaling method.

The final code framework was composed of 4 functions. The top level function, referred to henceforth as "Body Scaler", was where a user would define the target percentile and where the 3D scaling of the nodal coordinates took place. Following this, the 3D scaled nodes and their coordinate data were passed on to the function that would return the nodes after the scaling sections had all been scaled; this function will be referred to as Full Body 1D Scaler (FB-1DS). Before any sections were scaled, the nodes were first run through a preprocessing code necessary to local 1D

scaling. The preprocessing code would sort the nodes into their respective scaling sections. These sections were denoted by another column being added to the matrix containing an integer corresponding to the appropriate scaling section. The single matrix of would then be separated into nine matrices corresponding to the 9 scaling sections and these matrices would be returned to the calling function. With the returned matrices, the FB-1DS would pass scaling section nodes and scaling variables to the Local Section Scaler one at a time, resulting in the Local Scaler being called 6 times. After this the scaled nodes would be passed back to the Body Scaler. During the development process, Body Scaler would then print out the nodes and their coordinates to a LS-DYNA keyword file, which could be imported, without offset, onto the positioned caveman model. When integrated with the body positioning code from Corvid, Body scaler simply passed the Node data back to the positioning program. The final code framework was 400 lines long.

A critical part of the scaling code that has not been expounded upon yet in this chapter is the optimization of the code. The original leg scaling described in section 3.2.1 took an hour to finish scaling just 1 leg. This code could be described as absurdly serial. One operation was performed at a time, with overused nested for loops. Through the influence and guidance of a colleague (Kevin McIver), steps were taken to vectorize and parallelize the code to improve performance. Instead of operations being performed one at a time on single variables in a vector using a for loop, operations were performed on entire vectors, drastically reducing compute time. In contrast to the original hour spent to scale the left leg alone, these optimizations made it possible to scale and measure the stature and weight of all 91 possible standing models in a comparably short 2.8 hours. This time is used to illustrate the orders of magnitude difference in compute time given optimization, as mass does not need to be calculated every time a body needs to be scaled. Scaling all possible standing models without measuring weight takes a mere 13.6 minutes, with the scaling of a single target percentile model taking less than 30 seconds in MATLAB. Code optimization and vectorization made the on-the-fly scaling of repositioned body models possible in a reasonable time and were key to the usability of the code.

4. CREATION OF DIGITAL TWIN TO EXPERIMENTAL HIRRT LAB HELMET TESTING SETUP

Material in this chapter will appear in a journal application. Co-authors for this paper would include Kevin McIver, who provided input for data processing code optimization, and Dr. Eric Nauman and Dr. Thomas Talavage, advisors.

4.1 Overview

The Human Injury Research and Regenerative Technologies (HIRRT) Lab has had a keen interest in human injury, particularly in football, for several years. The HIRRT Lab designed, developed, and fabricated its helmet testing setup in the mid-2010s composed of a instrumented Hybrid III head and neck mounted to a heavy steel block. The helmet testing setup was novel and differed from NOCSAE in that the testing setup could measure input and output parameters in the form of impulse as an input, and translational and rotational accelerations at the headform's center of mass as outputs [84], [85]. The setup was also novel in that it did not rely on linear impactors such as a drop tower, pneumatic ram, or pendulum. Impacts are delivered to the headform with an impulse hammer swung by a researcher in both barehead and helmeted cases.

During experimental testing from the Cummiskey et al. paper, the hit locations were the forehead, forehead oblique, front boss, side, rear boss, rear boss oblique, back, top, and facemask (see Figure 4.1) [84]. Each helmet would receive 20 hits to each location, with 4 hits falling into the impulse ranges of 2-4 Ns, 5-7 Ns, 8-10 Ns, 11-13 Ns, and 14+ Ns [84]. After the submission of the Cummiskey et al. paper and acquisition of Speedflex helmets, and a new impact location was suggested for future testing so that impacts on the cutout of the Speedflex "horseshoe" (see Figure 4.1) could be compared across helmets since the horseshoe cutout is such a stark departure from the design of other modern helmets.

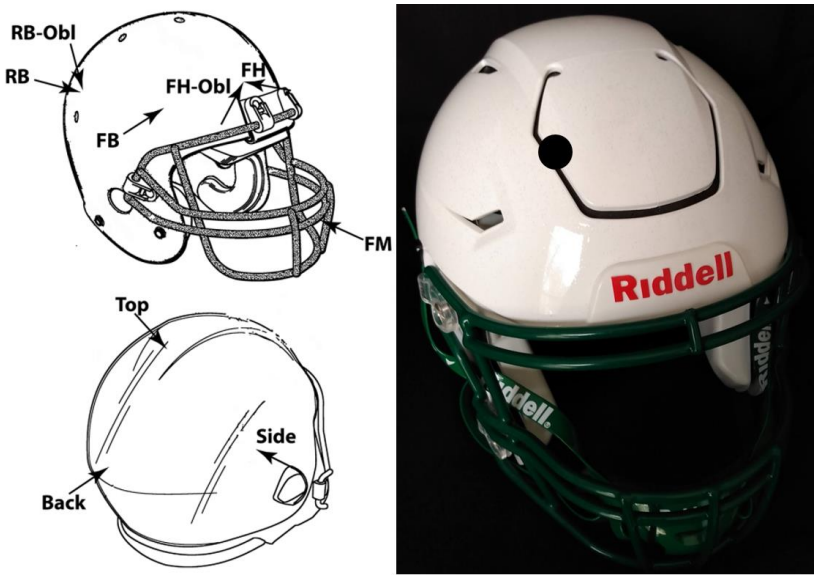

Figure 4.1 Impact locations used by Cummiskey et al. (left) [Figure from [84]] and new location, indicated by a black dot, added to test Speedflex cutout (right).

From the input of impulse and outputs peak translational acceleration (PTA) and peak rotational acceleration (PRA), dimensionless variables were defined and used to evaluate performance. From the plots of dimensionless PTA and PRA vs dimensionless impulse, a curve was fit, and outliers removed from the data as necessary [84]. Following this, the regression coefficients were evaluated between the different impact cases (experimental barehead, simulated barehead, experimental helmet a, simulated helmet b, etc.) to determine if the coefficients were statistically different.

A logical step forward for the HIRRT Lab to take was to bring helmet testing into the computational space. To that end, I calibrated and verified a digital twin to the experimental helmet testing setup and simulated a 2016 Riddell Revolution Speed Classic to compare to a 2018 Riddell Revolution Speed Classic. Helmet simulation will be an invaluable tool to research, making modifications of helmet geometry and materials feasible.

Simulations of the barehead and helmeted headforms was done using the simulation software Velodyne, a Corvid Technologies LLC product [86]. LS-PrePost, a Liverpool Software Technology pre- and post-processing software, was used to visually interact with meshed geometries [78]. Helmet parts and additional parts for the headform were created using the CAD software Solidworks, and meshed using coreform Cubit [87], [88]. The open-source visualization

software VisIt was used to visually inspect the simulations [89]. Pre- and post-processing of simulations was performed using MATLAB [77].

4.2 Methods

4.2.1 Calibration and Verification of Barehead Hybrid III Head and Neck Model

The bulk of the digital twin H3 head and neck model was made available to me during my internship at Corvid Technologies LLC, and they allowed me to return with the model to university. The part addition made to the model was the inclusion of an accelerometer mount modeled after the one designed by Cummiskey et al. and can be seen in Figure 4.2, along with comparison to the digital twin model [85]. The drawings for the accelerometer mount were used to create a simplified version of the device [85]. All holes for fittings and cutouts for holding the accelerometers were not implemented and the FE model was made to be monolithic. The elimination of the holes was done to simplify meshing and making the mount monolithic eliminated the need to define and use fasteners. The elimination of the cutouts was done because there needed to be nodes and elements in the areas of the cutouts to define the accelerometers in the model. Accelerometers were defined according to Velodyne specifications, with their locations at the approximate locations of their experimental counterparts; this minor change in accelerometer location is reflected in changes to the variables related to accelerometer position.

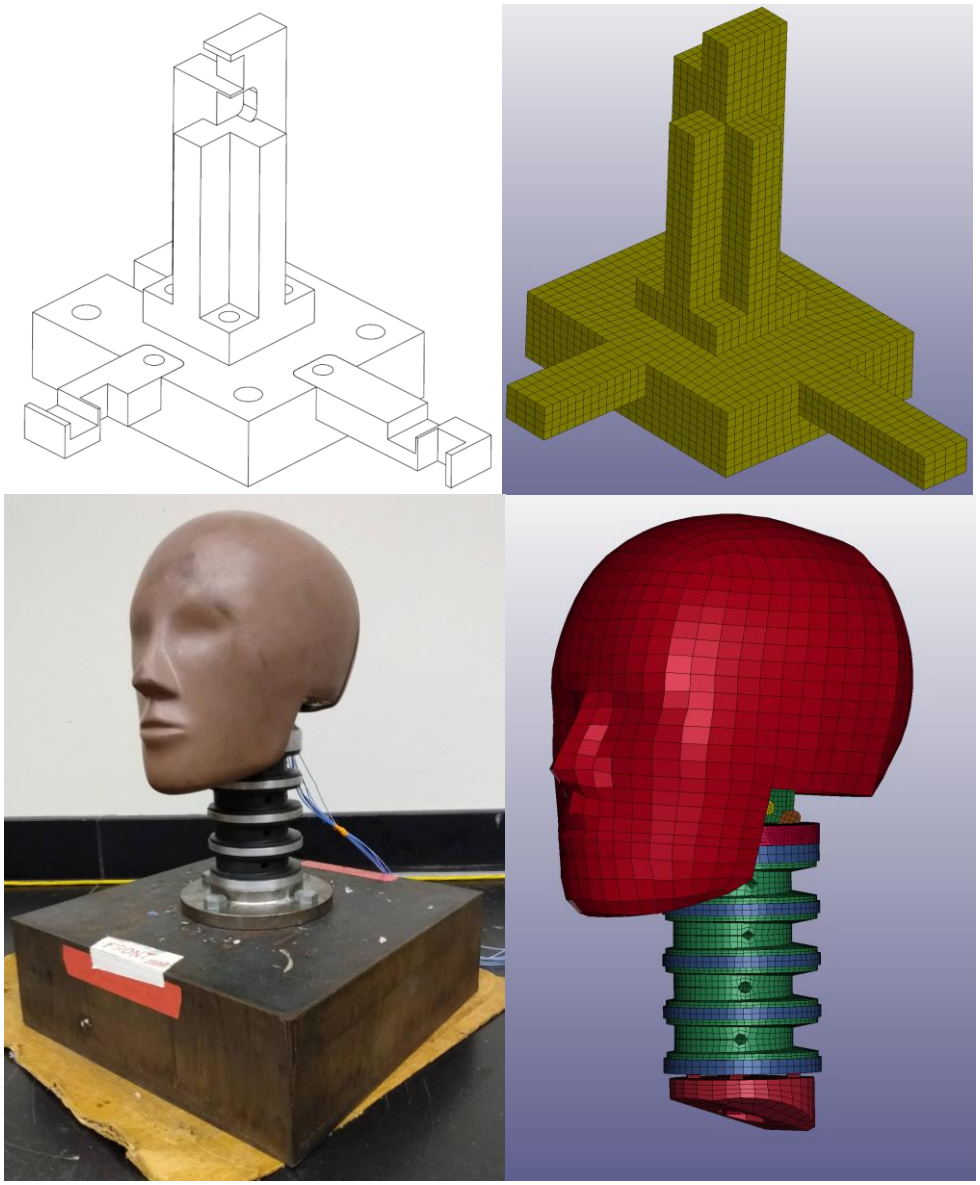

Figure 4.2 Accelerometer mount designed by Cummiskey et al. (top left) [Figure from [85]] used in the HIRRT Lab helmet testing experimental setup and the FE representation (top right) of the Cummiskey et al. accelerometer mount used in the digital twin simulations. Experimental head and neck setup (bottom left) and virtual twin setup (bottom right).

The calibration and verification of the digital twin followed a very similar method as laid out by members of the HIRRT [85], [90]. Experimental testing on the head included hits to the front, side, and rear of the head. Hits were limited to the front, side, and rear in order to simplify calibration and verification of the simulated bareheaded model but additional hits to other locations tested experimentally could be performed later to further assess the validity of the simulated

headform. The experimental setup could measure PTA and PRA using data from the custom sensor mount mounted at the center of mass of the headform and utilization of a nine accelerometer (composed of 1 triaxial and 6 uniaxial accelerometers) protocol [85]. The force profile is also recorded using a modal impact hammer. The dimensionless variables mentioned earlier are π_1, Π_1, and Π_2 and are presented in equations 4.1-4.3 for reference [84]. The components of the dimensionless variables are a reference time t_r of 100 ms and impact duration Δt, the impulse delivered by the hammer on the head $\int F(t)dt$, mass of the head m_h, width of the neck w_n, peak translational acceleration a_p, and peak rotational acceleration $\ddot{\theta}_p$ [84].

$$\pi_1 = \frac{(t_r - \Delta t)\int F(t)dt}{m_h w_n} \quad (4.1)$$

$$\Pi_1 = \frac{a_p(t_r - \Delta t)^2}{w_n} \quad (4.2)$$

$$\Pi_2 = \ddot{\theta}_p(t_r - \Delta t)^2 \quad (4.3)$$

Following the calculation of the dimensionless variables above, the Π_1 vs π_1 and Π_2 vs π_1 data points are preliminarily fit to a log transformation of an intermediate asymptotic model (Equation 4.4), the equation for which can be seen in Equation 4.4 [84]. A modified Grubb's method and estimated standard deviation were then used to remove outliers that that were more than three standard deviations from the equation for the preliminary fit. A final curve fit was then performed to determine the B_i and β_{1i} regression coefficient values for each dataset. From the final curve fit with the regression coefficients to determine the effect size between the experimental barehead model and the simulated head model. 101 evenly spaced points from 0 to the maximum values for the $\pi 1$ coefficients were used to estimate the area under the regression curve and the mean values for each location. The difference between the area under the curve of the experimental barehead and a simulated case would then be divided by the area under the experimental barehead curve. This was done for both Π_1 and Π_2 variables. In the case of comparing the experimental and simulated barehead, the closer the effect size is to zero, the closer the models are. In the case of comparing the barehead to the helmeted simulations, the higher the effect size, the impact absorption capabilities of the helmet.

$$\ln(\Pi_i) = \ln(B_i) + \beta_{1i}\ln(\pi_1) \quad (4.4)$$

These final pi plots' regression coefficients can then be statistically evaluated to determine if they are statistically significant from each other. The experimental and simulated barehead regression coefficients were compared using an analysis of covariance with an α of 0.05, with a

post hoc Tukey test with Holm-Sidak p-value correction to determine significant differences between regression coefficients of the experimental and simulated data [84].

For calibration and verification of the digital twin, hits to the front, side, and rear of the head were simulated, the locations of which can be seen in Figure 4.3. From the experimental barehead data, the force curve was extracted, subjected to the application of rejection criteria, and then transformed to be appropriate for simulation. The rejection criteria defined set limits on when the peak force could occur in the recorded 200 ms of each experimental hit. If the peak force occurred before 10 ms or after 175 ms, the data would be rejected and not used to define a simulation because outside of the 10-175 ms time window, the full curve of the impact and subsequent accelerations were not fully expressed. If an experimental hit was rejected, it would be noted in an error report file that would give the hit and the reason for rejection. If hit data was not rejected, the applied force would have its negative values set to zero. Setting the minimum force to zero was necessary because of how Velodyne applies forces. A force applied to a node set uses a curve with force plotted against time. If there were negative values in the curve, they would be explicitly applied the model during simulated impact, which is unrealistic. Additionally, the force curve would be shifted in time to begin shortly after time zero so that there would be no wasted simulation time waiting for the force to be applied. Figure 4.4 shows an experimentally recorded force curve beside its zeroed and time shifted version used for simulation. The experimental acceleration data was also subjected to the same time shifting to maintain the relationship between the applied force and the resulting acceleration and be a useful comparison to the simulated accelerations. The experimental variables π_1, Π_1, and Π_2 were also saved linked to their companion simulations for later postprocessing.

Next, files that need to be included in the simulation directory, such as the geometry, sets, and includes files defining the head and neck, would be copied from a base directory. Additionally, the preprocessing code would write a new include file that would define where the simulation would find necessary files, the node set to which the nodal force set would be applied, a mass scaling definition for the simulation, a rotation transformation for the head and neck to define the angle of impact, and the abscissa and ordinate values that define the load curve for the applied nodal force set.

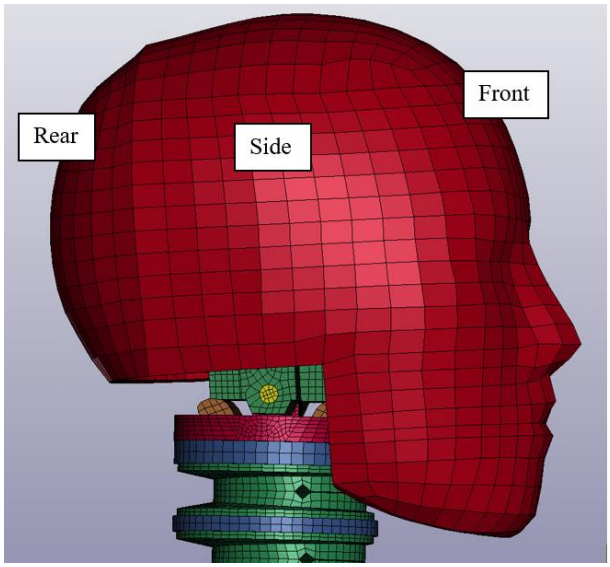

Figure 4.3 Illustration of hit locations on simulated barehead model.

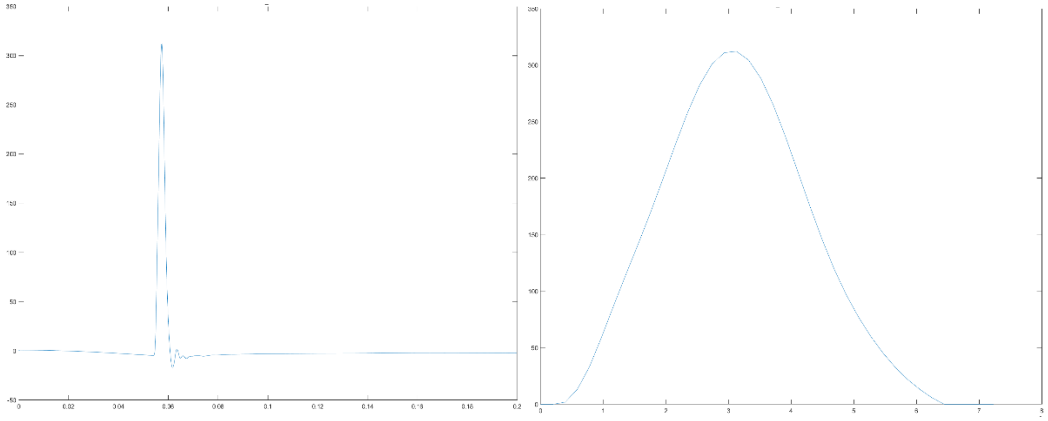

Figure 4.4 Comparison of raw experimental applied force (left) and zeroed and time shifted simulated applied force (right).

A special feature of the preprocessing code is that it is capable of spawning a theoretically limitless number of simulations, the only limit being the number of experimental datasets from which to pull data to define simulation inputs. The maximum number of jobs spawned so far by running one instance of the preprocessor code is 273. The only parameters that need to be input by the user before preprocessing is to have the correct files and directory paths defined. Following this, all jobs in a group can be submitted on a cluster using a single script.

Once all simulations of a group are complete, postprocessing using a custom MATLAB code can begin. The postprocessor goes through the simulation directories created by the pre-processor one at a time and extracts the simulated accelerometer data, calculates and saves the dimensionless variables, and plots experimental vs simulated data. The postprocessor first reads the H5 data files and extracts the accelerometer data collected during simulation. The accelerometer data (sampled at 1000 kHz) was filtered with a 5120 Hz low-pass filter (experimental sampling rate), to eliminate high frequency noise. Following this a 4th order Butterworth filter with a cutoff frequency of 600 Hz was applied, followed by downsampling the simulation accelerometer data to 5210 Hz. The PTA, PRA, π_1, Π_1, and Π_2 variables are then calculated for the simulation and saved for later use.

In early simulations, the neck of the H3H was lined up with the z axis, with impact directions being prescribed to be along the x axis for the front and back of the head, and the y axis for the side of the head. This resulted in qualitatively reasonable PTAs but unreasonable PRAs. Since the hit on the experimental setup were delivered by human hands with a hammer, the idea was had to try shifting the angles of impact for the simulation. To that end, a sweep of simulations were spawned and run with impact angles ranging from 0-45º; see Figure 4.5 for how these angles are arranged.

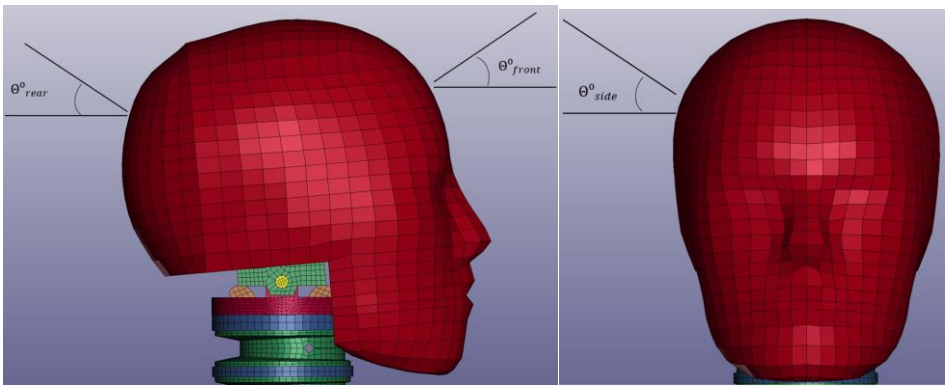

Figure 4.5 Illustration of how impact angle is defined for front, side, and rear hits.

After this preliminary angle sweep, further simulations were preformed to find the best angle of impact until the angles 30º, 28º, and 31º for the front, side, and rear hit location respectively, were determined to produce results similar to those of the experimental data.

Another issue that presented in simulating impacts to the bare head was a secondary spike in PTA in nearly all simulations. Examining the individual accelerometer traces from simulations,

the spike in PTA was found to be a result of spikes in accelerometers 3, 4, and 7, which had axes along the axis of the neck (see Figure 4.6 for accelerometers directions). Plotting the acceleration traces for these three accelerometers showed that these secondary negative peaks lined up in time. Opening the visual plot files in VisIt and going to the approximate timepoint where the peaks occurred showed the issue. By applying a Von Mises Criterion pseudocolor in VisIt and turning off the visibility of the neck adjustment bracket, the bottom part of the neck (visible in Figure 4.2), one can see that the top face of the nut that attaches to the neck cable of the H3 neck impacted the bottom surface of the neck adjustment bracket at the approximate time of the acceleration spike. See Figures 4.7 and 4.8 for the plots relevant to a representative simulation that contained the acceleration spike.

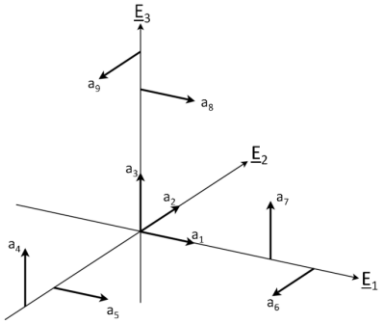

Figure 4.6 Accelerometer orientations in the accelerometer mount. E_1, E_2, and E_3 point toward the front, left side, and top of the head respectively. Figure from [85].

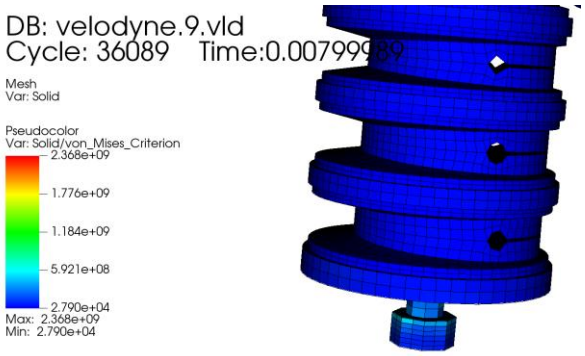

Figure 4.7 Pseudocolor plot of Von Mises Criterion of the bottom of the neck. Top elements of neck bold can be seen to have a higher value that surrounding elements.

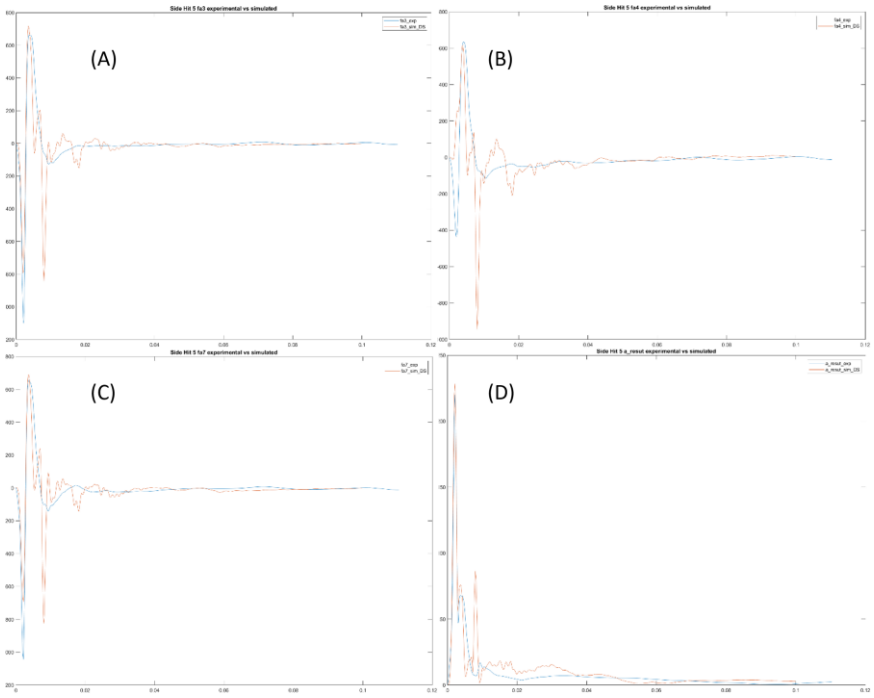

Figure 4.8 Filtered acceleration traces for accelerometers 3 (A), 4 (B), and 7 (C) and the resultant translational acceleration (D) that show the acceleration spike from neck nut impact. The negative acceleration spike at ~8 ms can be seen in A, B, and C and the resultant acceleration spike in D. Blue curves are from experimental data and orange curves are from simulation data.

In an attempt to stop the neck nut impacting the neck adjustment bracket, it was effectively unthreaded in simuilations to increase the distance between the nut and neck adjustment bracket. The nut was unthreaded to distances of 1 mm, 1.25 mm, 2.5 mm, and 5 mm from its original position. While all simulations with the nut unthreaded to various degrees lessened or eliminated the acceleration spike from the nut impacting, another issue arose. Oscillations started to occur in accelerometers 3, 4, and 7. The oscillations are most visible in the 14+ Ns impacts and can be seen in Figure 4.9 but are present in all simulations. For the simulations with the nut unthreaded 1 mm, a hybrid of acceleration spike and oscillation can be seen (Figure 4.10). It should be noted that the simulations, whose acceleration plots appear in Figures 4.8, 4.9, and 4.10 are identical except for the position of the neck nut. Additional testing with the nut being unthreaded 0.15 mm, 0.2 mm, 0.25 mm, 0.3 mm, 0.35 mm, 0.4 mm, and 0.45 mm from its original position also resulted in hybridization of the acceleration spike and oscillations.

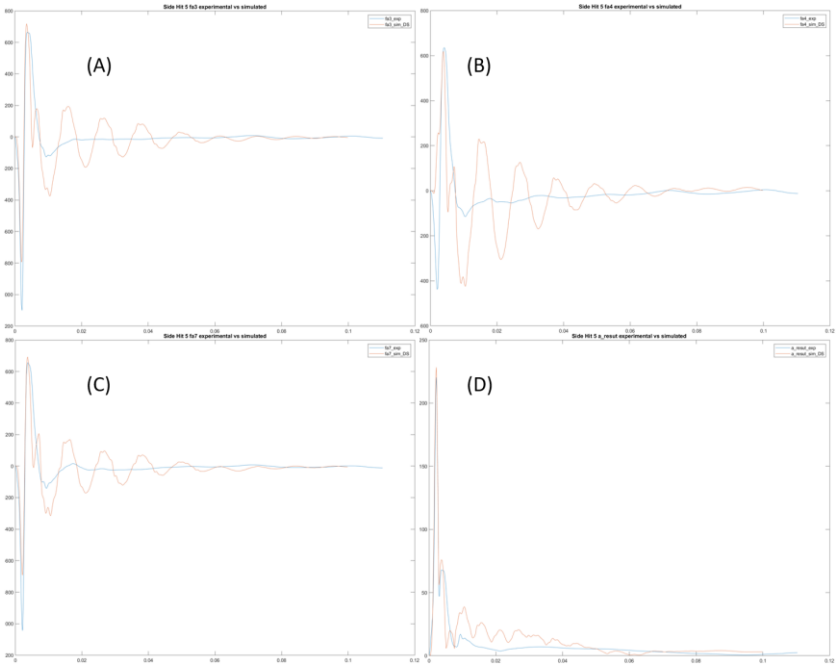

Figure 4.9 Filtered acceleration traces for accelerometers 3 (A), 4 (B), and 7 (C) and the resultant translational acceleration (D) that show the acceleration oscillation when the nut is unthreaded 5 mm. Blue curves are from experimental data and orange curves are from simulation data.

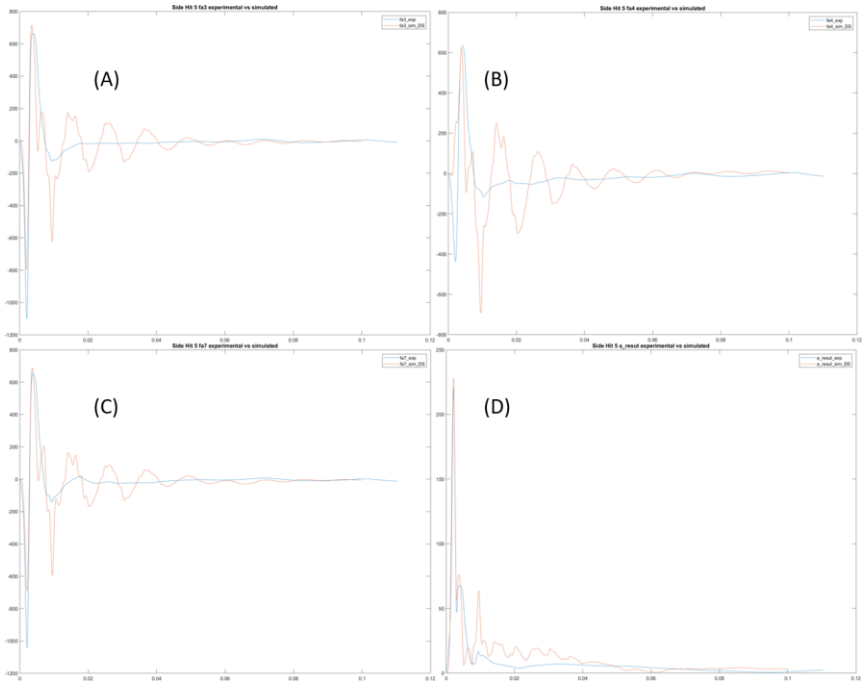

Figure 4.10 Filtered acceleration traces for accelerometers 3 (A), 4 (B), and 7 (C) and the resultant translational acceleration (D) that show the acceleration oscillation when the nut is unthreaded 1 mm. Blue curves are from experimental data and orange curves are from simulation data.

Another attempt to solve the issue of the second acceleration spike was to tie the neck nut and neck adjustment bracket together so that they remained in contact with each other throughout simulation and therefore be unable to collide with each other. This was effectively done with a tied node set between the mating surfaces of the neck nut and the neck adjustment bracket.

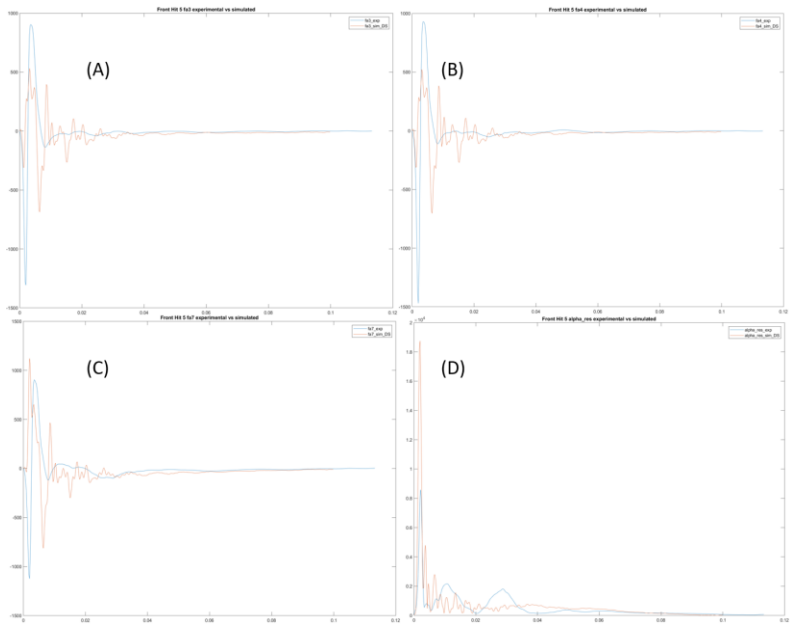

Figure 4.11 Filtered acceleration traces for accelerometers 3 (A), 4 (B), and 7 (C) and the resultant translational acceleration (D) that show the acceleration when the neck nut is tied to the neck bracket. Blue curves are from experimental data and orange curves are from simulation data.

4.2.2 2016 Riddell Revolution Speed Classic Football Helmet Simulation Setup

The football helmet simulated on the digital testing twin was the 2016 Riddell Revolution Speed Classic (RRSC). The FE model of the helmet was developed based of the geometry of the Biocore model of the RRSC designed to run in LS-DYNA. The meshed parts from the BioCore model could not be used in Velodyne due to mesh issues such as wedge elements in parts that were mostly composed of hexahedral elements necessitated a reconstruction of the helmet as Velodyne does not support wedge elements. All parts were exported individually from LS-DYNA as stl files and then opened in SolidWorks. In SolidWorks, using the points of the stl mesh as reference points, new STEP files were created, imposted into Cubit, meshed, and reassembled into a helmet in LS-PPREPOST. The LS-DYNA keyword file was used as reference to define the material models for the Fu-Chang modeled foam padding, helmet shell, chinstrap/cup, and facemask in Velodyne and the model itself was referenced when recreating tied sets between parts. The original reconstructed helmet can be seen in Figure 4.11.

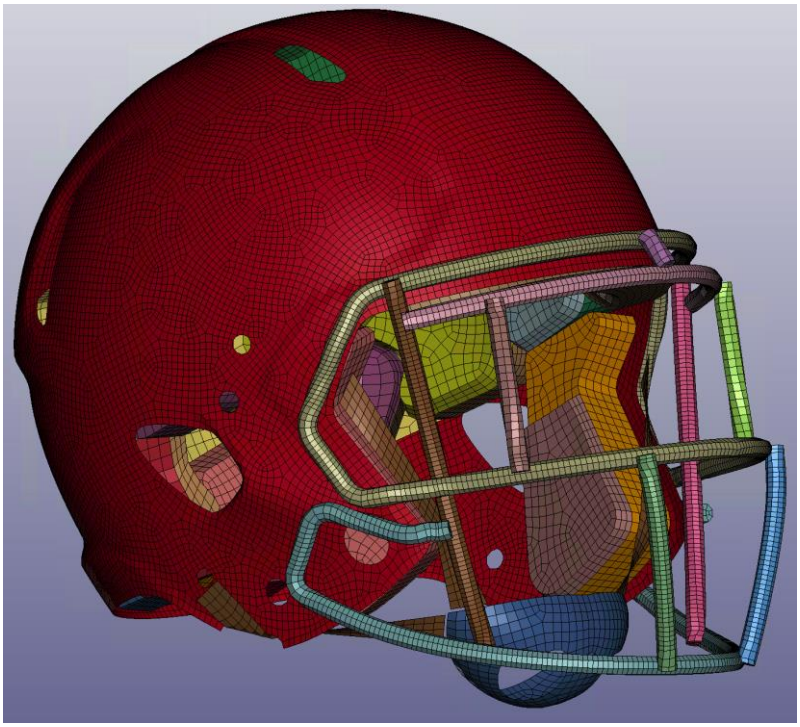

Figure 4.12 Early version of the reconstructed 2016 RRSC helmet.

A hurdle that appeared early on in testing of the helmet was the instability of the chinstrap of the helmet model during impacts. The helmet shown in Figure 4.12 would fail to run to completion due to the elements of the chinstrap becoming unstable, causing neighboring elements to invert. In addition to the chinstrap shown in Figure 4.12, other chinstrap geometries were attempted, with the other attempts as well as the final working chinstrap shown in Figure 4.13. The final chinstrap geometry used as reference a Corvid ACH simulation and the BioCore DYNA model to define the chinstrap with discrete element connecting the chinstrap to the helmet shell and beam elements connecting the chinstrap to the chincup.

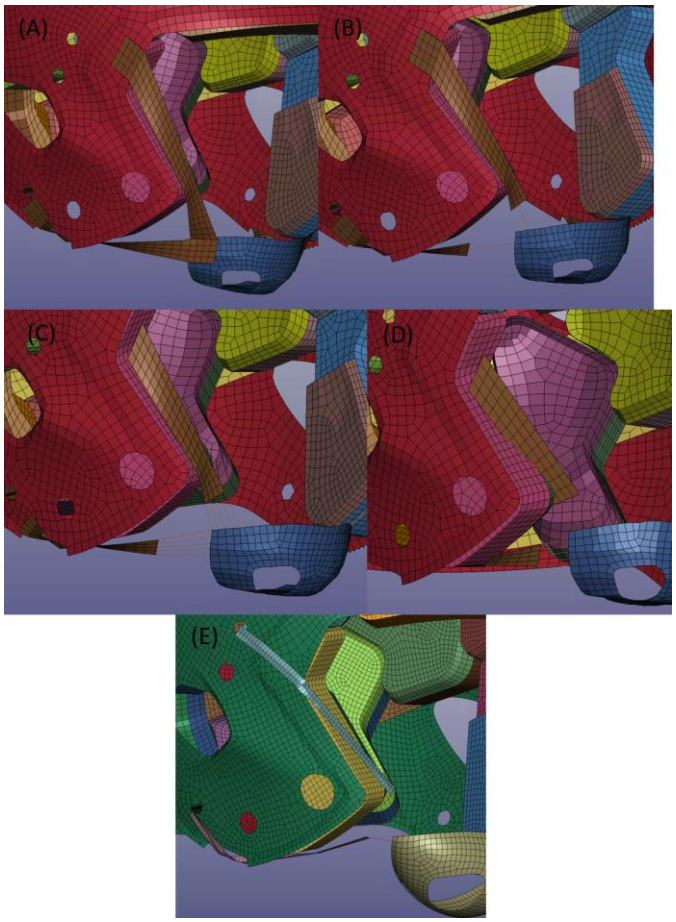

Figure 4.13 Various, failed versions of the chinstrap geometry A-C, alongside the final, functional chinstrap geometry D, with BioCore chinstrap geometry visible in E.

With the chinstrap sorted, and no longer being the impetus behind simulations crashing, impact simulations of a helmeted headform could begin. When running a group of simulations, an issue that occurred in some 14+ Ns simulations was compression of the comfort padding that lay between the energy absorbing padding and the head. This comfort padding would compress so much that the volume of elements would drastically shrink, causing the timestep of the simulation to become incredibly small, resulting in the termination of the Velodyne simulation. To address this, the material definitions associated with the comfort padding geometry was switched to that of the energy absorbing padding beneath. Figure 4.14 shows how the padding differs between the BioCore model run in DYNA and the model run in Velodyne. After changing the material definitions associated with the comfort padding, the simulations in the 14+ Ns range began running to completion.

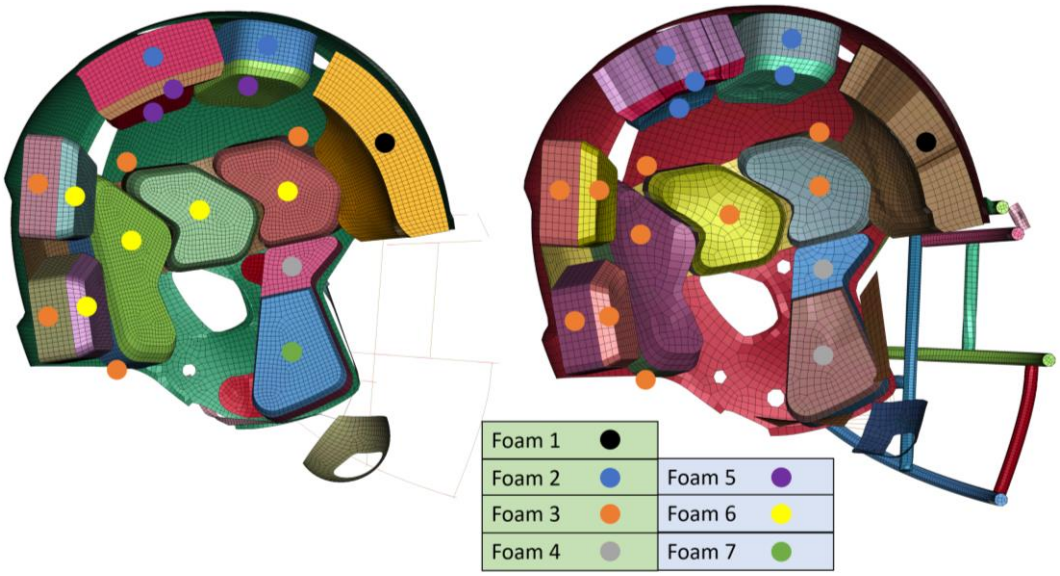

Figure 4.14 Padding comparison between BioCore's (left) and Velodyne simulated (right) models. Foams in the green section of the legend are energy absorption foams while foams in the blue section are comfort foams.

Next, simulations were spawned using experimental data, with hits falling into the same impulse ranges mentioned in the barehead simulation methods. Following completion of the simulations, postprocessing to determine the pi variables and pi plots takes place in the same fashion as described in the barehead simulation methods. These helmeted simulation pi plots and their regression coefficients were then compared to the barehead data, using the same statistics gone over earlier to determine if there are statistically significant differences.

Preliminary simulations of the helmeted head showed a stark contrast between experimental and simulated helmet performance, with experimental helmeted pi plots having greater slopes than simulated helmets. In an attempt to alleviate this discrepancy, the scale factor that scales the stress data defined in the Fu-Chang tables was lowered to various degrees in an attempt to make the padding softer. Table 4-1 shows how the scale factors were modified from the original. Foams 1, 2, 3, and 4 had the same scaling factors, with 1 Fu-Chang table applied to Foam 1 and 1 Fu-Chang table applied to Foams 2, 3, and 4.

Table 4-1 Original scale factor and modified scale factors used in RRSC helmet simulations. Scale factor a is 1 order of magnitude lower than the original, scale factor b is the mean of the original scale factor and scale factor a, scale factor e is the average of the original and scale factor d, and scale factor f is the average of scale factors a and d.

Original Scale Factor	Scale Factor a	Scale Factor d	Scale Factor e	Scale Factor f
1.00E+07	1.00E+06	5.50E+06	7.75E+06	3.25E+06

4.3 Results

4.3.1 Results from barehead H3H simulations

Translational and rotational acceleration plots for the same hit, differing only in the angle of impact can be seen in Figure 4.15. Translational acceleration can be seen to be qualitatively similar across the hit angles, but rotational acceleration can differ greatly. The pi plots for the calibration of front, side, and rear impacts can be seen in Figure 4.16, while the pi plots for the verification can be seen in Figure 4.17.

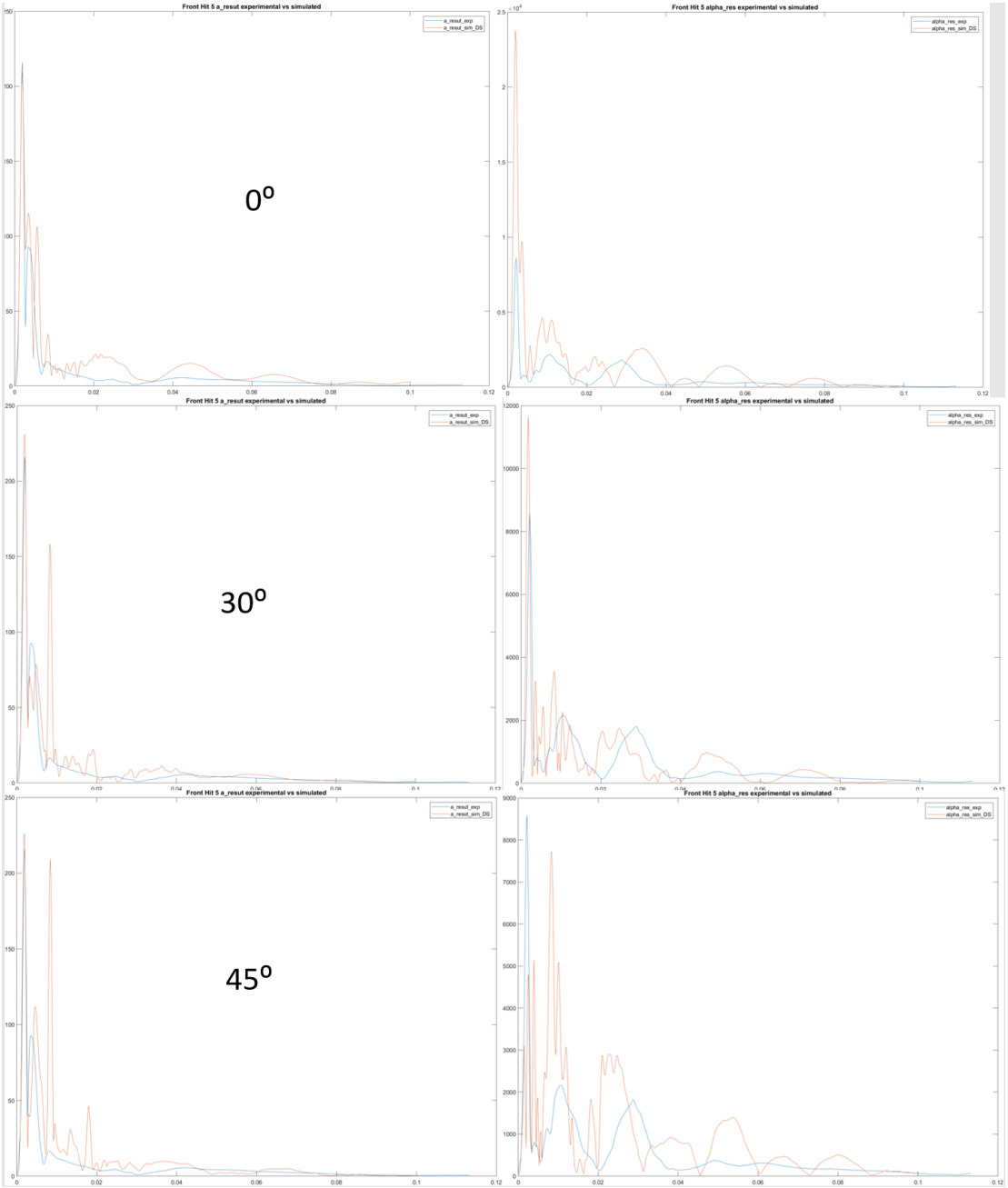

Figure 4.15 Translational acceleration (left column) and rotational acceleration (right column) plots for front hits to the barehead that differ only in angle of impact.

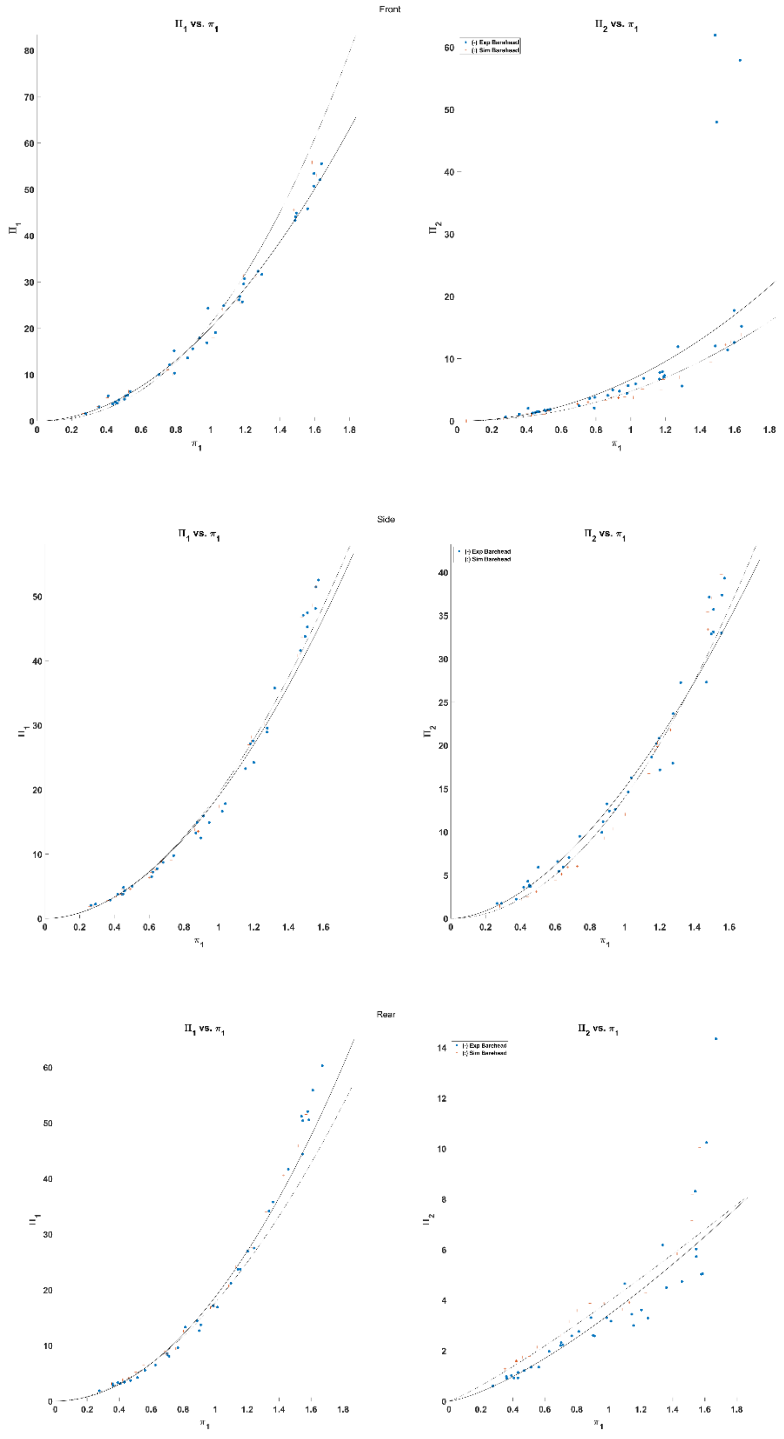

Figure 4.16 Pi plots from the calibration simulations.

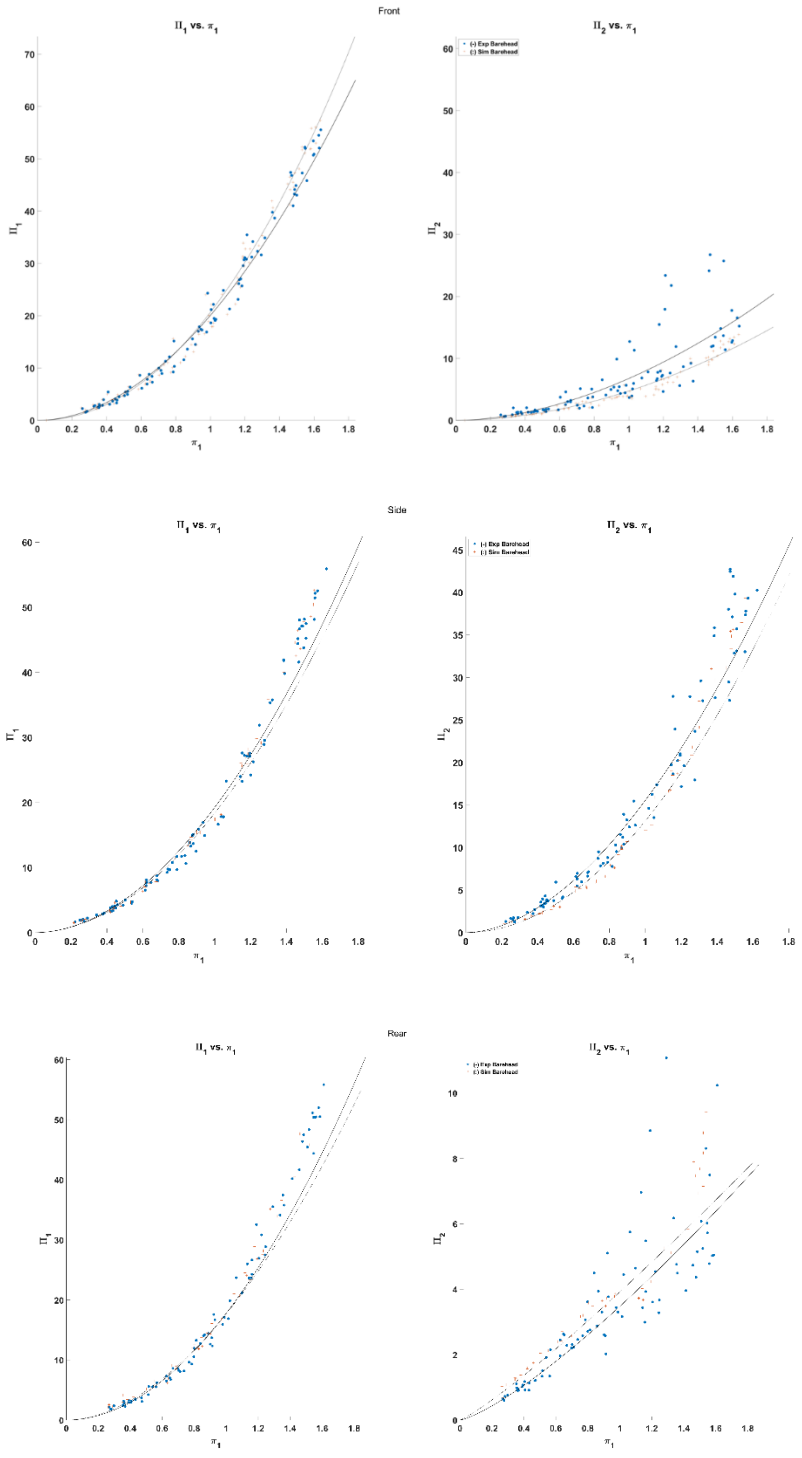

Figure 4.17 Pi plots from the verification of the barehead simulations.

Table 4-2 lays out the regression coefficients for the dimensionless PTA variable, Π_1, for the experimental and barehead hits from the verification of the simulated headform, as well as the

ANCOVA results. The letters in parentheses indicate that a significant difference between groups a and b, corresponding to experimental barehead and simulated barehead.

Table 4-2 Regression coefficients of the curves fit to the dimensionless PTA variable Π_1 for bareheaded cases, along with ANCOVA ($p<0.05$) results indicated in parentheses.

		Hit Location		
		Front	**Side**	**Rear**
Experimental Barehead Hybrid III	B1	20.06 (b)	19.43	19.27
	β1i	1.93 (b)	1.93	1.98
Simulated Barehead Hybrid III	B1	20.80 (a)	19.64	19.90
	β1i	2.19 (a)	1.94	1.90

Table 4-3 gives the effect size of the experimental barehead data compared to the simulated barehead data for the PTA variable Π_1 for the front, back, and rear impact locations.

Table 4-3 Effect size for the simulated barehead compared to the experimental barehead for dimensionless PTA variable Π_1.

Hit Location	Simulated Barehead
Front	-8%
Side	-1%
Rear	-2%

The ANCOVA and effect size results for the Π_2 data can be seen in Tables 4-4 and 4-5. The letters in parentheses indicate that a significant difference between groups a and b, corresponding to experimental barehead and simulated barehead.

Table 4-4 Regression coefficients of the curves fit to the dimensionless PRA variable Π_2 for bareheaded cases, along with ANCOVA ($p<0.05$) results indicated in parentheses.

		Hit Location		
		Front	**Side**	**Rear**
Experimental barehead Hybrid III	B2	6.87	15.75 (b)	3.85 (b)
	β2i	1.84	1.85 (b)	1.38 (b)
Simulated Barehead Hybrid III	B2	4.77	14.11 (a)	4.35 (a)
	β2i	1.97	2.01 (a)	1.23 (a)

Table 4-5 Effect size for the simulated barehead compared to the experimental barehead for dimensionless PRA variable Π_2.

Hit Location	**Simulated Barehead Hybrid III**
Front	29%
Side	8%
Rear	-12%

4.3.2 Helmeted Simulation Results

Initial simulations of the helmet were underwhelming and unstable. Simulations continued to crash, with the elements of the chinstrap becoming unstable, leading to negative element volumes and termination of the simulation. Numerous methods to solve the instability problems of the chinstrap were attempted until a solution was reached. Connecting the chinstrap to the helmet with discrete elements and to the chincup with beam elements solved the instability of the chinstrap.

Figure 4.18 show linear and rotational acceleration results from preliminary simulations for front impacts to the helmeted head model at the same 30º angle as the bareheaded impacts. The simulation PTAs can be seen to be nearly 50% higher than the experimental values, while the simulations PRAs can be seen to be several times larger the experimental value.

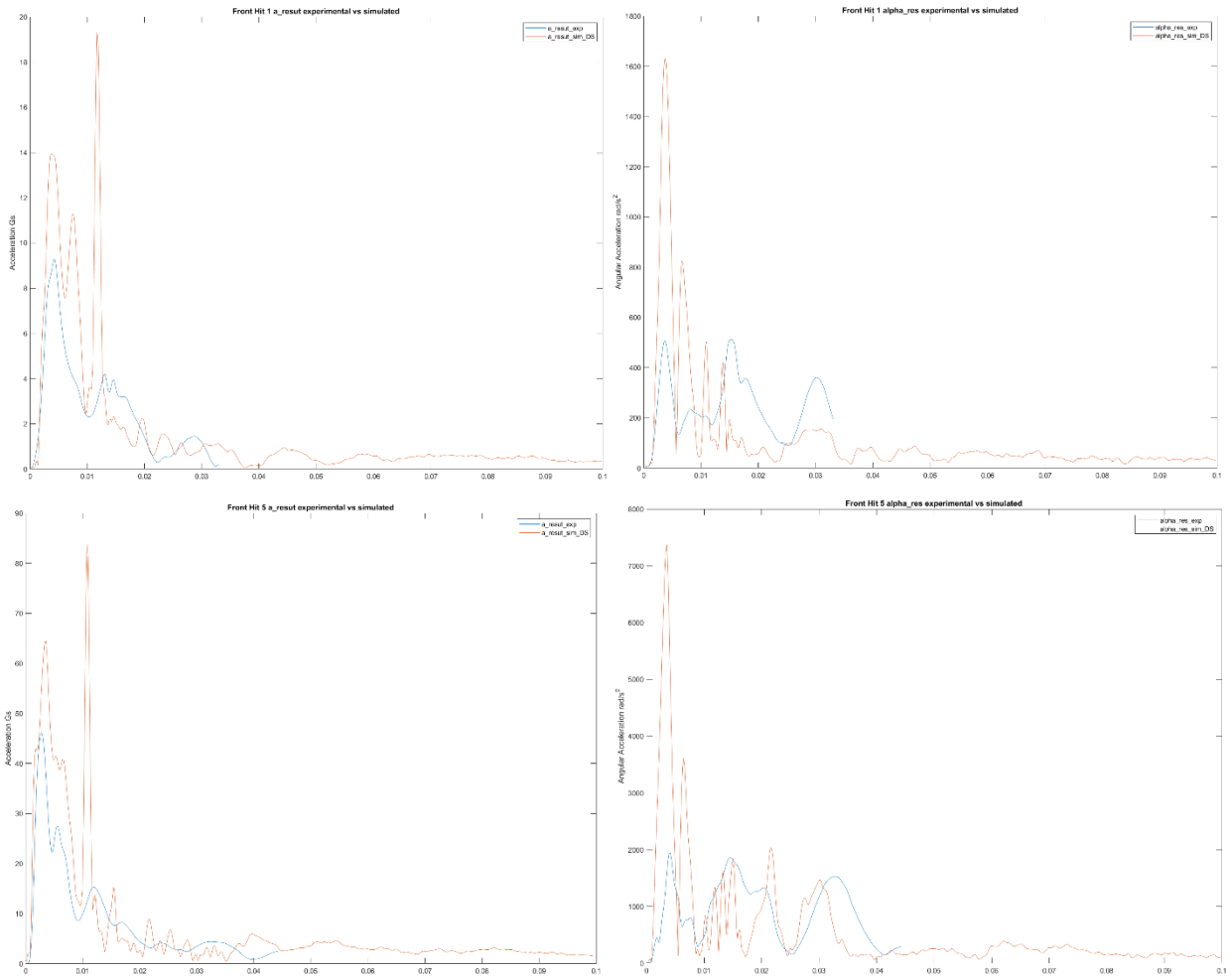

Figure 4.18 Preliminary linear and angular acceleration for front impacts.

Figures 4.19 shows the dimensionless PTA and PRA plotted against dimensionless impulse for the front and side impact locations for bareheaded and helmeted cases. The plots for the dimensionless PTA and PRA for rear impacts are not shown as they are currently unreasonable and unrealistic.

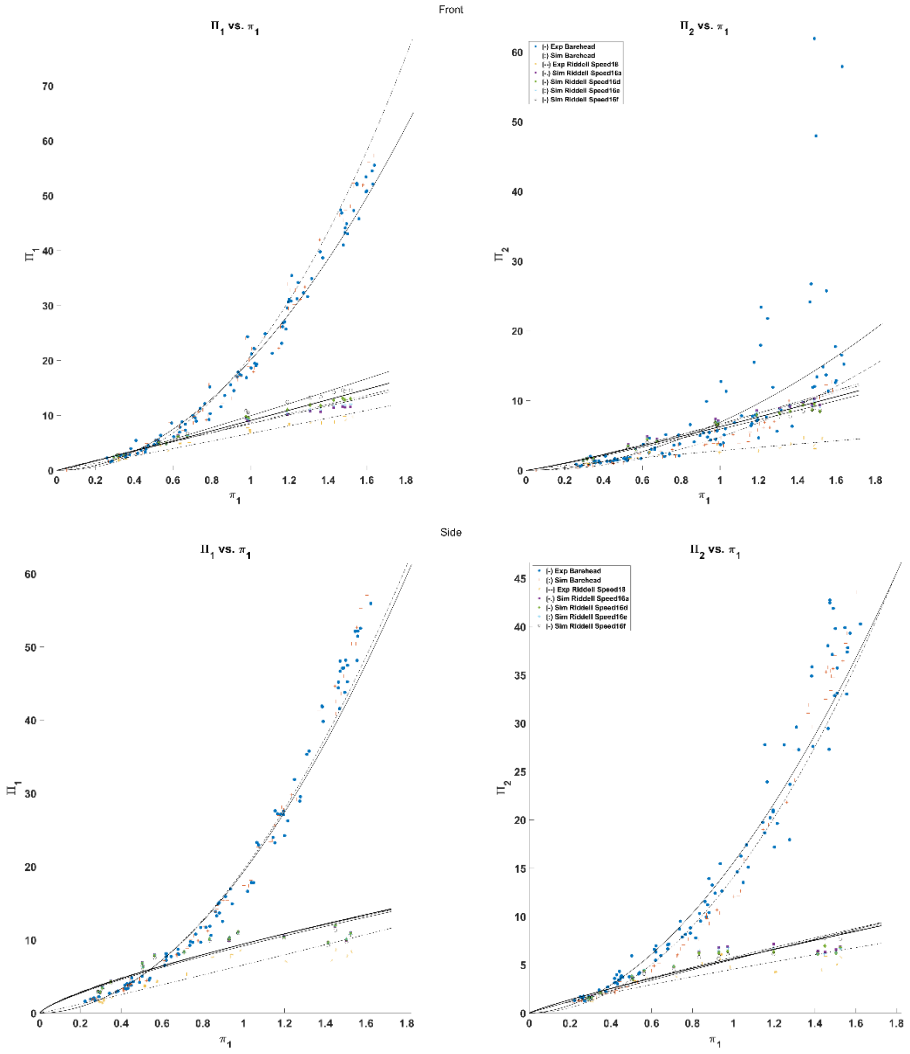

Figure 4.19 Pi plots inclusive of data from the experimental and simulated barehead and simulated helmeted impacts for the front and side impact locations.

Table 4-6 gives the regression coefficients and ANCOVA results for comparing the Π_1 data from the bareheaded impact cases and the simulated helmeted impact cases. The letter(s) in parentheses indicates a significant difference between the given regression coefficient and the regression coefficient indicated by the letter. Letters a, b, c, d, e, f, and g correspond to the experimental H3 head, simulated H3 head, experimental 2018 Riddell Speed, simulated 2016 RRSC a (original scale factor), simulated 2016 RRSC d, simulated 2016 RRSR e, and simulated 2016 RRSC f.

Table 4-6 Regression coefficients of the curves fit to the dimensionless PTA variable Π_1 for bareheaded and helmeted cases, along with ANCOVA ($p<0.05$) results indicated in parentheses.

		Hit Location		
		Front	**Side**	**Rear***
Experimental barehead Hybrid III	B1	20.06 (bcdefg)	19.43 (cdefg)	19.27 (bcdefg)
	β1i	1.93 (bcdefg)	1.93 (cdefg)	1.98 (cdefg)
Simulated Barehead Hybrid III	B1	20.80 (acdefg)	19.64 (cdefg)	19.90 (acdefg)
	β1i	2.19 (acdefg)	1.94 (cdefg)	1.90 (cdefg)
Experimental Riddell Speed 2018	B1	6.72 (abdefg)	6.58 (abdefg)	6.48 (abdefg)
	β1i	1.03 (ab)	1.04 (abdefg)	0.92 (ab)
Simulated Riddell Speed 2016 a	B1	8.48 (abceg)	9.43 (abcg)	13.43 (abceg)
	β1i	0.96 (abg)	0.74 (abc)	0.88 (ab)
Simulated Riddell Speed 2016 b	B1	9.07 (abcdfg)	9.44 (abcg)	12.51 (abcdfg)
	β1i	1.04 (ab)	0.75 (abc)	0.91 (ab)
Simulated Riddell Speed 2016 c	B1	8.63 (abceg)	9.44 (abcg)	13.24 (abceg)
	β1i	0.98 (abg)	0.74 (abc)	0.89 (ab)
Simulated Riddell Speed 2016 d	B1	9.94 (abcdef)	9.18 (abcdef)	10.63 (abcdef)
	β1i	1.10 (abdf)	0.76 (abc)	0.94 (ab)

Table 4-7 gives the effect size for comparing the simulated impact cases' data and the experimental Riddell Speed 2018 data to the experimental barehead for Π_1. For the simulated barehead, the lower the number, better it corresponds to the experimental barehead. In the case of a negative value, this indicates that the barehead overestimates the translational acceleration response. For the helmeted cases, the higher the value, the better the impact was absorbed by the helmet.

Table 4-7 Effect size for the simulated barehead compared to the experimental barehead for dimensionless PTA variable Π_1.

Hit Location	Simulated Barehead Hybrid III	Experimental Riddell Speed 2018	Simulated Riddell Speed 2016 a	Simulated Riddell Speed 2016 b	Simulated Riddell Speed 2016 c	Simulated Riddell Speed 2016 d
Front	-8%	67%	58%	55%	57%	51%
Side	-1%	67%	51%	51%	51%	52%
Rear*	-2%	67%	30%	35%	31%	45%

Table 4-8 presents the regression coefficients and ANCOVA results for comparing the Π_2 data from the bareheaded impact cases and the simulated helmeted impact cases. The letter(s) in parentheses indicates a significant difference between the given regression coefficient and the regression coefficient indicated by the letter. Letters a, b, c, d, e, f, and g correspond to the experimental H3 head, simulated H3 head, experimental 2018 Riddell Speed, simulated 2016 RRSC a (original scale factor), simulated 2016 RRSC d, simulated 2016 RRSR e, and simulated 2016 RRSC f.

Table 4-8 Regression coefficients of the curves fit to the dimensionless PRA variable Π_2 for bareheaded and helmeted cases, along with ANCOVA ($p<0.05$) results indicated in parentheses.

		Hit Location		
		Front	**Side**	**Rear***
Experimental barehead Hybrid III	B1	6.87 (bcg)	15.75 (bcdefg)	3.85 (bcdefg)
	β1i	1.84 (cdefg)	1.85 (bcdefg)	1.38 (bdefg)
Simulated Barehead Hybrid III	B1	4.77 (acdefg)	14.11 (acdefg)	4.35 (acdefg)
	β1i	1.97 (cdefg)	2.01 (acdefg)	1.23 (adefg)
Experimental Riddell Speed 2018	B1	2.82 (abdefg)	4.55 (abdefg)	2.92 (abdefg)
	β1i	0.87 (abdefg)	0.85 (ab)	1.30 (defg)
Simulated Riddell Speed 2016 a	B1	6.66 (bceg)	5.78 (abcefg)	7.31 (abcefg)
	β1i	1.16 (abc)	0.89 (ab)	0.97 (abc)
Simulated Riddell Speed 2016 d	B1	6.25 (bcdfg)	5.62 (abcd)	5.29 (abcdfg)
	β1i	1.12 (abc)	0.87 (ab)	1.02 (abc)
Simulated Riddell Speed 2016 e	B1	6.55 (bceg)	5.67 (abcdg)	6.54 (abcdeg)
	β1i	1.14 (abc)	0.87 (ab)	1.02 (abc)
Simulated Riddell Speed 2016 f	B1	5.89 (abcdef)	5.55 (abcdf)	3.18 (abcdef)
	β1i	1.12 (abc)	0.95 (ab)	0.85 (abc)

Table 4-9 presents the effect size for comparing the simulated impact cases' data and the experimental Riddell Speed 2018 data to the experimental barehead for Π_2. For the simulated barehead, the lower the number, better it corresponds to the experimental barehead. For the helmeted cases, the higher the value, the better the impact was absorbed by the helmet.

Table 4-9 Effect size for the simulated barehead compared to the experimental barehead for dimensionless PRA variable Π_2.

Hit Location	Simulated Barehead Hybrid III	Experimental Riddell Speed 2018	Simulated Riddell Speed 2016 a	Simulated Riddell Speed 2016 b	Simulated Riddell Speed 2016 c	Simulated Riddell Speed 2016 d
Front	29%	59%	4%	10%	5%	15%
Side	8%	71%	63%	64%	64%	65%
Rear*	-12%	24%	-94%	-40%	-72%	15%

4.4 Discussion

4.4.1 Barehead Simulation

After the sweep to find a set of optimal angles at which the hit the front, side and rear of the head and comparing against two of the seven datasets to calibrate impact responses that agree with the experimental data, verification of the bareheaded model proceeded. The same angle determined from the calibration step were applied to the five unused datasets for verification. The second acceleration spike, caused by the collision of the neck cable nut and the neck adjustment bracket, was still visible in most resultant linear acceleration traces and in the accelerometer channels 3, 4, and 7 could not be eliminated. The methods to reduce the acceleration spike by the unthreading the nut or tying the nut to the bracket were not fruitful and modifying the material definition for butyl rubber, of which the Hybrid III neck rubber is composed, was not considered feasible. The design and validation of the simulated model and its constituent material models was performed years prior to use in the helmet testing digital twin. There is no way to determine the differences between the rubber tested and characterized for the Corvid Hybrid III model and the rubber of the HIRRT Lab experimental Hybrid III head and neck. It would be possible to characterize the neck rubber of the experimental HIRRT Lab setup by taking a sample of the neck rubber, but the testing parameters of the rubber for the Corvid model are not known and the condition of the rubber relative to the HIRRT Lab neck rubber is not known. Since the experimental and simulated traces for acceleration had comparable magnitude and shape, the neck rubber material model was left as is and the second acceleration spike accounted for in postprocessing.

Following a correction to the statistics code that generated the ANCOVA results, the relationship between the experimental head and neck and the simulated head and neck changed in that there were significant differences between the front and rear for the dimensionless PTA variable Π_1 performance and differences between the front, side, and rear for the dimensionless PRA variable Π_2 performance. Given how qualitatively similar the experimental and simulated curves are, and how important impact angle is to rotational acceleration, further simulation and refinement of the angle of impact for the front, side, and rear would likely bring the experimental and simulated barehead performance back to being statistically insignificant.

The vast difference in PRA for impacts delivered at different angles highlights a shortcoming of current helmet testing. Impacts to the same location at different angles produce similar PTA, but PRA can change dramatically. Future testing may consider the addition of different angle of impact for the same hit location to achieve a broader and more complete picture of the performance headgear.

4.4.2 **Helmeted Simulation**

With the inability of the BioCore 2016 Riddell Speed helmet model to run in Velodyne due to unsupported elements, reconstruction of the meshed geometry and application of the BioCore material definitions to the Velodyne model was the best choice available. The reconstructed model would run to completion in Velodyne, but the material definitions applied to the comfort pads proved unstable in the setup of the simulations and were changed to the energy absorption padding beneath. Different boundary conditions between the head and helmet may resolve the issue of the comfort padding being nearly completely compressed, but further simulation would be necessary to determine this.

The material definition of the foam padding of the helmet, which utilized a Fu-Chang Foam material model, may benefit from further validation and fleshing out using experimental data. From the seven foams used in the BioCore RRSC model, only 3 tables were used to define the stress and strain relationships as different strain rates. One of these tables were associated with the comfort padding layer, and were not used in the Velodyne simulations. Having additional tables with further fleshed out stain rates may contribute to different performance of the padding during simulation.

Rear helmeted impacts behaved poorly and were not featured prominently in this document. The rear pi plots can be seen in Appendix C and were not included in the main body of the document due to their behavior. Some regressions for the Π_2 variable had slopes greater than that of the unhelmeted cases, seemingly indicating inferior performance under angular acceleration than the bareheaded model. Such a result seems unlikely and warrants further simulation and research.

When reading the manual for BioCore's 2016 Riddell Revolution Speed Classic, a worrisome fact becomes clear. The evaluation criteria of the helmet model are lacking. Pendulum, linear, and drop impact data were used to validate the simulated model, but an important evaluation criterion is missing. There is no validation of the model using the angular acceleration criterion; there is however the validation criterion of angular velocity [91]. This calls into question the validity of any resulting information gleaned from angular acceleration in the simulations.

The experimental 2018 Riddell Speed results were significantly different from the 2016 Riddell Speed helmet simulations. Since the geometries of the two helmets are not strikingly distinct, the materials used in their construction are a suspect for the difference in performance. The materials of the 2018 Riddell Speed would need to be characterized, particularly the padding, to see the difference in materials.

5. CONCLUSIONS

No literature could be found where scaling was performed after repositioning of a HBM, and with the scaled CAVEMAN HBMs meeting target statures and weights, scaling code could be dubbed a success. This does not mean that this should be the conclusion to work on the scaling of the CAVEMAN model.

Given that the main target parameters for scaling are stature and weight, other anthropometric measure may possibly not be met. This makes the 5^{th} to 95^{th} scaled models a powerful tool for assessing injury for a non-average human, but it's performance may fall short if the model does not meet the specific anthropometric measurements of 1 particular individual.

Further work that could be done to increase the predictive ability of a scaled model would be to implement code that is able to change the girth of the scaling sections. Such a modification would be able to create a leaner or bulkier HBM at a given stature percentile. A possible method to accomplish this would be to radially scale the scaling sections about their constituent scaling vectors. It is also possible that Kriging or Radial Basis Function Interpolation could be employed to elicit this effect.

An even further step than creating general models outside the 50^{th} percentile would be to scale the CAVEMAN to an individual target. This has already been accomplished by other authors on other HBM models and the techniques employed there could likely be applied to CAVEMAN. On an infrequent, individual basis it may be worth to use the PIPER software framework to achieve individual scaling.

Further work to be done to validate the simulated barehead would be to have impacts that vary slightly from the angle that best reflects the results from experimental testing. This would allow for some variance to the data that is likely to exist in experimental testing. Following this, a wide swath of impacts at various angles could be run to develop and understanding of how impact angle affects translational and rotational acceleration.

Not unexpectedly, further work can be done to more accurately simulate helmets on an instrumented headform. Validation of the BioCore model using angular acceleration data would be advisable. Additionally, development of a different material model to describe foam could be a boon to helmet simulation as the angular acceleration behavior of the helmeted simulation could

be attributed to the poor performance of the foam model, but further research would need to be performed to determine this.

Additional work can also be done to examine and develop simulated helmets that perform better within a specific range of impacts. Designing a helmet to perform better for the impacts a specific position will encounter is more feasible in a simulation than experimentally. A simulation could have something as simple as the padding material replaced, or the geometry of the shell modified, the latter of which would be impractical to do experimentally, given that many helmet shell are formed through injection molding. Helmet simulations could also be used to develop and test structures added to the helmet in order to reduce angular acceleration. Such a structure could be similar in concept to the Multi-Directional Impact Protection System (MIPS) seen in bicycle helmets, but applied to football helmets. The MIPS system employs a layer between the cradle that is in contact with the head and the helmets shell, to allow for the helmet shell to rotate on the head to attenuate rotational acceleration.

HBM scaling and helmet simulation also provides the opportunity to simulate full body impacts between football plays of different statures and weights, and could give an insight into the magnitude of acceleration during big impacts.

Testing the other BioCore helmet models in simulation would also be worthwhile, as they use different padding schemes than the Riddell helmet. A prime contender for the helmet to simulate after the Riddell would be the Schutt. This is due to the Schutt helmet having conical energy absorbers as opposed to conventional foam padding, which is difficult to simulate. Helmet testing standards are also in need of update. With the NOCSAE standard testing for football helmets is not useful for comparing helmet performance and fails to take angular acceleration performance into account during testing. Testing akin to what the HIRRT Lab performs would be useful for comparing the performance of helmets.

There is always more to simulate, and with the progression of computing technology, simulation will continue to be attractive for human injury and helmet simulation. It allows precise control and analysis capabilities that are incomparable to cadaveric or dummy tests, and make the evaluation, modification, and creation of helmet technology squarely into the purview of independent researchers.

REFERENCES

[1] C. C. Gordon *et al.*, "2010 Anthropometric Survey of U.S. Marine Corps Personnel: Methods and Summary Statistics," *Journal of Biomedical Engineering*, Jun. 2013.

[2] J. S. Simpson, "An economical approach to teaching cadaver anatomy: A 10-year retrospective," *American Biology Teacher*, vol. 76, no. 1, pp. 42–46, Jan. 2014, doi: 10.1525/abt.2014.76.1.9.

[3] C. Keyes, "Steep cost of military vehicles outlined in Army report," Jan. 27, 2011. http://www.cnn.com/2011/US/01/27/army.vehicle.costs/index.html (accessed Apr. 04, 2022).

[4] A. Lawrence, "There's More to Crash Test Dummies Than Meets the Eye," Aug. 01, 2019. https://www.caranddriver.com/features/a28510766/crash-test-dummies-how-they-work/ (accessed Apr. 05, 2022).

[5] T. E. Lobdell, C. K. Kroelll, D. C. Schneider, W. E. Hering, and A. M. Nahum, "Impact Response of the Human Thorax," in *Human Impact Response: Measurement and Simulation*, Springer Science+Business Media, 1973, pp. 201–246.

[6] M. Iwamoto, K. Miki, and K. H. Yang, "Development of a Finite Element Model of the Human Shoulder to Investigate the Mechanical Responses and Injuries in Side Impact," *JSME International Journal*, vol. 44, pp. 1072–1081, 2001.

[7] P. J. Schuster, C. C. Chou, P. Prasad, and G. Jayaraman, "Development and Validation of a Pedestrian Lower Limb Non-Linear 3-D Finite Element Model," *Stapp Car Crash Journal*, vol. 44, 2000.

[8] M. Beaugonin, E. Haug, and D. Cesari, "Improvement of Numerical Ankle/Foot Model: Modeling of Deformable," *JOURNAL OF PASSENGER CARS: Part*, vol. 106, pp. 3742–3754, 1997.

[9] F. Dauvilliers, F. Bendjellal, M. Weiss, F. Lavaste, and C. Tarrière, "Development of a Finite Element Model of the Neck," *JOURNAL OF PASSENGER CARS*, vol. 103, pp. 1645–1659, 1994.

[10] G. R. Plank, M. Kleinberger, and R. H. Eppinger, "Analytical Investigation of Driver Thoracic Response to Out of Position Airbag Deployment," *JOURNAL OF PASSENGER CARS*, vol. 107, pp. 2941–2954, 1998, [Online]. Available: https://about.jstor.org/terms

[11] L. van Rooij, ; Bours, R. ;J van Hoof, and ; Mihm, “The Development, Validation and Application of a Finite Element Upper Extremeity Model Subjected to Air Bag Loading,” *Stapp Car Crash Journal*, vol. 47, pp. 55–78, 2003.

[12] Y. Huang, A. I. King, and J. M. Cavanaugh, “Finite Element Modeling of Gross Motion of Human Cadavers in Side Impact,” 1994.

[13] R. Happee, M. Hoofman, A. J. van den Kroonenberg, and P. Morsink, “A Mathematical Human Body Model for Frontal and Rearward Seated Automotive Impact Loading,” *JOURNAL OF PASSENGER CARS*, vol. 107, pp. 2720–2734, 1998, [Online]. Available: https://about.jstor.org/terms

[14] E. Lizee *et al.*, “Development of a 3D Finite Element Model of the Human Body Development of a 3D Finite Element Model of Human Body,” 1998.

[15] T. Motor Corporation, “TOTAL HUMAN MODEL FOR SAFETY (THUMS): REVOLUTIONIZING CRASH SIMULATION TO SUPPORT SAFE MOBILITY FOR ALL.” Jan. 28, 2021.

[16] M. Iwamoto, Y. Kisanuki, I. Watanabe, K. Furusu, K. Miki, and J. Hasegawa, “DEVELOPMENT OF A FINITE ELEMENT MODEL OF THE TOTAL HUMAN MODEL FOR SAFETY (THUMS) AND APPLICATION TO INJURY RECONSTRUCTION.”

[17] T. Maeno and J. Hasegawa, “DEVELOPMENT OF A FINITE ELEMENT MODEL OF THE TOTAL HUMAN MODEL FOR SAFETY (THUMS) AND APPLICATION TO CAR-PEDESTRIAN IMPACTS.”

[18] E. Lizee *et al.*, “Development of a 3D Finite Element Model of the Human Body,” *JOURNAL OF PASSENGER CARS*, vol. 107, pp. 2760–2782, 1998.

[19] “Evolution of the NFL Player | NFL Football Operations.” https://operations.nfl.com/inside-football-ops/players-legends/evolution-of-the-nfl-player/ (accessed Apr. 14, 2022).

[20] “Traumatic brain injury - Symptoms and causes - Mayo Clinic.” https://www.mayoclinic.org/diseases-conditions/traumatic-brain-injury/symptoms-causes/syc-20378557 (accessed Apr. 09, 2022).

[21] “Traumatic Brain Injury (TBI): What Is It, Causes, Types,” *Cleveland Clinic*. https://my.clevelandclinic.org/health/diseases/8874-traumatic-brain-injury (accessed Apr. 09, 2022).

[22] “Get the Facts About TBI | Concussion | Traumatic Brain Injury | CDC Injury Center.” https://www.cdc.gov/traumaticbraininjury/get_the_facts.html (accessed Apr. 09, 2022).

[23] “Moderate and Severe TBI | Concussion | Traumatic Brain Injury | CDC Injury Center.” https://www.cdc.gov/traumaticbraininjury/moderate-severe/index.html (accessed Apr. 09, 2022).

[24] “TBI-related Emergency Department (ED) Visits | Concussion | Traumatic Brain Injury | CDC Injury Center.” https://www.cdc.gov/traumaticbraininjury/data/tbi-ed-visits_1_1.html (accessed Apr. 09, 2022).

[25] “TBI-related Emergency Department (ED) Visits,” *Centers for Disease Control and Prevention*, Mar. 15, 2019. https://www.cdc.gov/traumaticbraininjury/data/tbi-ed-visits_1_1.html (accessed Apr. 09, 2022).

[26] D. Waltzman, ; Lindsay, S. Womack, K. E. Thomas, and ; Kelly Sarmiento, “Trends in Emergency Department Visits for Contact Sports–Related Traumatic Brain Injuries Among Children — United States, 2001–2018,” *Morbidity and Mortality Weekly Report*, vol. 69, no. 27, pp. 870–874, Jul. 2001, [Online]. Available: https://surveillance.cancer.gov/joinpoint/

[27] L. Depadilla, G. F. Miller, ; Sherry, E. Jones, A. B. Peterson, and M. J. Breiding, “Self-Reported Concussions from Playing a Sport or Being Physically Active Among High School Students-United States, 2017,” *Morbidity and Mortality Weekly Report*, vol. 67, no. 24, pp. 682–685, Jun. 2018, [Online]. Available: https://nces.ed.gov/pubs2016/2016117rev.pdf.

[28] J. A. Langlois, W. Rutland-Brown, and M. M. Wald, “The Epidemiology and Impact of Traumatic Brain Injury A Brief Overview,” *Journal of Head Trauma Rehabil*, vol. 21, no. 5, pp. 375–378, 2006, [Online]. Available: www.headtraumarehab.com

[29] “Sports Concussion Policies and Laws | HEADS UP | CDC Injury Center.” https://www.cdc.gov/headsup/policy/index.html (accessed Apr. 09, 2022).

[30] “Implementing Return to Play: Learning from the Experiences of Early Implementers.”

[31] F. P. Rivara, M. A. Schiff, S. P. Chrisman, S. K. Chung, R. G. Ellenbogen, and S. A. Herring, "The effect of coach education on reporting of concussions among high school athletes after passage of a concussion law," *American Journal of Sports Medicine*, vol. 42, no. 5, pp. 1197–1203, 2014, doi: 10.1177/0363546514521774.

[32] V. N. Poole *et al.*, "MR spectroscopic evidence of brain injury in the non-diagnosed collision sport athlete," *Developmental Neuropsychology*, vol. 39, no. 6, pp. 459–473, Aug. 2014, doi: 10.1080/87565641.2014.940619.

[33] K. Abbas *et al.*, "Effects of repetitive sub-concussive brain injury on the functional connectivity of default mode network in high school football athletes," *Developmental Neuropsychology*, vol. 40, no. 1, pp. 51–56, Jan. 2015, doi: 10.1080/87565641.2014.990455.

[34] S. P. Broglio, D. Martini, L. Kasper, J. T. Eckner, and J. S. Kutcher, "Estimation of head impact exposure in high school football: Implications for regulating contact practices," *American Journal of Sports Medicine*, vol. 41, no. 12, pp. 2877–2884, Dec. 2013, doi: 10.1177/0363546513502458.

[35] J. E. Bailes, A. L. Petraglia, B. I. Omalu, E. Nauman, and T. Talavage, "Role of subconcussion in repetitive mild traumatic brain injury," *Journal of Neurosurgery*, vol. 119, no. 5, pp. 1235–1245, Nov. 2013, doi: 10.3171/2013.7.JNS121822.

[36] T. M. Talavage, E. A. Nauman, and L. J. Leverenz, "The role of medical imaging in the recharacterization of mild traumatic brain injury using youth sports as a laboratory," *Frontiers in Neurology*, vol. 6, no. JAN, Jan. 2016, doi: 10.3389/fneur.2015.00273.

[37] "1. Odds of high school players going pro | Football and Concussions." https://u.osu.edu/groupbetaengr2367/junran-add-things-here-for-real/ (accessed Apr. 09, 2022).

[38] B. I. Omalu, S. T. DeKosky, R. L. Minster, M. I. Kamboh, R. L. Hamilton, and C. H. Wecht, "Chronic traumatic encephalopathy in a National Football League player," *Neurosurgery*, vol. 57, no. 1, pp. 128–133, Jul. 2005, doi: 10.1227/01.NEU.0000163407.92769.ED.

[39] J. Mez *et al.*, "Clinicopathological evaluation of chronic traumatic encephalopathy in players of American football," *JAMA - Journal of the American Medical Association*, vol. 318, no. 4, pp. 360–370, Jul. 2017, doi: 10.1001/jama.2017.8334.

[40] “Leatherhead to Radio-head: The Evolution of the Football Helmet | Arts & Culture| Smithsonian Magazine.” https://www.smithsonianmag.com/arts-culture/leatherhead-to-radio-head-the-evolution-of-the-football-helmet-56585562/ (accessed Apr. 11, 2022).

[41] “Riddell History.” https://content.riddell.com/history/ (accessed Apr. 11, 2022).

[42] “Recalling when the NFL made helmets mandatory - ProFootballTalk.” https://profootballtalk.nbcsports.com/2014/04/07/recalling-when-the-nfl-made-helmets-mandatory/ (accessed Apr. 11, 2022).

[43] “History – NOCSAE.” https://nocsae.org/about-nocsae/history/ (accessed Apr. 11, 2022).

[44] “Certification – NOCSAE.” https://nocsae.org/certification/ (accessed Apr. 12, 2022).

[45] “NOCSAE Issues Clarification About Football Helmet Certification to NOCSAE Standards – NOCSAE.” https://nocsae.org/nocsae-issues-clarification-about-football-helmet-certification-to-nocsae-standards/ (accessed Apr. 12, 2022).

[46] “STANDARD PERFORMANCE SPECIFICATION FOR NEWLY MANUFACTURED FOOTBALL HELMETS,” Jun. 2021.

[47] “STANDARD TEST METHOD AND EQUIPMENT USED IN EVALUATING THE PERFORMANCE CHARACTERISTICS OF HEADGEAR/EQUIPMENT,” Jun. 2020.

[48] “The Science of Football: Which Positions Take the Hardest Hits? | Live Science.” https://www.livescience.com/54972-which-football-positions-take-hardest-hits.html (accessed Apr. 15, 2022).

[49] “Virtual Human Models - Elemance.” https://www.elemance.com/models/ (accessed Apr. 06, 2022).

[50] “Toyota Updates its THUMS Virtual Crash Dummy Software | Corporate | Global Newsroom | Toyota Motor Corporation Official Global Website.” https://global.toyota/en/newsroom/corporate/26497281.html (accessed Apr. 06, 2022).

[51] D. Kato, Y. Nakahira, N. Atsumi, and M. Iwamoto, “Development of Human-Body THUMS Version 6 containnig Muscle Controllers and Application to Injury Analysis in Frontal Collision after Brake Deceleration,” *IRCOBI Conference* , 2018.

[52] “Toyota Offers Free Access to THUMS Virtual Human Body Model Software | Corporate | Global Newsroom | Toyota Motor Corporation Official Global Website.” https://global.toyota/en/newsroom/corporate/32665896.html (accessed Apr. 06, 2022).

[53] A. Awoukeng Goumtcha, M. Bodo, L. Taddei, and S. Roth, “From military to civil loadings: Preliminary numerical-based thorax injury criteria investigations,” *International Journal for Numerical Methods in Biomedical Engineering*, vol. 32, no. 3, pp. 1–14, Mar. 2016, doi: 10.1002/cnm.2738.

[54] A. Bracq, R. Delille, C. Maréchal, B. Bourel, S. Roth, and O. Mauzac, “Rib fractures prediction method for kinetic energy projectile impact: from blunt ballistic experiments on SEBS gel to impact modeling on a human torso FE model,” *Forensic Science International*, vol. 297, pp. 177–183, Apr. 2019, doi: 10.1016/j.forsciint.2019.02.007.

[55] “PIPER Software Framework and Application: User guide Position and Personalize Advanced Human Body Models for Injury Prediction.” 2017. [Online]. Available: http://doc.piper-project.org/framework/1.0.1/user-guide.pdf

[56] E. Jolivet, Y. Lafon, P. Petit, and P. Beillas, “Comparison of Kriging and Moving Least Square Methods to Change the Geometry of Human Body Models Erwan Jolivet CEESAR-European center of studies and risk analysis, France,” *Stapp Car Crash Journal*, vol. 59, pp. 337–357, 2015, [Online]. Available: http://www.piper-project.eu/

[57] T. Janák, Y. Lafon, P. Petit, and P. Beillas, “A method to use kriging with large sets of control points to morph finite element models of the human body,” *Journal of Biomechanical Engineering*, vol. 143, no. 2, Feb. 2021, doi: 10.1115/1.4048575.

[58] K. Zhang *et al.*, “An automated method to morph finite element whole-body human models with a wide range of stature and body shape for both men and women,” *Journal of Biomechanics*, vol. 60, pp. 253–260, Jul. 2017, doi: 10.1016/j.jbiomech.2017.06.015.

[59] J. Mckee, “Scaling a Human Body Finite Element Model with Radial Basis Function Interpolation,” Jun. 2018.

[60] J. A. Newman, M. C. Beusenberg, N. Shewchenko, C. Withnall, and E. Fournier, “Verification of biomechanical methods employed in a comprehensive study of mild traumatic brain injury and the effectiveness of American football helmets,” *Journal of Biomechanics*, vol. 38, no. 7, pp. 1469–1481, Jul. 2005, doi: 10.1016/j.jbiomech.2004.06.025.

[61] K. Kormi and R. A. Etheridge, “Application of the finite-element method to simulation of damage to the human skull as a consequence of missile impact on a multi-layered composite crash helmet,” *Journal of Biomedical Engineering*, vol. 14, pp. 203–208, May 1992.

[62] W. C. Moss and M. J. King, “Impact response of US Army and National Football League helmet pad systems,” 2011.

[63] V. Tinard, C. Deck, and R. Willinger, “New methodology for improvement of helmet performances during impacts with regards to biomechanical criteria,” *Materials and Design*, vol. 37, pp. 79–88, May 2012, doi: 10.1016/j.matdes.2011.12.005.

[64] J. M. Johnston *et al.*, “Simulation, fabrication and impact testing of a novel football helmet padding system that decreases rotational acceleration,” *Sports Engineering*, vol. 18, no. 1, pp. 11–20, Mar. 2015, doi: 10.1007/s12283-014-0160-4.

[65] T. Darling, J. Muthuswamy, and S. D. Rajan, “Finite element modeling of human brain response to football helmet impacts,” *Computer Methods in Biomechanics and Biomedical Engineering*, vol. 19, no. 13, pp. 1432–1442, Oct. 2016, doi: 10.1080/10255842.2016.1149574.

[66] “Finite Element Models - Biocore, LLC.” https://biocorellc.com/finite-element-models/ (accessed Apr. 12, 2022).

[67] M. A. Corrales, D. Gierczycka, J. Barker, D. Bruneau, M. C. Bustamante, and D. S. Cronin, “Validation of a Football Helmet Finite Element Model and Quantification of Impact Energy Distribution,” *Annals of Biomedical Engineering*, vol. 48, no. 1, pp. 121–132, Jan. 2020, doi: 10.1007/s10439-019-02359-1.

[68] D. Cronin, J. Barker, D. Gierczycka, D. Bruneau, and M. Bustamante, “User Manual Finite Element Model of 2016 Xenith X2E (Safety Equipment Institute model X2E) Version 1.0 for LS-DYNA,” May 2018. [Online]. Available: www.biocorellc.com

[69] D. A. Bruneau and D. S. Cronin, “Brain response of a computational head model for prescribed skull kinematics and simulated football helmet impact boundary conditions,” *Journal of the Mechanical Behavior of Biomedical Materials*, vol. 115, Mar. 2021, doi: 10.1016/j.jmbbm.2020.104299.

[70] W. Decker, A. Baker, X. Ye, P. Brown, J. Stitzel, and F. S. Gayzik, “Development and Multi-Scale Validation of a Finite Element Football Helmet Model,” *Annals of Biomedical Engineering*, vol. 48, no. 1, pp. 258–270, Jan. 2020, doi: 10.1007/s10439-019-02345-7.

[71] W. Decker, X. Ye, A. Baker, J. Stitzel, S. Gayzik, and J. D. Stitzel, “User Manual Finite Element Model of 2016 Schutt Air XP Pro Helmet (Safety Equipment Institute model 789102) Version 1.0 for LS-DYNA Document Version (v) 1.0,” 2018. [Online]. Available: www.biocorellc.com

[72] J. S. Giudice, G. Park, K. Kong, A. Bailey, R. Kent, and M. B. Panzer, “Development of Open-Source Dummy and Impactor Models for the Assessment of American Football Helmet Finite Element Models,” *Annals of Biomedical Engineering*, vol. 47, no. 2, pp. 464–474, Feb. 2019, doi: 10.1007/s10439-018-02155-3.

[73] J. S. Giudice *et al.*, “Finite Element Model of a Deformable American Football Helmet Under Impact,” *Annals of Biomedical Engineering*, vol. 48, no. 5, pp. 1524–1539, May 2020, doi: 10.1007/s10439-020-02472-6.

[74] S. T. Mills, T. S. Young, L. S. Chatham, S. Poddar, R. D. Carpenter, and C. M. Yakacki, “Effect of foam densification and impact velocity on the performance of a football helmet using computational modeling,” *Computer Methods in Biomechanics and Biomedical Engineering*, vol. 24, no. 1, pp. 21–32, 2021, doi: 10.1080/10255842.2020.1807015.

[75] “Zygote::Solid 3D Male Model | Medically Accurate | Anatomy | Human (CAD).” https://www.zygote.com/cad-models/collections-products/solid-3d-male-collection (accessed Apr. 13, 2022).

[76] Corvid Technologies, “CAVEMAN User Manual For CAVEMAN Version 21.4.”

[77] “MATLAB - MathWorks - MATLAB & Simulink.” https://www.mathworks.com/products/matlab.html (accessed Apr. 16, 2022).

[78] “LS-PrePost | Livermore Software Technology Corp.” https://www.lstc.com/products/ls-prepost (accessed Apr. 16, 2022).

[79] T. Baltis *et al.*, “Positioning and Scaling of the CAVEMAN Human Body Model for Pilot Injury Risk Analysis Deliverable 0003.” May 14, 2021.

[80] T. Baltis *et al.*, “Positioning and Scaling of the CAVEMAN Human Body Model for Pilot Injury Risk Analysis Deliverable 0005.” Sep. 14, 2021.

[81] S. Bhutani, E. Kahn, E. Tasali, and D. A. Schoeller, “Composition of two-week change in body weight under unrestricted free-living conditions,” *Physiological Reports*, vol. 15, no. 13, 2017, doi: 10.14814/phy2.13336.

[82] J. Turicchi *et al.*, “Weekly, seasonal and holiday body weight fluctuation patterns among individuals engaged in a European multi-centre behavioural weight loss maintenance intervention,” *PLoS ONE*, vol. 15, no. 4, Apr. 2020, doi: 10.1371/journal.pone.0232152.

[83] A. L. Orsama, E. Mattila, M. Ermes, M. van Gils, B. Wansink, and I. Korhonen, “Weight rhythms: Weight increases during weekends and decreases during weekdays,” *Obesity Facts*, vol. 7, no. 1, pp. 36–47, 2014, doi: 10.1159/000356147.

[84] B. Cummiskey *et al.*, “Quantitative evaluation of impact attenuation by football helmets using a modal impulse hammer,” *Proceedings of the Institution of Mechanical Engineers, Part P: Journal of Sports Engineering and Technology*, vol. 233, no. 2, pp. 301–311, Jun. 2019, doi: 10.1177/1754337118823603.

[85] B. R. Cummiskey, “Characterization and Evaluation of Head Impact Sensors and Varsity Football Helmets,” Master of Science, Purdue University, 2015.

[86] “VELODYNE SOFTWARE | Corvid Technologies.” https://www.corvidtec.com/velodyne-software (accessed Apr. 16, 2022).

[87] “coreform Cubit.” https://coreform.com/products/coreform-cubit/ (accessed Apr. 16, 2022).

[88] “SOLIDWORKS.” https://www.solidworks.com/ (accessed Apr. 16, 2022).

[89] “VisIt | Weapons and Complex Integration.” https://wci.llnl.gov/simulation/computer-codes/visit (accessed Apr. 16, 2022).

[90] K. G. McIver, “ENGINEERING BETTER PROTECTIVE HEADGEAR FOR SPORT AND MILITARY APPLICATIONS,” Purdue University, 2019.

[91] M. Fahlstedt, M. Arnesen, E. Jungstedt, and P. Halldin, “Helmet Model Riddell Revolution Speed Classic v1.0 User Manual Finite Element Model of 2016 Riddell Speed Classic (Safety Equipment Institute model R41179) Version 1.0 for LS-DYNA Document Version (v) 1.0,” 2018. [Online]. Available: www.kth.se/mth/neuronik

APPENDIX A. ANTHROPOMETRIC MEASUREMENTS

Measurement Number	Description	ANSUR II 50th Percentile	ANSUR II 50th Percentile Standard Deviation	Zygote CAD Measurement	Measurement Error	Measurement Within One Standard Deviation?	Measurement Error Outside One Standard Deviation (cm)
2	Acromion-Radiale Length	33.48	1.73	34.4	2.7%	Yes	
5	Ankle Circumference	22.69	1.36	18.8	17.1%	No	2.53
8	Axilla Height	132.67	6.01	131.6	0.8%	Yes	
12	Ball of Foot Circumference	25.19	1.29	21.2	15.8%	No	2.7
13	Biacromal Breadth	40.88	1.97	38.9	4.8%	Yes	
19	Bimalleolar Breadth	7.33	0.39	6.9	5.9%	No	0.04
24	Bitragion-Menton Arc	32.95	1.32	33.1	0.5%	Yes	
27	Bitragion-Submandibular Arc	30.91	1.47	30.4	1.6%	Yes	
30	Buttock Depth	23.73	2.17	23.4	1.4%	Yes	
31	Buttock Height	88.81	4.71	87.6	1.4%	Yes	
34	Calf Circumference	38.41	2.64	38.3	0.3%	Yes	
36	Cervical Height	151.07	6.36	150.4	0.4%	Yes	
37	Chest Breadth	28.47	1.78	31.3	9.9%	No	1.05
38	Chest/Bust Circumference	103.02	7.59	103.3	0.3%	Yes	
39	Chest/Bust Depth	25.54	2.19	25.6	0.2%	Yes	
40	Chest/Bustpoint Height	129.1	5.84	129.5	0.3%	Yes	
43	Crotch Height	85.49	4.63	79	7.6%	No	1.86
47	Ear Breadth	3.61	0.27	3.5	3.0%	Yes	
48	Ear Length	6.47	0.41	5.8	10.4%	No	0.26
50	Ear Protrusion	2.34	0.31	1.6	31.6%	No	0.43
55	Elbow-Fingertip Length	47.69	2.29	45.7	4.2%	Yes	
56	Elbow-Grip Length	35.02	1.75	33.6	4.1%	Yes	
60	Elbow-Wrist Length	28.31	1.52	28.4	0.3%	Yes	
63	Face Length (Menton-Sellion)	12.4	0.66	11.6	6.5%	No	0.14
67	Foot Breadth	10.12	0.53	9.6	5.1%	Yes	
68	Foot Length	27.1	1.28	26.4	2.6%	Yes	
79	Hand Breadth	8.95	0.44	8.7	2.8%	Yes	
81	Hand Circumference	21.1	0.99	21.7	2.8%	Yes	
83	Hand Length	19.38	0.96	18.3	5.6%	No	0.12
85	Head Breadth	15.4	0.54	15.3	0.6%	Yes	
86	Head Circumference	57.1	1.52	56.7	0.7%	Yes	
89	Head Height (Tragion to top of head)	13.15	0.64	12.1	8.0%	No	0.41
90	Head Length	19.89	0.68	20.1	1.1%	Yes	
91	Heel-Ankle Circumference	33.99	1.6	33.5	1.4%	Yes	
92	Heel Breadth	7.05	0.48	6.1	13.5%	No	0.47
94	Hip Breadth, Standing	34.23	2.19	33.3	2.7%	Yes	
96	Hip (Bottock) Circumference, Standing	100.6	6.77	100	0.6%	Yes	
97	Hip (Trochanteric Height)	91.45	4.8	90.7	0.8%	Yes	
99	Instep Length	20.03	1.01	19.8	1.1%	Yes	
101	Interpupillary Breadth	6.35	0.34	5.7	10.2%	No	0.31
102	Interscye, Back	42.4	3.33	39.4	7.1%	Yes	
108	Knee Height, Midpatella	49.53	2.79	49.9	0.7%	Yes	
113	Lateral Malleolus Height	6.94	0.7	7.3	5.2%	Yes	
116	Lower Thigh Circumference	40.28	2.97	39.1	2.9%	Yes	
133	Neck Circumference	39.09	2.17	41.6	6.4%	No	0.34
138	Palm Length	11.64	0.62	10	14.1%	No	1.02
145	Radiale-Stylion Length	26.54	1.48	24.8	6.6%	No	0.26
150	Shoulder (Acromiale) Height, Standing	143.37	6.38	146.1	1.9%	Yes	
151	Shoulder (Bideltoid) Breadth	49.79	2.77	49.7	0.2%	Yes	
152	Shoulder Circumerence	116.32	5.9	118.6	2.0%	Yes	
154	Shoulder-Fingertip Length	78.99	3.83	78.2	1.0%	Yes	
156	Shoulder Length	14.83	1.06	14.3	3.6%	Yes	
158	Sleve Inseam Length	48.91	2.94	44.9	8.2%	No	1.07
163	Stature	175.34	6.97	175.4	0.0%	Yes	
173	Suprasternal Height	143.5	6.17	144.2	0.5%	Yes	
176	Tibiale Height	47.83	2.6	46	3.8%	Yes	
177	Tragion Height, Standing	162.19	6.88	163.7	0.9%	Yes	
178	Thigh Circumference, Standing	61.22	5.36	60	2.0%	Yes	
185	Waist Back Length (Omphalion)	46.35	2.7	44.7	3.6%	Yes	
187	Waist Depth (Omphalion)	21.94	2.56	21.7	1.1%	Yes	
189	Waist Front Length (Omphalion)	38.61	2.59	39.3	1.8%	Yes	
193	Waist Breadth (Omphalion)	31.15	2.97	30.7	1.4%	Yes	
195	Waist Circumference (Omphalion)	88.4	8.9	87.3	1.2%	Yes	
198	Waist Height (Omphalion)	105.94	5.19	105	0.9%	Yes	
202	Wrist Circumference	17.67	0.83	18.6	5.3%	No	0.1

Total Measurements Within One Standard Deviation:	74%
Average Measurement Error:	4.2%
Average Measurement Error Outiside One Standard Deviation (cm):	0.77

Figure A.1 Anthropometric measurements for the CAVEMAN 50th percentile HBM. Figure from [76].

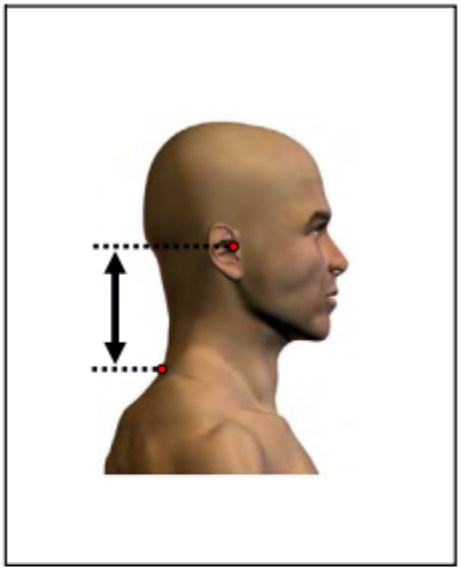

PERCENTILES				
FEMALES			MALES	
CM	IN		CM	IN
8.32	3.28	1ST	7.81	3.07
8.60	3.39	2ND	8.30	3.27
8.86	3.49	3RD	8.60	3.39
9.01	3.54	5TH	8.80	3.46
9.50	3.74	10TH	9.40	3.70
9.70	3.82	15TH	9.70	3.82
10.00	3.94	20TH	9.90	3.90
10.10	3.98	25TH	10.20	4.02
10.30	4.06	30TH	10.40	4.09
10.40	4.09	35TH	10.60	4.17
10.50	4.13	40TH	10.70	4.21
10.65	4.19	45TH	11.00	4.33
10.80	4.25	50TH	11.10	4.37
11.00	4.33	55TH	11.20	4.41
11.10	4.37	60TH	11.40	4.49
11.30	4.45	65TH	11.60	4.57
11.50	4.53	70TH	11.80	4.65
11.70	4.61	75TH	12.10	4.76
11.90	4.69	80TH	12.30	4.84
12.20	4.80	85TH	12.50	4.92
12.40	4.88	90TH	12.90	5.08
12.90	5.08	95TH	13.50	5.31
13.10	5.16	97TH	13.70	5.39
13.20	5.20	98TH	14.10	5.55
13.74	5.40	99TH	14.50	5.71

Figure A.2 Illustration and list of percentiles for neck link anthropometric measurement from ANSURII used to inform scaling of the neck. Figure from [1].

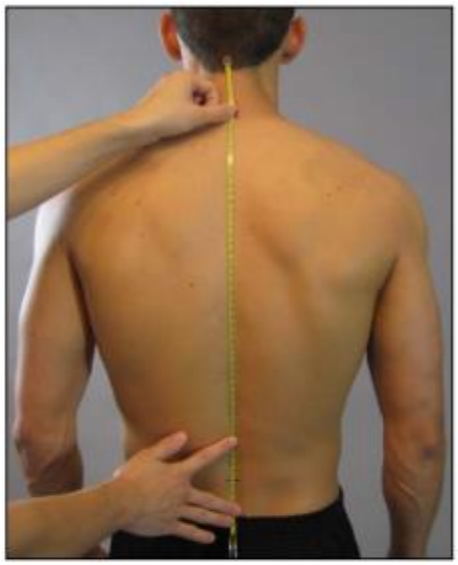

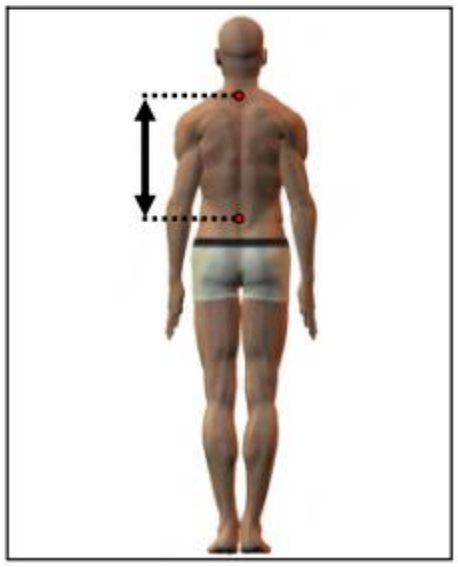

PERCENTILES				
FEMALES			MALES	
CM	IN		CM	IN
37.00	14.57	1ST	40.20	15.83
37.38	14.72	2ND	40.90	16.10
37.66	14.83	3RD	41.40	16.30
38.20	15.04	5TH	42.00	16.54
39.20	15.43	10TH	42.90	16.89
39.62	15.60	15TH	43.50	17.13
40.20	15.83	20TH	44.10	17.36
40.70	16.02	25TH	44.50	17.52
41.10	16.18	30TH	44.90	17.68
41.40	16.30	35TH	45.27	17.82
41.70	16.42	40TH	45.60	17.95
42.00	16.54	45TH	46.00	18.11
42.40	16.69	50TH	46.20	18.19
42.66	16.79	55TH	46.60	18.35
43.00	16.93	60TH	47.00	18.50
43.27	17.04	65TH	47.40	18.66
43.60	17.17	70TH	47.70	18.78
43.98	17.31	75TH	48.20	18.98
44.40	17.48	80TH	48.70	19.17
45.10	17.76	85TH	49.17	19.36
45.79	18.03	90TH	49.80	19.61
46.90	18.46	95TH	50.70	19.96
47.44	18.67	97TH	51.50	20.28
47.66	18.76	98TH	52.10	20.51
49.07	19.32	99TH	52.99	20.87

Figure A.3 Illustration and list of percentiles for waist back length anthropometric measurement from ANSURII used to inform scaling of the torso below the neck. Figure from [1].

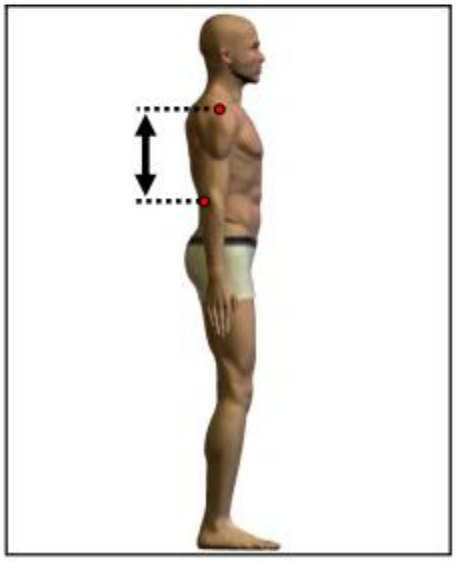

PERCENTILES				
FEMALES			MALES	
CM	IN		CM	IN
27.72	10.92	1ST	29.40	11.57
28.00	11.02	2ND	29.90	11.77
28.30	11.14	3RD	30.30	11.93
28.51	11.22	5TH	30.80	12.13
29.10	11.46	10TH	31.30	12.32
29.40	11.57	15TH	31.70	12.48
29.70	11.69	20TH	32.00	12.60
30.00	11.81	25TH	32.40	12.76
30.20	11.89	30TH	32.60	12.83
30.50	12.01	35TH	32.80	12.91
30.70	12.09	40TH	33.00	12.99
31.00	12.20	45TH	33.20	13.07
31.10	12.24	50TH	33.40	13.15
31.30	12.32	55TH	33.60	13.23
31.46	12.38	60TH	33.80	13.31
31.67	12.47	65TH	34.10	13.43
31.90	12.56	70TH	34.40	13.54
32.10	12.64	75TH	34.60	13.62
32.40	12.76	80TH	34.90	13.74
32.70	12.87	85TH	35.30	13.90
33.00	12.99	90TH	35.60	14.02
33.70	13.27	95TH	36.40	14.33
34.14	13.44	97TH	36.90	14.53
34.66	13.64	98TH	37.20	14.65
35.20	13.86	99TH	37.70	14.84

Figure A.4 Illustration and list of percentiles for acromion-radiale length anthropometric measurement from ANSURII used to inform scaling of the upper arm. Figure from [1].

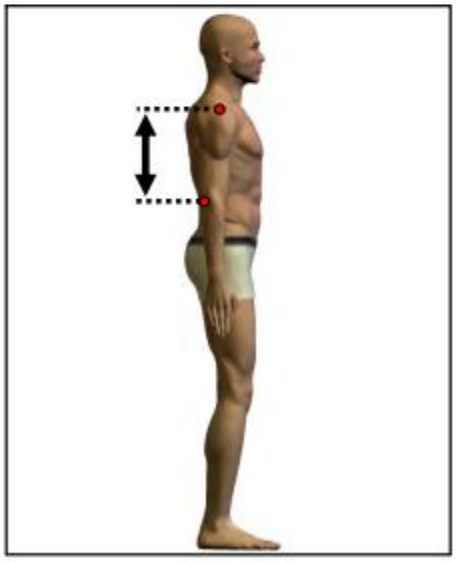

PERCENTILES				
FEMALES			MALES	
CM	IN		CM	IN
27.72	10.92	1ST	29.40	11.57
28.00	11.02	2ND	29.90	11.77
28.30	11.14	3RD	30.30	11.93
28.51	11.22	5TH	30.80	12.13
29.10	11.46	10TH	31.30	12.32
29.40	11.57	15TH	31.70	12.48
29.70	11.69	20TH	32.00	12.60
30.00	11.81	25TH	32.40	12.76
30.20	11.89	30TH	32.60	12.83
30.50	12.01	35TH	32.80	12.91
30.70	12.09	40TH	33.00	12.99
31.00	12.20	45TH	33.20	13.07
31.10	12.24	50TH	33.40	13.15
31.30	12.32	55TH	33.60	13.23
31.46	12.38	60TH	33.80	13.31
31.67	12.47	65TH	34.10	13.43
31.90	12.56	70TH	34.40	13.54
32.10	12.64	75TH	34.60	13.62
32.40	12.76	80TH	34.90	13.74
32.70	12.87	85TH	35.30	13.90
33.00	12.99	90TH	35.60	14.02
33.70	13.27	95TH	36.40	14.33
34.14	13.44	97TH	36.90	14.53
34.66	13.64	98TH	37.20	14.65
35.20	13.86	99TH	37.70	14.84

Figure A.5 Illustration and list of percentiles for radiale-stylion length anthropometric measurement from ANSURII used to inform scaling of the lower arm. Figure from [1].

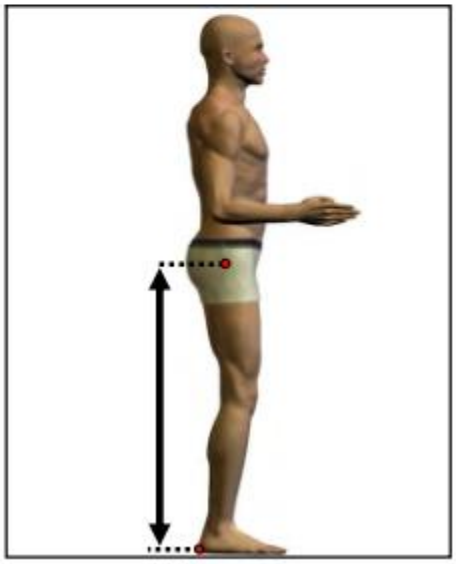

PERCENTILES				
FEMALES			MALES	
CM	IN		CM	IN
74.90	29.49	1ST	78.80	31.02
75.74	29.82	2ND	79.70	31.38
76.30	30.04	3RD	80.40	31.65
77.01	30.31	5TH	81.31	32.01
78.50	30.91	10TH	83.00	32.68
79.30	31.22	15TH	84.00	33.07
80.20	31.57	20TH	84.80	33.39
80.90	31.85	25TH	85.50	33.66
81.30	32.01	30TH	86.20	33.94
82.10	32.32	35TH	86.90	34.21
82.60	32.52	40TH	87.50	34.45
83.20	32.76	45TH	88.10	34.69
83.80	32.99	50TH	88.60	34.88
84.40	33.23	55TH	89.20	35.12
84.90	33.43	60TH	89.80	35.35
85.50	33.66	65TH	90.40	35.59
86.07	33.89	70TH	91.00	35.83
86.70	34.13	75TH	91.80	36.14
87.30	34.37	80TH	92.70	36.50
88.10	34.69	85TH	93.70	36.89
89.10	35.08	90TH	95.10	37.44
90.80	35.75	95TH	97.19	38.27
92.04	36.23	97TH	98.40	38.74
92.99	36.61	98TH	99.30	39.09
95.20	37.48	99TH	101.29	39.88

Figure A.6 Illustration and list of percentiles for buttock height anthropometric measurement from ANSURII used to inform scaling of the upper leg. Figure from [1].

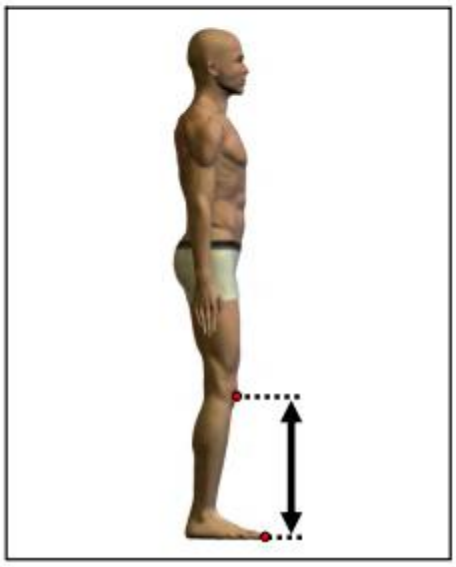

PERCENTILES				
FEMALES			MALES	
CM	IN		CM	IN
40.04	15.77	1ST	43.70	17.20
40.34	15.89	2ND	44.20	17.40
40.83	16.07	3RD	44.50	17.52
41.21	16.22	5TH	45.20	17.80
42.20	16.61	10TH	46.00	18.11
42.80	16.85	15TH	46.60	18.35
43.12	16.98	20TH	47.20	18.58
43.50	17.13	25TH	47.60	18.74
43.80	17.24	30TH	48.06	18.92
44.30	17.44	35TH	48.40	19.06
44.60	17.56	40TH	48.80	19.21
45.00	17.72	45TH	49.10	19.33
45.30	17.83	50TH	49.30	19.41
45.60	17.95	55TH	49.70	19.57
45.90	18.07	60TH	50.10	19.72
46.20	18.19	65TH	50.40	19.84
46.50	18.31	70TH	50.80	20.00
46.80	18.43	75TH	51.30	20.20
47.20	18.58	80TH	52.00	20.47
47.70	18.78	85TH	52.50	20.67
48.20	18.98	90TH	53.20	20.94
49.20	19.37	95TH	54.30	21.38
49.87	19.64	97TH	55.00	21.65
50.47	19.87	98TH	55.60	21.89
51.38	20.23	99TH	56.70	22.32

Figure A.7 Illustration and list of percentiles for knee height (midpatella) anthropometric measurement from ANSURII used to inform scaling of the upper and lower leg. Figure from [1].

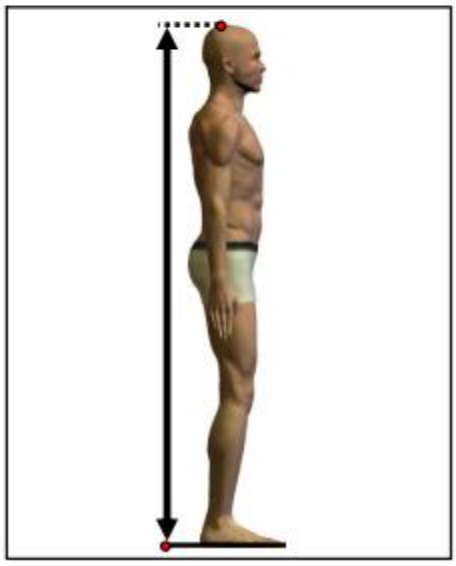

PERCENTILES				
FEMALES			MALES	
CM	IN		CM	IN
149.12	58.71	1ST	160.61	63.23
150.44	59.23	2ND	161.80	63.70
150.86	59.40	3RD	163.00	64.17
152.31	59.96	5TH	164.70	64.84
154.30	60.75	10TH	166.50	65.55
155.72	61.31	15TH	167.73	66.03
156.80	61.73	20TH	169.30	66.65
158.03	62.21	25TH	170.75	67.22
159.30	62.72	30TH	171.70	67.60
160.20	63.07	35TH	172.50	67.91
161.00	63.39	40TH	173.28	68.22
161.80	63.70	45TH	174.30	68.62
162.60	64.02	50TH	175.00	68.90
163.20	64.25	55TH	175.90	69.25
164.00	64.57	60TH	176.70	69.57
164.77	64.87	65TH	177.50	69.88
165.50	65.16	70TH	178.64	70.33
166.48	65.54	75TH	179.80	70.79
167.80	66.06	80TH	181.30	71.38
169.10	66.57	85TH	182.77	71.96
170.59	67.17	90TH	184.98	72.82
173.50	68.31	95TH	187.30	73.74
174.67	68.77	97TH	189.20	74.49
175.50	69.09	98TH	190.50	75.00
177.05	69.70	99TH	192.10	75.63

Figure A.8 Illustration and list of percentiles for stature anthropometric measurement from ANSURII. Figure from [1].

PERCENTILES				
FEMALES			MALES	
KG	LB		KG	LB
47.33	104.34	1ST	57.40	126.53
48.33	106.54	2ND	58.80	129.63
49.28	108.65	3RD	60.39	133.15
50.87	112.14	5TH	62.48	137.75
53.32	117.55	10TH	65.70	144.84
55.31	121.93	15TH	68.50	151.02
56.88	125.40	20TH	70.40	155.20
57.90	127.65	25TH	71.90	158.51
58.60	129.19	30TH	73.60	162.26
59.79	131.82	35TH	75.00	165.35
60.76	133.95	40TH	76.60	168.87
62.30	137.35	45TH	77.90	171.74
63.30	139.55	50TH	79.90	176.15
64.07	141.24	55TH	81.40	179.45
65.14	143.61	60TH	83.10	183.20
66.20	145.94	65TH	84.87	187.10
67.40	148.59	70TH	86.60	190.92
68.50	151.02	75TH	88.25	194.56
70.10	154.54	80TH	90.80	200.18
71.48	157.59	85TH	93.13	205.32
74.66	164.59	90TH	96.52	212.78
77.29	170.40	95TH	101.72	224.25
80.52	177.51	97TH	104.22	229.76
83.59	184.28	98TH	106.92	235.71
88.17	194.39	99TH	111.10	244.93

Figure A.9 Illustration and list of percentiles for weight anthropometric measurement from ANSURII. Figure from [1].

FEMALES		
KG		LB
63.60	MEAN	140.22
0.34	STD ERROR (MEAN)	0.75
8.40	STANDARD DEVIATION	18.53
0.24	STD ERROR (STD DEV)	0.53
44.00	MINIMUM	97.00
113.80	MAXIMUM	250.88
SKEWNESS		0.76
KURTOSIS		5.19
COEFFICIENT OF VARIATION		13.2%
NUMBER OF PARTICIPANTS		613

MALES		
KG		LB
80.60	MEAN	177.68
0.33	STD ERROR (MEAN)	0.73
11.88	STANDARD DEVIATION	26.18
0.23	STD ERROR (STD DEV)	0.51
51.90	MINIMUM	114.42
123.10	MAXIMUM	271.39
SKEWNESS		0.36
KURTOSIS		2.96
COEFFICIENT OF VARIATION		14.7%
NUMBER OF PARTICIPANTS		1297

FREQUENCIES

FEMALES							MALES			
F	FPct	CumF	CumFPct	KG			F	FPct	CumF	CumFPct
1	0.16	1	0.16	42.55	-	44.55				
2	0.33	3	0.49	44.55	-	46.55				
11	1.79	14	2.28	46.55	-	48.55				
11	1.79	25	4.08	48.55	-	50.55				
28	4.57	53	8.65	50.55	-	52.55	2	0.15	2	0.15
26	4.24	79	12.89	52.55	-	54.55	2	0.15	4	0.31
36	5.87	115	18.76	54.55	-	56.55	7	0.54	11	0.85
66	10.77	181	29.53	56.55	-	58.55	13	1.00	24	1.85
59	9.62	240	39.15	58.55	-	60.55	20	1.54	44	3.39
43	7.01	283	46.17	60.55	-	62.55	22	1.70	66	5.09
69	11.26	352	57.42	62.55	-	64.55	40	3.08	106	8.17
58	9.46	410	66.88	64.55	-	66.55	37	2.85	143	11.03
52	8.48	462	75.37	66.55	-	68.55	52	4.01	195	15.03
36	5.87	498	81.24	68.55	-	70.55	76	5.86	271	20.89
38	6.20	536	87.44	70.55	-	72.55	76	5.86	347	26.75
15	2.45	551	89.89	72.55	-	74.55	85	6.55	432	33.31
26	4.24	577	94.13	74.55	-	76.55	85	6.55	517	39.86
10	1.63	587	95.76	76.55	-	78.55	85	6.55	602	46.41
8	1.31	595	97.06	78.55	-	80.55	74	5.71	676	52.12
4	0.65	599	97.72	80.55	-	82.55	81	6.25	757	58.37
4	0.65	603	98.37	82.55	-	84.55	73	5.63	830	63.99
2	0.33	605	98.69	84.55	-	86.55	74	5.71	904	69.70
3	0.49	608	99.18	86.55	-	88.55	83	6.40	987	76.10
0	0.00	608	99.18	88.55	-	90.55	45	3.47	1032	79.57
3	0.49	611	99.67	90.55	-	92.55	54	4.16	1086	83.73
1	0.16	612	99.84	92.55	-	94.55	51	3.93	1137	87.66
0	0.00	612	99.84	94.55	-	96.55	31	2.39	1168	90.05
0	0.00	612	99.84	96.55	-	98.55	35	2.70	1203	92.75
0	0.00	612	99.84	98.55	-	100.55	22	1.70	1225	94.45
0	0.00	612	99.84	100.55	-	102.55	15	1.16	1240	95.61
0	0.00	612	99.84	102.55	-	104.55	20	1.54	1260	97.15
0	0.00	612	99.84	104.55	-	106.55	10	0.77	1270	97.92
0	0.00	612	99.84	106.55	-	108.55	7	0.54	1277	98.46
0	0.00	612	99.84	108.55	-	110.55	6	0.46	1283	98.92
0	0.00	612	99.84	110.55	-	112.55	7	0.54	1290	99.46
1	0.16	613	100.00	112.55	-	114.55	1	0.08	1291	99.54
				114.55	-	116.55	1	0.08	1292	99.61
				116.55	-	118.55	1	0.08	1293	99.69
				118.55	-	120.55	1	0.08	1294	99.77
				120.55	-	122.55	2	0.15	1296	99.92
				122.55	-	124.55	1	0.08	1297	100.00

Figure A.10 Statistics for weight anthropometric measurement in ANSURII. Figure from [1].

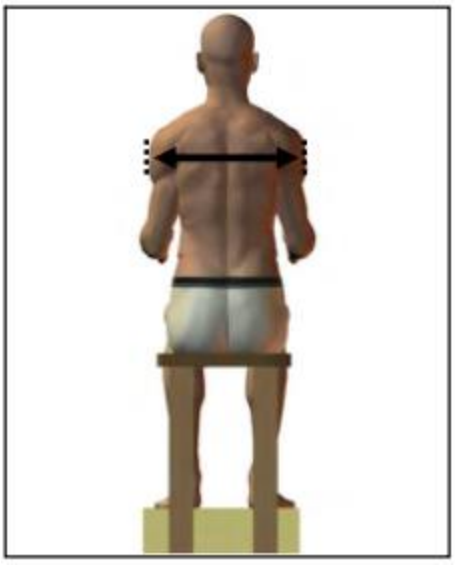

PERCENTILES				
FEMALES			MALES	
CM	IN		CM	IN
39.90	15.71	1ST	43.70	17.20
40.14	15.81	2ND	44.30	17.44
40.50	15.94	3RD	44.70	17.60
40.61	15.98	5TH	45.40	17.87
41.30	16.26	10TH	46.20	18.19
41.90	16.50	15TH	46.90	18.46
42.30	16.65	20TH	47.40	18.66
42.60	16.77	25TH	48.00	18.90
43.00	16.93	30TH	48.30	19.02
43.20	17.01	35TH	48.70	19.17
43.60	17.17	40TH	49.10	19.33
43.90	17.28	45TH	49.40	19.45
44.10	17.36	50TH	49.80	19.61
44.40	17.48	55TH	50.01	19.69
44.70	17.60	60TH	50.50	19.88
45.00	17.72	65TH	50.80	20.00
45.27	17.82	70TH	51.20	20.16
45.60	17.95	75TH	51.60	20.31
46.00	18.11	80TH	52.06	20.49
46.50	18.31	85TH	52.60	20.71
47.00	18.50	90TH	53.40	21.02
48.20	18.98	95TH	54.40	21.42
48.50	19.09	97TH	55.09	21.69
49.06	19.31	98TH	55.80	21.97
49.86	19.63	99TH	56.80	22.36

Figure A.11 Illustration and list of percentiles for bideltoid breadth anthropometric measurement from ANSURII. Figure from [1].

FEMALES		
CM		IN
162.49	MEAN	63.97
0.25	STD ERROR (MEAN)	0.10
6.22	STANDARD DEVIATION	2.45
0.18	STD ERROR (STD DEV)	0.07
145.40	MINIMUM	57.24
180.40	MAXIMUM	71.02
SKEWNESS		0.09
KURTOSIS		2.75
COEFFICIENT OF VARIATION		3.8%
NUMBER OF PARTICIPANTS		620

MALES		
CM		IN
175.34	MEAN	69.03
0.19	STD ERROR (MEAN)	0.08
6.97	STANDARD DEVIATION	2.75
0.14	STD ERROR (STD DEV)	0.05
151.80	MINIMUM	59.76
197.50	MAXIMUM	77.76
SKEWNESS		0.19
KURTOSIS		2.92
COEFFICIENT OF VARIATION		4.0%
NUMBER OF PARTICIPANTS		1301

FREQUENCIES

FEMALES							MALES			
F	FPct	CumF	CumFPct	CM			F	FPct	CumF	CumFPct
1	0.16	1	0.16	144.25	-	145.75				
1	0.16	2	0.32	145.75	-	147.25				
0	0.00	2	0.32	147.25	-	148.75				
9	1.45	11	1.77	148.75	-	150.25				
14	2.26	25	4.03	150.25	-	151.75				
17	2.74	42	6.77	151.75	-	153.25	1	0.08	1	0.08
27	4.35	69	11.13	153.25	-	154.75	1	0.08	2	0.15
40	6.45	109	17.58	154.75	-	156.25	2	0.15	4	0.31
37	5.97	146	23.55	156.25	-	157.75	1	0.08	5	0.38
39	6.29	185	29.84	157.75	-	159.25	1	0.08	6	0.46
48	7.74	233	37.58	159.25	-	160.75	7	0.54	13	1.00
67	10.81	300	48.39	160.75	-	162.25	17	1.31	30	2.31
63	10.16	363	58.55	162.25	-	163.75	20	1.54	50	3.84
56	9.03	419	67.58	163.75	-	165.25	32	2.46	82	6.30
54	8.71	473	76.29	165.25	-	166.75	63	4.84	145	11.15
35	5.65	508	81.94	166.75	-	168.25	65	5.00	210	16.14
33	5.32	541	87.26	168.25	-	169.75	71	5.46	281	21.60
30	4.84	571	92.10	169.75	-	171.25	82	6.30	363	27.90
13	2.10	584	94.19	171.25	-	172.75	115	8.84	478	36.74
15	2.42	599	96.61	172.75	-	174.25	105	8.07	583	44.81
13	2.10	612	98.71	174.25	-	175.75	123	9.45	706	54.27
3	0.48	615	99.19	175.75	-	177.25	119	9.15	825	63.41
1	0.16	616	99.35	177.25	-	178.75	93	7.15	918	70.56
3	0.48	619	99.84	178.75	-	180.25	79	6.07	997	76.63
1	0.16	620	100.00	180.25	-	181.75	66	5.07	1063	81.71
				181.75	-	183.25	64	4.92	1127	86.63
				183.25	-	184.75	39	3.00	1166	89.62
				184.75	-	186.25	44	3.38	1210	93.01
				186.25	-	187.75	35	2.69	1245	95.70
				187.75	-	189.25	18	1.38	1263	97.08
				189.25	-	190.75	14	1.08	1277	98.16
				190.75	-	192.25	12	0.92	1289	99.08
				192.25	-	193.75	6	0.46	1295	99.54
				193.75	-	195.25	3	0.23	1298	99.77
				195.25	-	196.75	2	0.15	1300	99.92
				196.75	-	198.25	1	0.08	1301	100.00

Figure A.12 Statistics for stature anthropometric measurement in ANSURII. Figure from [1].

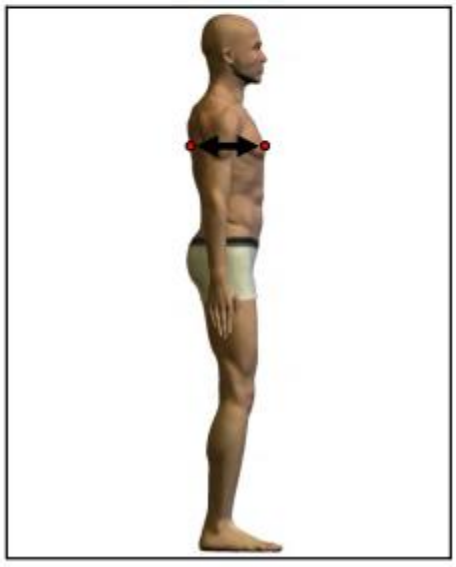

PERCENTILES				
FEMALES			MALES	
CM	IN		CM	IN
19.30	7.60	1ST	19.80	7.80
19.84	7.81	2ND	20.10	7.91
20.00	7.87	3RD	20.50	8.07
20.40	8.03	5TH	21.00	8.27
21.10	8.31	10TH	21.70	8.54
21.50	8.46	15TH	22.20	8.74
22.00	8.66	20TH	22.60	8.90
22.30	8.78	25TH	23.00	9.06
22.60	8.90	30TH	23.30	9.17
23.00	9.06	35TH	23.60	9.29
23.30	9.17	40TH	24.00	9.45
23.50	9.25	45TH	24.30	9.57
23.70	9.33	50TH	24.60	9.69
24.00	9.45	55TH	24.80	9.76
24.20	9.53	60TH	25.10	9.88
24.60	9.69	65TH	25.33	9.97
24.90	9.80	70TH	25.70	10.12
25.10	9.88	75TH	26.00	10.24
25.50	10.04	80TH	26.40	10.39
25.90	10.20	85TH	26.90	10.59
26.50	10.43	90TH	27.40	10.79
27.60	10.87	95TH	28.20	11.10
28.48	11.21	97TH	28.60	11.26
29.00	11.42	98TH	29.00	11.42
29.50	11.61	99TH	29.60	11.65

Figure A.13 Illustration and list of percentiles for chest depth anthropometric measurement from ANSURII. Figure from [1].

PERCENTILES				
FEMALES			MALES	
CM	IN		CM	IN
15.60	6.14	1ST	17.20	6.77
15.90	6.26	2ND	17.60	6.93
16.10	6.34	3RD	17.80	7.01
16.31	6.42	5TH	18.20	7.17
17.00	6.69	10TH	18.90	7.44
17.50	6.89	15TH	19.33	7.61
17.80	7.01	20TH	19.70	7.76
18.00	7.09	25TH	20.00	7.87
18.30	7.20	30TH	20.40	8.03
18.70	7.36	35TH	20.70	8.15
18.90	7.44	40TH	21.00	8.27
19.20	7.56	45TH	21.40	8.43
19.60	7.72	50TH	21.70	8.54
19.80	7.80	55TH	22.00	8.66
20.00	7.87	60TH	22.30	8.78
20.37	8.02	65TH	22.70	8.94
20.60	8.11	70TH	23.10	9.09
21.20	8.35	75TH	23.50	9.25
21.70	8.54	80TH	24.10	9.49
22.19	8.73	85TH	24.60	9.69
23.18	9.12	90TH	25.20	9.92
24.59	9.69	95TH	26.39	10.39
25.54	10.05	97TH	27.20	10.71
26.26	10.33	98TH	27.70	10.91
27.20	10.71	99TH	28.79	11.34

Figure A.14 Illustration and list of percentiles for waist depth anthropometric measurement from ANSURII. Figure from [1].

PERCENTILES				
FEMALES			MALES	
CM	IN		CM	IN
23.32	9.18	1ST	25.20	9.92
23.90	9.41	2ND	26.00	10.24
24.40	9.61	3RD	26.20	10.31
24.80	9.76	5TH	26.60	10.47
25.50	10.04	10TH	27.40	10.79
26.00	10.24	15TH	28.00	11.02
26.40	10.39	20TH	28.50	11.22
26.90	10.59	25TH	29.00	11.42
27.30	10.75	30TH	29.30	11.54
27.80	10.94	35TH	29.80	11.73
28.10	11.06	40TH	30.10	11.85
28.60	11.26	45TH	30.60	12.05
28.80	11.34	50TH	31.00	12.20
29.20	11.50	55TH	31.50	12.40
29.50	11.61	60TH	31.80	12.52
29.80	11.73	65TH	32.30	12.72
30.20	11.89	70TH	32.70	12.87
30.60	12.05	75TH	33.10	13.03
31.10	12.24	80TH	33.70	13.27
31.70	12.48	85TH	34.40	13.54
32.30	12.72	90TH	35.10	13.82
33.50	13.19	95TH	36.20	14.25
33.98	13.38	97TH	37.20	14.65
35.06	13.80	98TH	37.40	14.72
36.70	14.45	99TH	38.80	15.28

Figure A.15 Illustration and list of percentiles for waist breadth anthropometric measurement from ANSURII. Figure from [1].

APPENDIX B. ADDITIONAL FIGURES AND TABLES FOR HBM SCALING

Table B 1 Comparison of ANSURII and scaled CAVEMAN statures and weights for the 5th to 95th percentile in increments of 1 percentile.

Percentile	Target Stature (cm)	Scaled Stature (cm)	Stature Difference (cm)	Stature % Difference	Target Weight (kg)	Scaled Weight (kg)	Weight Difference (kg)	Weight % Difference
5	164.70	164.69	-0.01	0.005%	62.48	63.71	1.23	1.98%
6	165.06	165.05	-0.01	0.005%	63.12	64.25	1.13	1.79%
7	165.42	165.41	-0.01	0.004%	63.77	64.92	1.16	1.81%
8	165.78	165.77	-0.01	0.003%	64.41	65.60	1.19	1.85%
9	166.14	166.14	0.00	0.003%	65.06	66.28	1.23	1.89%
10	166.50	166.50	0.00	0.002%	65.70	66.84	1.14	1.73%
11	166.75	166.74	0.00	0.001%	66.26	67.52	1.26	1.90%
12	166.99	166.99	0.00	0.001%	66.82	68.07	1.25	1.88%
13	167.24	167.24	0.00	0.000%	67.38	68.63	1.25	1.86%
14	167.48	167.48	0.00	0.000%	67.94	69.19	1.25	1.84%
15	167.73	167.73	0.00	0.001%	68.50	69.75	1.25	1.83%
16	168.04	168.05	0.00	0.001%	68.88	70.13	1.25	1.81%
17	168.36	168.36	0.00	0.001%	69.26	70.50	1.24	1.80%
18	168.67	168.67	0.00	0.001%	69.64	70.88	1.24	1.78%
19	168.99	168.99	0.00	0.001%	70.02	71.08	1.06	1.51%
20	169.30	169.30	0.00	0.001%	70.40	71.63	1.23	1.74%
21	169.59	169.59	0.00	0.001%	70.70	71.89	1.19	1.68%
22	169.88	169.88	0.00	0.001%	71.00	72.15	1.15	1.63%
23	170.17	170.17	0.00	0.001%	71.30	72.56	1.26	1.77%
24	170.46	170.46	0.00	0.001%	71.60	72.83	1.23	1.71%
25	170.75	170.75	0.00	0.001%	71.90	73.09	1.19	1.66%
26	170.94	170.94	0.00	0.001%	72.24	73.52	1.28	1.77%
27	171.13	171.13	0.00	0.001%	72.58	73.80	1.22	1.68%
28	171.32	171.32	0.00	0.001%	72.92	74.08	1.16	1.59%
29	171.51	171.51	0.00	0.002%	73.26	74.51	1.25	1.70%
30	171.70	171.70	0.00	0.002%	73.60	74.78	1.18	1.60%
31	171.86	171.86	0.00	0.002%	73.88	75.12	1.24	1.68%
32	172.02	172.02	0.00	0.002%	74.16	75.32	1.16	1.57%
33	172.18	172.18	0.00	0.003%	74.44	75.66	1.22	1.64%
34	172.34	172.35	0.01	0.003%	74.72	76.01	1.29	1.73%
35	172.50	172.51	0.01	0.003%	75.00	76.21	1.21	1.62%
36	172.66	172.66	0.01	0.003%	75.32	76.55	1.23	1.63%

Table B 1 continued

37	172.81	172.82	0.01	0.004%	75.64	76.89	1.25	1.65%
38	172.97	172.97	0.01	0.004%	75.96	77.23	1.27	1.67%
39	173.12	173.13	0.01	0.004%	76.28	77.57	1.29	1.69%
40	173.28	173.29	0.01	0.004%	76.60	77.77	1.17	1.52%
41	173.48	173.49	0.01	0.004%	76.86	78.03	1.17	1.53%
42	173.69	173.70	0.01	0.004%	77.12	78.30	1.18	1.54%
43	173.89	173.90	0.01	0.005%	77.38	78.58	1.20	1.54%
44	174.10	174.10	0.01	0.005%	77.64	78.85	1.21	1.55%
45	174.30	174.31	0.01	0.005%	77.90	79.12	1.22	1.56%
46	174.44	174.45	0.01	0.005%	78.30	79.60	1.30	1.66%
47	174.58	174.59	0.01	0.005%	78.70	79.93	1.23	1.56%
48	174.72	174.73	0.01	0.005%	79.10	80.27	1.17	1.48%
49	174.86	174.87	0.01	0.006%	79.50	80.75	1.25	1.57%
50	175.00	175.01	0.01	0.006%	79.90	81.09	1.19	1.49%
51	175.18	175.19	0.01	0.006%	80.20	81.47	1.27	1.59%
52	175.36	175.37	0.01	0.006%	80.50	81.71	1.21	1.51%
53	175.54	175.55	0.01	0.006%	80.80	82.10	1.30	1.61%
54	175.72	175.73	0.01	0.006%	81.10	82.34	1.24	1.53%
55	175.90	175.91	0.01	0.007%	81.40	82.58	1.18	1.45%
56	176.06	176.07	0.01	0.007%	81.74	82.94	1.20	1.47%
57	176.22	176.23	0.01	0.007%	82.08	83.31	1.23	1.50%
58	176.38	176.39	0.01	0.007%	82.42	83.68	1.26	1.52%
59	176.54	176.55	0.01	0.008%	82.76	84.04	1.28	1.55%
60	176.70	176.71	0.01	0.008%	83.10	84.41	1.31	1.58%
61	176.86	176.87	0.01	0.008%	83.45	84.64	1.18	1.42%
62	177.02	177.03	0.01	0.008%	83.81	85.02	1.21	1.44%
63	177.18	177.19	0.01	0.008%	84.16	85.40	1.24	1.47%
64	177.34	177.36	0.02	0.009%	84.52	85.78	1.26	1.49%
65	177.50	177.52	0.02	0.009%	84.87	86.16	1.29	1.52%
66	177.73	177.74	0.02	0.009%	85.22	86.48	1.26	1.48%
67	177.96	177.97	0.02	0.009%	85.56	86.80	1.23	1.44%
68	178.18	178.20	0.02	0.009%	85.91	87.11	1.21	1.40%
69	178.41	178.43	0.02	0.009%	86.25	87.59	1.33	1.55%
70	178.64	178.66	0.02	0.009%	86.60	87.91	1.31	1.51%
71	178.87	178.89	0.02	0.009%	86.93	88.23	1.30	1.49%
72	179.10	179.12	0.02	0.009%	87.26	88.55	1.29	1.48%
73	179.34	179.35	0.02	0.010%	87.59	88.87	1.28	1.46%
74	179.57	179.59	0.02	0.010%	87.92	89.19	1.27	1.44%
75	179.80	179.82	0.02	0.010%	88.25	89.51	1.26	1.43%
76	180.10	180.12	0.02	0.010%	88.76	90.08	1.32	1.49%
77	180.40	180.40	0.00	0.000%	89.27	90.22	0.95	1.07%

Table B 1 continued

78	180.70	180.70	0.00	0.000%	89.78	90.66	0.88	0.98%
79	181.00	181.00	0.00	0.000%	90.29	91.10	0.81	0.90%
80	181.30	181.32	0.02	0.011%	90.80	92.07	1.27	1.40%
81	181.59	181.61	0.02	0.011%	91.27	92.50	1.24	1.36%
82	181.89	181.91	0.02	0.011%	91.73	92.93	1.20	1.31%
83	182.18	182.20	0.02	0.011%	92.20	93.37	1.17	1.27%
84	182.48	182.50	0.02	0.011%	92.66	93.80	1.14	1.23%
85	182.77	182.79	0.02	0.011%	93.13	94.24	1.11	1.19%
86	183.21	183.23	0.02	0.011%	93.81	95.04	1.24	1.32%
87	183.65	183.68	0.02	0.012%	94.49	95.69	1.21	1.28%
88	184.10	184.12	0.02	0.012%	95.16	96.34	1.18	1.24%
89	184.54	184.56	0.02	0.012%	95.84	97.00	1.16	1.21%
90	184.98	185.00	0.02	0.012%	96.52	97.66	1.14	1.18%
91	185.44	185.47	0.02	0.013%	97.56	98.69	1.13	1.15%
92	185.91	185.93	0.02	0.013%	98.60	99.72	1.12	1.14%
93	186.37	186.40	0.03	0.014%	99.64	100.76	1.12	1.13%
94	186.84	186.86	0.03	0.014%	100.68	101.82	1.14	1.13%
95	187.30	187.33	0.03	0.015%	101.72	102.87	1.15	1.13%

Table B 2 Comparison of the ANSURII weight and the seated scaled CAVEMAN weight for the 5^{th} to 95^{th} percentiles in increments of 1 percentile.

Percentile	**Target Weight (kg)**	**Scaled Weight(kg)**	**Weight Difference (kg)**	**Weight % Difference**
5	62.48	61.46	-1.02	1.63%
6	63.124	61.98	-1.14	1.81%
7	63.768	62.62	-1.15	1.80%
8	64.412	63.27	-1.14	1.77%
9	65.056	63.92	-1.13	1.74%
10	65.7	64.45	-1.25	1.90%
11	66.26	65.10	-1.16	1.74%
12	66.82	65.63	-1.19	1.77%
13	67.38	66.17	-1.21	1.80%
14	67.94	66.70	-1.24	1.83%
15	68.5	67.24	-1.26	1.84%
16	68.88	67.60	-1.28	1.86%
17	69.26	67.96	-1.30	1.87%
18	69.64	68.33	-1.31	1.89%

Table B 2 continued

19	70.02	68.52	-1.50	2.14%
20	70.4	69.04	-1.36	1.93%
21	70.7	69.30	-1.40	1.98%
22	71	69.56	-1.44	2.03%
23	71.3	69.95	-1.35	1.90%
24	71.6	70.21	-1.39	1.95%
25	71.9	70.46	-1.44	2.00%
26	72.24	70.87	-1.37	1.90%
27	72.58	71.14	-1.44	1.99%
28	72.92	71.41	-1.51	2.07%
29	73.26	71.82	-1.44	1.97%
30	73.6	72.08	-1.52	2.07%
31	73.88	72.40	-1.48	2.00%
32	74.16	72.60	-1.56	2.11%
33	74.44	72.93	-1.51	2.03%
34	74.72	73.26	-1.46	1.96%
35	75	73.45	-1.55	2.06%
36	75.32	73.78	-1.54	2.05%
37	75.64	74.10	-1.54	2.04%
38	75.96	74.42	-1.54	2.02%
39	76.28	74.75	-1.53	2.01%
40	76.6	74.94	-1.66	2.17%
41	76.86	75.20	-1.66	2.16%
42	77.12	75.46	-1.66	2.16%
43	77.38	75.72	-1.66	2.15%
44	77.64	75.98	-1.66	2.14%
45	77.9	76.24	-1.66	2.13%
46	78.3	76.70	-1.60	2.05%
47	78.7	77.01	-1.69	2.14%
48	79.1	77.34	-1.76	2.23%
49	79.5	77.80	-1.70	2.14%
50	79.9	78.12	-1.78	2.23%
51	80.2	78.49	-1.71	2.14%
52	80.5	78.72	-1.78	2.22%
53	80.8	79.09	-1.71	2.12%
54	81.1	79.32	-1.78	2.20%
55	81.4	79.55	-1.85	2.28%
56	81.74	79.90	-1.84	2.25%
57	82.08	80.25	-1.83	2.23%
58	82.42	80.60	-1.82	2.21%

Table B 2 continued

59	82.76	80.95	-1.81	2.19%
60	83.1	81.30	-1.80	2.16%
61	83.454	81.52	-1.93	2.32%
62	83.808	81.88	-1.93	2.30%
63	84.162	82.25	-1.92	2.28%
64	84.516	82.61	-1.90	2.25%
65	84.87	82.98	-1.89	2.23%
66	85.216	83.28	-1.93	2.27%
67	85.562	83.59	-1.97	2.31%
68	85.908	83.89	-2.01	2.35%
69	86.254	84.35	-1.91	2.21%
70	86.6	84.66	-1.94	2.24%
71	86.93	84.96	-1.97	2.26%
72	87.26	85.27	-1.99	2.28%
73	87.59	85.58	-2.01	2.30%
74	87.92	85.89	-2.03	2.31%
75	88.25	86.20	-2.05	2.33%
76	88.76	86.75	-2.01	2.27%
77	89.27	86.89	-2.38	2.67%
78	89.78	87.31	-2.47	2.75%
79	90.29	87.73	-2.56	2.83%
80	90.8	88.66	-2.14	2.36%
81	91.266	89.07	-2.19	2.40%
82	91.732	89.48	-2.25	2.45%
83	92.198	89.90	-2.30	2.49%
84	92.664	90.32	-2.35	2.53%
85	93.13	90.74	-2.39	2.57%
86	93.808	91.51	-2.30	2.45%
87	94.486	92.13	-2.35	2.49%
88	95.164	92.76	-2.40	2.53%
89	95.842	93.39	-2.45	2.56%
90	96.52	94.02	-2.50	2.59%
91	97.56	95.00	-2.56	2.62%
92	98.6	95.99	-2.61	2.64%
93	99.64	96.99	-2.65	2.66%
94	100.68	98.00	-2.68	2.67%
95	101.72	99.01	-2.71	2.67%

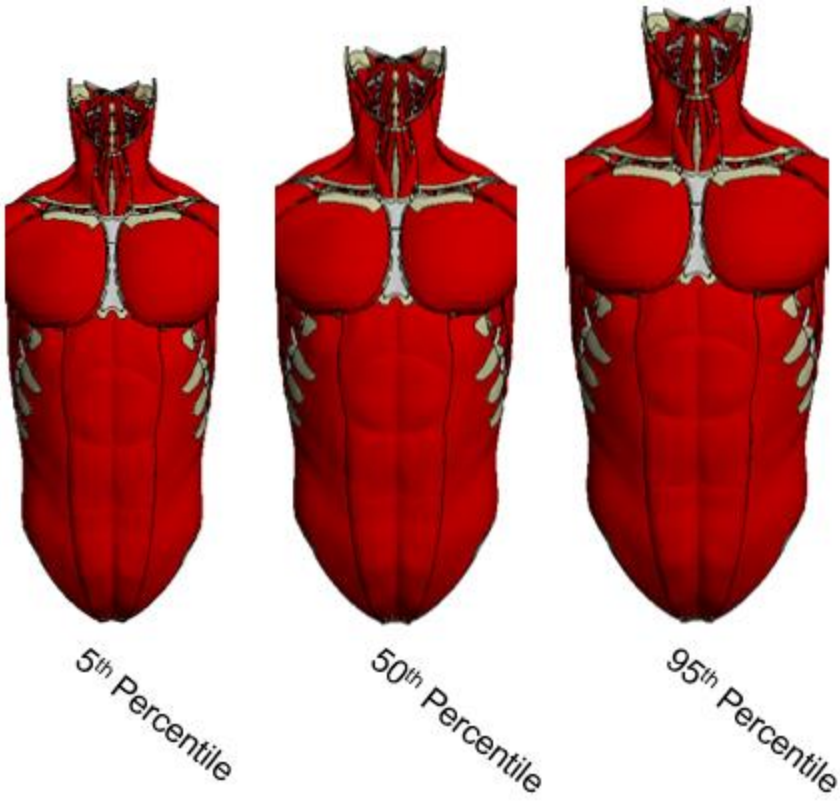

Figure B.1 Comparison of 50th percentile torso compared to scaled 5th and 95th percentile torsos. Figure from [80].

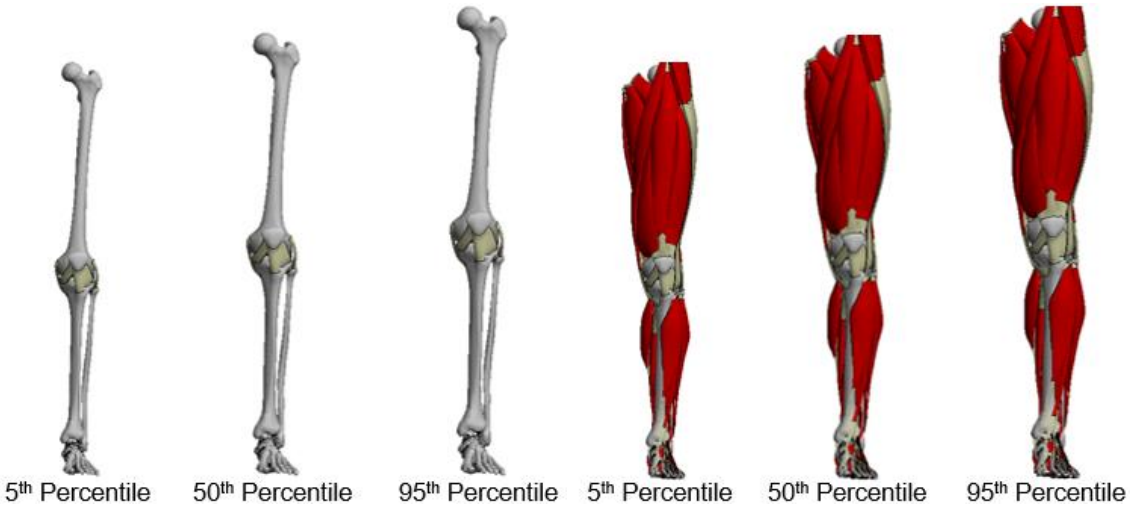

Figure B.2 Comparison of 50th percentile leg compared to scaled 5th and 95th percentile legs, with and without soft tissue visible. Figure from [80].

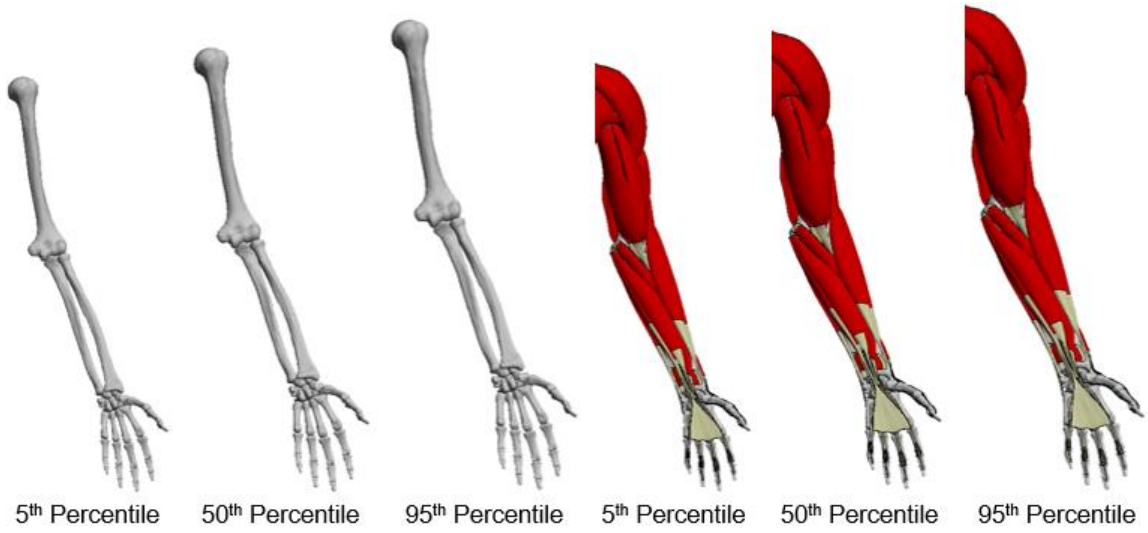

Figure B.3 Comparison of 50th percentile arm compared to scaled 5th and 95th percentile arms, with and without soft tissue visible. Figure from [80].

APPENDIX C. ADDITIONAL FIGURES AND TABLES FROM HELMET TESTING DIGITAL TWIN

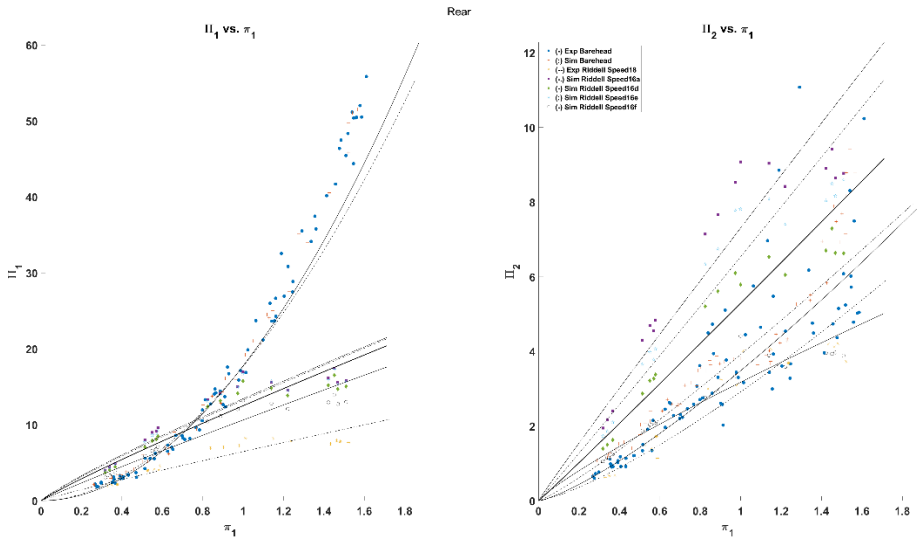

Figure C.1 Pi plots inclusive of data from the experimental and simulated barehead and simulated helmeted impacts for the rear impact location.

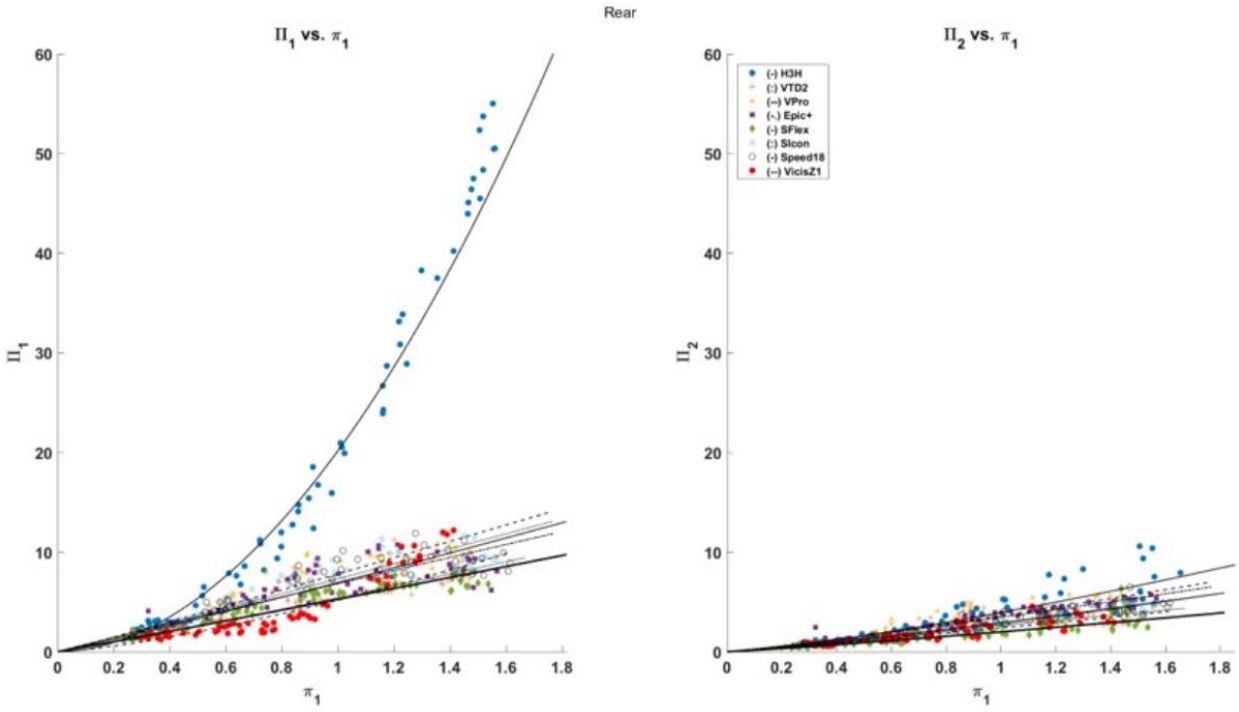

Figure C. 2 Rear pi plots for experimental helmet testing. Figure from [90].